Aus dem Fachbereich Medizinische Physiologie Theoretische Medizin und Biowissenschaften der Medizinischen Fakultät der Universität des Saarlandes, Homburg/Saar

Effect of cell maturation and cytokine inhibition on the cytotoxic arsenal release by $CD8^+$ T cells

DISSERTATION

zur Erlangung des Grades eines Doktors der Naturwissenschaften der Medizinischen Fakultät der UNIVERSITÄT DES SAARLANDES

2025

vorgelegt von **Omnia Mohmed Khamis Ibrahim**

geboren am 1.09.1990 in Alexandria, Egypt

Tag der Promotion: 07.11.2025

Dekan: Prof. Dr. M. Hannig

Berichterstatter: PD U. Becherer

Prof. M. Hoth

Disclosure

From 9-12-2019 till 31-12-2024.

All experiments were supported and performed at the Department of Cellular Neurophysiology (formerly Prof. Dr. Jens Rettig) from Institute of Physiology, Center for Integrative Physiology and Molecular Medicine (CIPMM), Saarland University, 66424 Homburg, Germany.

Eidesstattliche Versicherung
(Erklärung gemäß § 7 Absatz 1 Nr. 2)

Ich erkläre hiermit an Eides statt, dass ich die vorliegende Arbeit ohne unzulässige Hilfe Dritter und ohne Benutzung anderer als der angegebenen Hilfsmittel angefertigt habe. Die aus anderen Quellen direkt oder indirekt übernommenen Daten und Konzepte sind unter Angabe der Quelle gekennzeichnet.

Bei der Auswahl und Auswertung folgenden Materials haben mir die nachstehend aufgeführten Personen in der jeweils beschriebenen Weise unentgeltlich geholfen:

1. Der elektronenmikroskopische Aufnahmen wurde von Dr. Claudia Schirra durchgeführt.
2. Die RT-qPCR wurde von Szumin Tu durchgeführt.

Weitere Personen waren an der inhaltlich-materiellen Erstellung der vorliegenden Arbeit nicht beteiligt. Insbesondere habe ich nicht die entgeltliche Hilfe von Vermittlungs- bzw. Beratungsdiensten (Promotionsberaterinnen/Promotionsberater oder anderer Personen) in Anspruch genommen. Außer den Angegebenen hat niemand von mir unmittelbar oder mittelbar geldwerte Leistungen für Arbeiten erhalten, die im Zusammenhang mit dem Inhalt der vorgelegten Dissertation stehen.

Die Arbeit wurde bisher weder im Inland noch im Ausland in gleicher oder in ähnlicher Form in einem anderen Verfahren zur Erlangung des Doktorgrades einer anderen Prüfungsbehörde vorgelegt.
Ich versichere an Eides statt, dass ich nach bestem Wissen die Wahrheit gesagt und nichts verschwiegen habe. Die Bedeutung der eidesstattlichen Erklärung und die strafrechtlichen Folgen einer unrichtigen oder unvollständigen eidesstattlichen Erklärung sind mir bekannt.

_____

(Ort, Datum)

_____

(Unterschrift der/des Promovierenden)

_____

(Unterschrift der die Versicherung an Eides statt aufnehmenden Beamtin bzw. des aufnehmenden Beamten)

Acknowledgment

I would like to express my deepest gratitude to **Prof. Dr. Jens Rettig** for providing an exceptional platform to pursue my Ph.D.

Special thanks to my supervisor, **PD Dr. Ute Becherer**, for her unwavering support during my most challenging times. She gave me the encouragement and confidence to overcome my internal struggles. Beyond academic guidance, she provided a supportive and welcoming environment, making my Ph.D. journey both enriching and fulfilling. She always made me feel included and valued, encouraged me to pursue my ideas with confidence, and helped me master methodologies such as TIRF and SIM microscopy. Her guidance has been a cornerstone of my progress in my Ph.D. and personal life.

I thank **Dr. Varsha Pattu** for her initial guidance during the early stages of my Ph.D., which helped me build a strong foundation. My sincere thanks go to **PD Dr. Elmar Krause** for his insightful discussions and methodological support with Flow cytometry and SIM microscopy.

I would also like to thank **Dr. Claudia Schirra** for her expertise in TEM imaging and invaluable support, which provided me with both personal encouragement and professional guidance, and **Dr. Hsin-Fang Chang** for her productive discussion.

My gratitude extends to **Anja Ludes**, **Margarete Klose**, **Nicole Rothgerber**, and **Katrin Sandmeier** for their technical assistance, and to **Bernadette Schwarz** and **Andrea Berger** for their administrative help and personal support.

I would like to thank **Dr. Keerthana Ravichandran** for her priceless guidance. My heartfelt gratitude also goes to **Szumin Tu**, who not only provided me with immense help in my experiments but also gave me emotional support during my most difficult moments, like the true sister I never had, created an environment that made me feel at ease and to **Abed Alrahman Chouaib** for his help with some of the data processing.

Last but not least, I am deeply thankful to my beloved mother for her unwavering belief in me, my Egyptian friends **Mohanad Elkhaligy**, and **Amira El Sayed** for their consistent emotional support during my whole journey, which made it much easier for me to move forward, **Omnia Ali,** for the strength she gave me to continue and not give up on myself, **Desi**, my loyal sleepy German cat, for her comforting companionship and also **Princy,** my Egyptian cat, whose playful spirit kept me smiling through stressful days, has passed away, but his presence will always be cherished.

Content

List of Abbreviations

	%	Percentage
	°C	Degrees Celsius
	µL	Microliter
	µM	Micromolar
	n or N	Number
	ANOVA	Analysis of variance
A	APCs	Antigen-presenting cells
	BME	β-Mercaptoethanol
B	BSA	Bovine serum albumin
	Ca^{2+}	Calcium
C	$CaCl_2$	Calcium chloride
	CCR7	CC chemokine receptor 7
	CD	cluster of differentiation
	cDNA	complementary DNA
	CGs	Cytotoxic granules
	CO_2	Carbon dioxide
	CRAC	Ca^{2+} release-activated channels
	CsA	Cyclosporin A
	cSMAC	Central supra-molecular activation cluster
	CT	threshold cycle
	CTLs	Cytotoxic T lymphocytes
	CV	coefficient of variation
	DCs	Dendritic cells
D	DGS-NTA	1,2-dioleoyl-sn-glycero-3-[(N-(5-amino-1-carboxypentyl)iminodiacetic acid) succinyl]
	DMSO	Dimethyl sulfoxide
	DNA	Deoxyribonucleic Acid
	DOPC	1,2-dioleoyl-sn-glycero-3-phosphocholine
	DPBS	Dulbecco's phosphate-buffered saline
	dSMAC	Distal supra-molecular activation cluster
	ECM	extracellular matrix
E	EDTA	Ethylenediaminetetraacetic acid
	EE	early endosomes

	ER	Endoplasmic reticulum
	ER	endoplasmic reticulum
	et al.	et alia
	F-actin	Filamentous actin
F	Fas	First apoptosis signal receptor
	FasL	Fas ligand
	FCS	Fetal calf serum
	GzmB	Granzyme B
G	H	Hour
	HBS	HEPES-Buffered Saline
H	HEPES	4-(2-Hydroxyethyl)-1-piperazineethanesulfonic acid
	HSA	Human Serum Albumin Buffer
	IB	Isolation buffer
I	ICAM	intercellular adhesion molecule
	IFNGR	Interferon-gamma receptor
	IFN-γ	Interferon-gamma
	IL	Interleukin
	IL10R	IL-10 receptor
	IP3	Inositoll 1,4,5-trisphosphate
	IS	Immunological synapse
	KCl	Potassium chloride
K	kDa	Kilodalton
	KI	Knockin
	L	Liter
L	LAMP-1	lysosomal-associated membrane protein 1
	LE	late endosome
	LFA-1	Lymphocyte function-associated antigen
	m	Mili
M	MCGs.	Multi-core granules
	MgCl2	Magnesium chloride
	MHC	major histocompatibility complex
	min	Minute
	mL	Milliliter
	mm	Millimeter
	mM	Millimolar

	mmol	Millimole
	MOC	Manders' overlap coefficient
	mRNA	Messenger Ribonucleic Acid
	Munc13	Mammalian uncoordinated-13
	MW	Molecular weight
	Na_2HPO_4	Disodium phosphate
N	NaCl	Sodium chloride
	NaH_2PO_4	Monosodium phosphate
	$NaHCO_3$	Sodium bicarbonate
	NFATs	Nuclear Factor of Activated T cells
	NFκB	Nuclear factor kappa-light-chain-enhancer of activated B cells
	NH_4Cl	Ammonium chloride
	NK	Natural killer cells
	nm	Nanometer
	NTA	nitrilotriacetic acid
	p	Probability value
P	PBS	Phosphate-buffered saline
	PCC	Pearson's correlation coefficient
	PCR	Polymerase chain reaction
	PE	Phycoerythrin
	PFA	paraformaldehyde
	pg	picogram
	pH	Potential hydrogen
	PLO	Poly-L-ornithine
	Prf1	Perforin-1
	pSMAC	Peripheral supra-molecular activation cluster
	Rab5	Ras-related in brain 5
R	RNA	Ribonucleic Acid
	ROI	region of interest
	rpm	Revolutions per minute
	RT	Room temperature
	RT-PCR	Reverse transcription of RNA
	RT-qPCR	Real-time quantitative PCR
	s	Second
	SA-PE	Streptavidin-phycoerythrin

S	SCGs	Single-core granules
	SEM	Standard error of the mean
	SIM	Structure illumination microscopy
	SIM	Structured Illumination Microscopy
	SLB	Supported lipid bilayer
	SMAC	Supramolecular activation clusters
	SMAPs	Supramolecular attack particles
	SNAP-23	the synaptosome-associated protein -23
	SNARE	Soluble N-ethylmaleimide-sensitive factor Attachment protein Receptor
	StdDev	Standard deviation
	STIM1	Stromal interaction molecule 1
	TBP	TATA-binding protein
	Tcm	Central memory T cell
T	TCRs	T cell receptors
	Tem	Effector memory T cells
	TIRFM	Total Internal Reflection Fluorescence Microscopy
	TNF	tumor necrosis factor-alpha
	TNF	Tumor necrosis factor
	t-SNARE	Target-SNARE
	TSP-1	Thrombospondin-1
	U	Units
U	UV	Ultraviolet
V	v-SNARE	Vesicular-SNARE
	WGA	Wheat germ agglutinin
W	WT	Wild-type

List of Tables

List of Figures

Abstract

Cytotoxic T lymphocytes (CTLs) play a pivotal role in the eradication of infected and malignant cells through the release of cytotoxic molecules, including perforin (Prf) and granzyme B (GzmB). These molecules are stored in specialized granules. Two classes of granules were identified by Bálint et al. (2020) and Chang et al. (2022), single-core granules (SCGs) and multi-core granules (MCGs). It is noteworthy that MCGs discharge their toxic cargo in the form of supramolecular attack particles (SMAPs) into the immunological synapse (IS), thereby ensuring precise and efficient destruction of the target cell.

In order to explore the factors that induce T cell cytotoxicity, we employed both wild-type and GzmB-tdTomato knock-in mice, in addition to fluorescently labeled thrombospondin-1 (TSP-1) as markers for MCGs. By employing flow cytometry and advanced imaging techniques, namely Total Internal Reflection Fluorescence Microscopy (TIRFM), Structured Illumination Microscopy (SIM), and Transmission Electron Microscopy (TEM), we were able to ascertain that prolonged culture time led to increased biogenesis and release of CGs without any alteration to the T cell subtypes.

The exogenous labeling with Wheat germ agglutinin (WGA) revealed the existence of a potential intermediate CG, which may serve as a step in MCGs maturation. This novel class is capable of releasing cytotoxic substances in the IS, in a similar manner to that observed with SCGs. Furthermore, we discovered that stimulation of T cells at an earlier stage of culture boosts the maturation of T cells through the generation of more MCGs and SMAPs.

Given the essential role of cytokines in T-cell activation, we conducted further research to ascertain whether these cytokines could influence the generation of MCGs and additionally SMAPs. To this end, we employed Cyclosporin A (CsA), a well-characterized immunosuppressant, to elucidate the contribution of diverse cytokines to MCG release. In particular, we demonstrated that Interferon-gamma (IFN-γ), a crucial cytotoxic cytokine, markedly affected MCG release. This conclusion was corroborated through the utilization of anti-IFN-γ antibody.

My work revealed two unidentified factors (time in culture and the concentration of IFN-γ) that modify the generation and the subsequent release of MCGs and SMAPs formation. These findings have the potential to facilitate the development of novel immunotherapeutic strategies, providing new avenues for the enhancement of T cell-mediated cancer and infection therapies.

Zusammenfassung

Zytotoxische T-Lymphozyten (CTL) spielen durch die Freisetzung zytotoxischer Moleküle, darunter Perforin (Prf) und Granzyme B (GzmB), eine zentrale Rolle bei der Vernichtung infizierter und bösartiger Zellen. Diese Moleküle werden in spezialisierten Granula gespeichert. Bálint et al. (2020) und Chang et al. (2022) haben zwei Klassen von Granula identifiziert: einkernige Granula (SCGs) und mehrkernige Granula (MCGs). Bemerkenswert ist, dass MCGs ihre toxische Fracht in Form von supramolekularen Angriffspartikeln (SMAPs) in die immunologische Synapse (IS) entladen und damit eine präzise und effiziente Zerstörung der Zielzelle gewährleisten.

Um die Faktoren zu erforschen, die die Zytotoxizität der T-Zellen auslösen, setzten wir sowohl Wildtyp- als auch GzmB-tdTomato-Knock-in-Mäuse ein, zusätzlich zu fluoreszierend markiertem Thrombospondin-1 (TSP-1) als Marker für MCGs. Durch den Einsatz von Durchflusszytometrie und fortschrittlichen bildgebenden Verfahren, nämlich Total Internal Reflection Fluorescence Microscopy (TIRFM), Structured Illumination Microscopy (SIM) und Transmission Electron Microscopy (TEM), konnten wir feststellen, dass längere Kulturzeiten zu einer erhöhten Biogenese und Freisetzung von CGs führte, ohne dass die T-Zell-Subtypen verändert wurden.

Die exogene Markierung mit Weizenkeim-Agglutinin (WGA) zeigte die Existenz eines potenziellen Zwischenprodukts CG, das möglicherweise als Vorreifungsschritt von MCGs dient. Diese neue Klasse ist in der Lage, im IS zytotoxische Substanzen freizusetzen, ähnlich wie dies bei SCGs beobachtet wurde. Darüber hinaus entdeckten wir, dass die Stimulation von T-Zellen in einem früheren Stadium der Kultur die Reifung der T-Zellen fördert, so dass sie durch die Bildung von mehr MCGs und SMAPs.

Angesichts der wesentlichen Rolle von Zytokinen bei der T-Zell-Aktivierung führten wir weitere Untersuchungen durch, um festzustellen, ob diese die Bildung von MCGs und zusätzlich SMAPs beeinflussen könnten. Zu diesem Zweck setzten wir Cyclosporin A (CsA), ein gut charakterisiertes Immunsuppressivum, ein, um den Beitrag verschiedener Zytokine zur MCG-Freisetzung zu untersuchen. Insbesondere wurde nachgewiesen, dass Interferon-gamma (IFN-γ), ein wichtiges zytotoxisches Zytokin, die MCG-Freisetzung deutlich beeinflusst. Diese Schlussfolgerung wurde durch die Verwendung von anti-IFN-γ-antikörpern bestätigt.

Meine Arbeit ergab, dass zwei bisher unbekannte Faktoren (die Zeit in der Kultur und die IFN-γ-Konzentration) die Bildung und anschließende Freisetzung von MCGs und die SMAP-Bildung beeinflussen. Diese Erkenntnisse haben das Potenzial, die Entwicklung neuartiger immuntherapeutischer Strategien zu erleichtern und neue Wege für die Verbesserung von T-Zell-vermittelten Krebs- und Infektionstherapi.

1. Introduction

1.1 Immune system

The body has a remarkable capacity to defend itself against foreign antigens (Ag) and toxins from the surrounding environment. It is carried out by the immune system, which comprises an array of white blood cells and the lymphatic organs. The immune system is divided into two lines of defense: the innate and adaptive immune systems. The innate or nonspecific immune system represents the body's initial line of defense. It comprises natural barriers, including physical (skin and mucous membranes), chemical barriers (enzymes and acids), and cellular components of the immune system cells. The adaptive immune system is the specialized defense mechanism that delivers directed and long-lasting antigen-specific responses. It consists of lymphoid cells that include T lymphocytes, B lymphocytes, natural killer cells (NK), and innate lymphoid cells. With the help of lymphoid organs, both the innate and the adaptive immune systems work together to help immune cells to develop and respond to the infection. Lymphoid organs are divided into primary lymphoid organs that include bone marrow and thymus serving as the main sites for lymphocyte production, development, and selection of naive lymphocytes. While lymph nodes, the spleen, and the tonsils represent the secondary lymphoid organs (peripheral lymphoid organs) that help immune cells to mature and activate.

1.2 Bone marrow

Bone marrow is a primary lymphoid organ composed of spongy tissue in the hollow spaces of long-length bones such as the pelvis and femur. It gives rise to several types of immune cells, including B cells, T cell precursors, NK cells, granulocytes, monocytes, and dendritic cells.

1.2.1 B cells

B cells are produced and matured in the bone marrow and are activated by T helper cells in the secondary lymphoid organs. After activation, B cells multiply and transform into plasmocytes that produce antibodies to be released into the blood. After activation, some of the B cells are transformed into memory cells and become part of the memory of the adaptive immune system.

1.2.2 T cells

After the production of T cells in the bone marrow, they migrate via the bloodstream to the thymus. There, they experience a process of rearrangement of the T cell antigen-binding receptor genes on their membrane. This process results in the expression of a protein complex located on the surface of T lymphocytes, named T cell receptors (TCRs). According to Quang, Zaniboni, and Ghysdael (2017), the affinity level of the thymocyte's TCR in the thymus for self-peptide Major Histocompatibility Complex (MHC) determines whether they undergo apoptosis or maturation. They undergo apoptosis (negative selection) when thymocytes have a high affinity to self-peptide MHC complexes. Alternately, with low affinity, they go through a positive selection to become naïve single-positive T cells either $CD4^+$ or

$CD8^+$ T lymphocytes. These naïve T cells become effector T cells (helper or cytotoxic) depending on the antigen presentation of the cytokine signals from the antigen-presenting cells (APCs) in a process called T cell activation.

1.3 Spleen

In mice, the spleen contains about 100 million splenocytes, which are mononuclear white blood cells. These cells consist of about 25% T cells, with $CD4^+$ (cluster of differentiation 4) helper T cells and $CD8^+$ killer T cells accounting for about 16% and 8%, respectively, along with other cells like NK cells, B cells, monocytes, granulocytes, dendritic cells (DCs), and macrophages. DCs are APCs that have a crucial role in initiating an adaptive immune response when the innate immune system cannot destroy the foreign antigen.

1.3.1 T cell activation

The T cell activation process is regulated by the interaction of three TCR signaling cascades. Initially, TCRs recognize foreign antigen peptides presented by APCs through peptide-MHC class I (pMHC-I) molecules within a contact zone called the immunological synapse (IS). The TCR complex is principally constituted of integral membrane proteins, including antigen binding subunit (TCRαβ), located at the core of the complex, that is responsible for the binding to MHC-presented antigens with high specificity and three CD3 signaling subunits: CD3εδ, CD3εγ, and CD3ζζ (Smith-Garvin, Koretzky, and Jordan 2009). Subsequently, co-stimulatory signals, such as CD80 (B7.1) and CD86 (B7.2), are expressed by APCs, which interact with the CD28 receptor on T cells. Finally, the third signal is initiated when cytokines, such as interleukin 12 (IL-12) or type I interferons (type I IFNs), are secreted in response to an inflammatory stimulus. These cytokines direct and amplify T-cell differentiation and expansion. TCRs also cooperate with co-receptor glycoproteins such as CD4 or CD8, to enhance antigen recognition and subsequent T cell activation. CD4 co-receptor assists MHC class II recognition while CD8 co-receptor aids MHC class I recognition.

1.3.2 $CD8^+$ T cell differentiation

Activation of naive $CD8^+$ T cells leads to clonal expansion and differentiation into a heterogeneous pool of effector $CD8^+$ T cells. First, they differentiate into either short-lived effector cells, which die during the contraction phase, or memory progenitor effector cells, which survive and become memory $CD8^+$ T cells (Figure 1). Due to the surface proteins involved in chemotaxis and cell adhesion, memory $CD8^+$ T cells explore peripheral tissues where the infection started (Obar and Lefrançois 2010; Sun et al. 2023). In the contraction phase, a substantial proportion (90%) of effector T cells undergo programmed cell death. The remaining T cells enter the memory phase, during this phase, the number of memory T cells stabilizes over time, securing the persistence of memory T cell populations for long-term immunity.

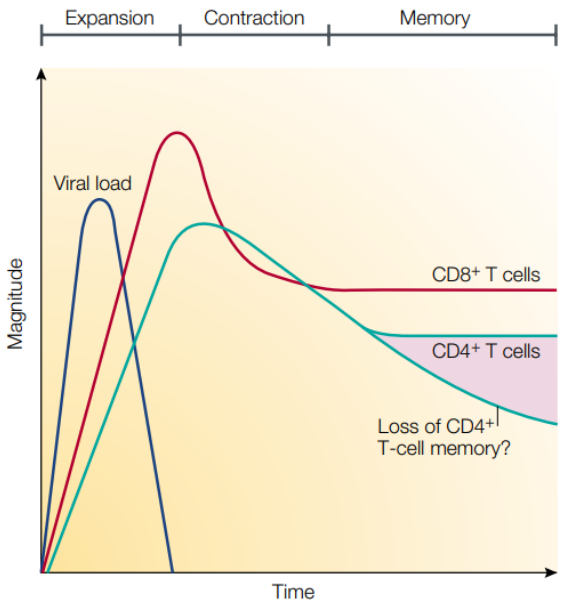

Figure 1: Antiviral response from $CD4^+$ and $CD8^+$ T-cells.

T-cell responses go through 3 main phases. It starts with encountering antigen, and afterward T cell clonally expands. After the virus clearance, during the contraction stage, most of the virus-specific T cells go through apoptosis. The remaining T cells are maintained over a longer period (the memory phase). Note that the response of the $CD4^+$ T-cell is less than the $CD8^+$ T-cell (Homann, Teyton, and Oldstone 2001; Kaech, Wherry, and Ahmed 2002)

The major subtypes of memory T cells are classified based on extracellular marker proteins, such as CC chemokine receptor 7 (CCR7) and L-selectin (CD62L) (Figure 2).

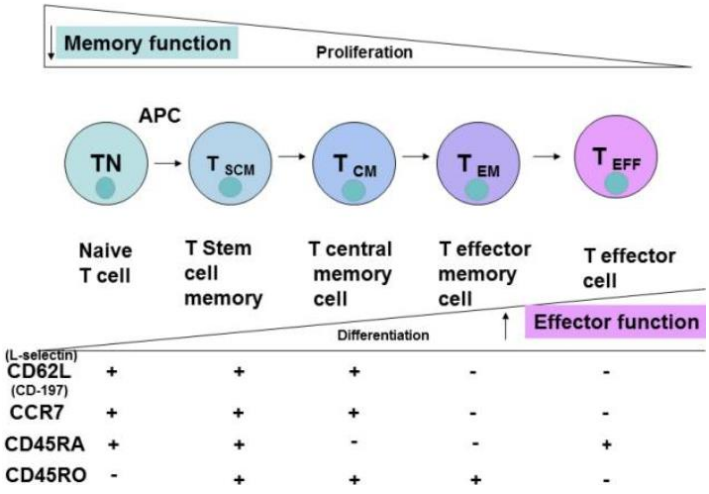

Figure 2: Describing the different $CD8^+$T cell subsets.

Naïve $CD8^+$ T cells exhibit distinct phenotypic characteristics, as evidenced by variations in surface marker protein expression (Golubovskaya and Wu 2016).

$CD8^+$ T cells expressing $CD62L^{hi}/CCR7^{hi}$, which is associated with T cell homing properties to secondary lymphoid organs, are characterized as central memory T cells (Tcm). Tcms are more capable of proliferating in response to antigens and continue producing (Interleukin-2) IL-2 after infection. On the other hand, T cells expressing $CD62L^{lo}/CCR7^{lo}$ are referred to as effector memory T cells (Tem). These Tems predominantly reside in infected non-lymphoid organs, such as peripheral tissues, due to

their expression of specific chemokines (Masopust et al. 2001; Weninger et al. 2001). This diverse subpopulation of $CD8^+$ T cells can be detected by flow cytometry (Torang, Gupta, and Klinke 2019).

1.4 Immune synapse (IS)

The formation of IS represents a fundamental stage in the activation of naïve $CD8^+$ T cells, which occurs within minutes of contact with APCs. This initial, long-lasting signaling synapse eventually results in T-cell differentiation. After the initial activation of T cells, short-lasting synapses-persisting for up to 30 minutes- can form when T cells interact with a target cell or an artificial lipid bilayer containing pMHC and intercellular adhesion molecule 1 (ICAM-1) (Alarcón, Mestre, and Martínez-Martín 2011; Davis and van der Merwe 2001).

Both long and short-lasting IS display a similar formation of a bull's-eye structure. This configuration is characterized by three clusters, referred to as supramolecular activation clusters (SMACs), each cluster has a unique molecular composition and function (Grakoui et al. 1999; Monks et al. 1998). The three cluster regions are the central SMAC (cSMAC), which is encircled by the peripheral (pSMAC), and the outer distal SMAC (dSMAC). TCRs and TCR-associated proteins such as the co-stimulatory receptor CD28, CD4 (in $CD4^+$T helper cells), and CD2 are enriched in the cSMAC, while pSMAC has a high concentration of integrins, such as lymphocyte function-associated antigen (LFA-1), as well as cytoskeleton-associated proteins and talin (Monks et al. 1998). On the other hand, filamentous actin, which forms from the polymerization of globular actin monomers, the major cytoskeletal protein, is enriched in the dSMAC. It plays a role in clustering integrins such as LFA-1 in the pSMAC. These integrins interact with ICAM-1 on the APC or the target cell to enhance the stability of the IS and amplify TCR signaling. (Comrie, Babich, and Burkhardt 2015; Le Floc'h and Huse 2015). At the dSMAC, the gathering of TCR-CD28 microcluster at the synaptic membrane is started when the TCR signaling is initiated, then they move centripetally to the IS to localize within cSMAC (Figure 3) (Grakoui et al. 1999).

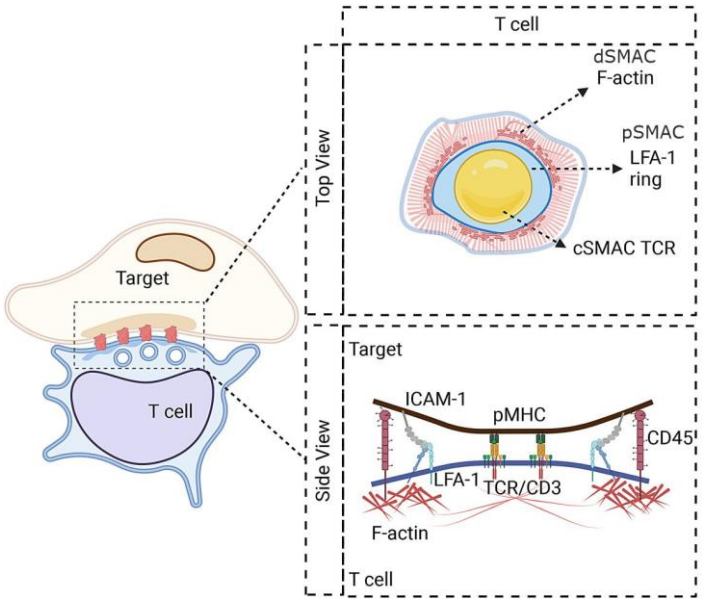

Figure 3: The bull's-eye structure of T-cell synapse.

It shows the supramolecular activation clusters (cSMAC, pSMAC, dSMAC) during IS formation between the T-cell and target. This image was edited from (Xiong, Libby, and Su 2024).

The outermost dSMAC also holds large molecules such as the glycosylated phosphatase CD45, which are involved in the dephosphorylation of the CD3ζ chain. The actin lamellipodium in the distal region controls the rearrangement within the synapse (Xiong, Libby, and Su 2024). After the initial binding of TCRs to their target, a sequence of relocalization events takes place in the Cytotoxic T Lymphocyte (CTL). These events are initiated from the centrosome, which is the major microtubule-organizing center (MTOC). The centrosome is a structure comprising two centrioles encased in pericentriolar material. Its relocation towards the IS occurs in response to a diacylglycerol gradient that shifts from the posterior of the cell to the membrane region in contact with the target cell (Quann et al. 2009). The relocalization of the centrosome in CTLs results in the formation of a microtubule network that extends from the centrosome to the IS (Stinchcombe et al. 2011). The delivery of secretory vesicles along the microtubule network toward the MTOC is mediated by dynein. Subsequently, upon arrival at the MTOC, kinesin transports these vesicles toward the cSMAC at the IS (Kurowska et al. 2012). Typically, these vesicles move as tethered pairs of recycling endosomes and lytic granules (Qu et al. 2011).

The formation of the IS by the T cell is pivotal not only for the activation of CTLs but also for achieving their primary function as mature CTLs, which is to eliminate target cells. T cells utilize two principal mechanisms to trigger apoptosis in target cells: the calcium-dependent Prf1/Gzm pathway and the calcium-independent Fas/Fas ligand (FasL) pathway (Atkinson et al., 1998). Both pathways involve the close contact between T cells and their target cells (Lowin et al. 1994), which ensures the precise and efficient elimination of harmful or infected cells.

1.5 Calcium (Ca^{2+}) role in secretory vesicle release

1.5.1 Mechanisms of store-operated Ca^{2+} intake in T cell activation

Ca^{2+} signal plays a role in transducing information that is related to T cell subtypes, developmental state, antigen properties, and APC type (Lewis 2001). The killing mechanism of CTLs after TCR activation was shown to rely on the release of intracellular Ca^{2+} $[Ca^{2+}]_i$ from the endoplasmic reticulum (ER), as well as the Ca^{2+} influx from the extracellular space. Firstly, the TCR stimulation results in the activation of phospholipase C gamma 1, which subsequently produces diacylglycerol and inositol 1,4,5-trisphosphate (IP3). IP3 then binds to its receptor located on the ER, to induce the efflux of the stored Ca^{2+} to the cytoplasm (Joseph, Reicher, and Barda-Saad 2014). In the event of an ER luminal Ca^{2+} deficit, the process of store - operated Ca^{2+} entry is triggered. During this process, stromal interaction molecule 1 (STIM1) - an ER protein with a luminal Ca^{2+} sensor - oligomerizes in regions of the ER adjacent to the plasma membrane. In these regions, clustered STIM1 proteins capture Orai1 subunits located on the plasma membrane, which then organize into active Ca^{2+} release-activated channels (CRAC) (Parekh and Penner 1997; Zhang et al. 2005). Next, CRAC facilitates the entry of the extracellular Ca^{2+} and elicits a prolonged (minutes to hours) rise in $[Ca^{2+}]_i$ (Maul-Pavicic et al. 2011; Quintana et al. 2011). A notable consistency can be observed in the elevation of $[Ca^{2+}]_i$ along the IS, with levels approximating 2 μM (Vaeth, Kahlfuss, and Feske 2020). A principal mechanism underlying CTL-mediated killing is the orchestrated release of cytotoxic granules (CGs), which are specialized secretory vesicles containing enzymes and other proteins (Henkart 1985). These particular CGs fall within a category of unique lysosomes, which are designated secretory lysosomes (Blott and Griffiths 2002).

1.6 CGs

1.6.1 Origin

CGs and lysosomes originate from the endo-/lysosmal compartment. CG maturation is thought to begin with early endosomes (EE), which contain T-cell receptors and Soluble N-ethylmaleimide sensitive factor attachment protein receptor (SNARE), probably derived by fusion with endocytic vesicles. CG cargo of granzymes is transported from the Golgi (Griffiths and Isaaz 1993) to EE by mannose 6-phosphate receptor-mediated sorting, whereas the entry pathway for Perforin is unknown. During the maturation of the EE into the late endosome (LE), the molecular labeling (Poteryaev et al. 2010) changes from Ras-related in brain 5 (Rab5) to Rab7, then they become multivesicular with one or more dense core (Gruenberg and Stenmark 2004) representing the final maturation step of LE (Peters et al. 1991).

1.6.2 Release of CG

Upon contact with a target cell, CGs in CTL are transported to the IS in a process known as docking. After docking, the CGs are subjected to priming, a process dependent on Munc13-4 in CTL (Feldmann et al. 2003), to prepare them for fusion.

1.7 SNAREs

The core molecular machinery that is responsible for vesicular fusion is mediated by the SNARE proteins. These proteins were first isolated and characterized by Kaiser and Schekman (1990) in yeast and subsequently by Burkhardt et al. (1990) and Weber et al. (1998) in mammals. The research about SNARE proteins has been further advanced by studies of the impact of clostridial neurotoxins, including tetanus and botulinum toxins, on neuronal function. These toxins have been shown to cleave specific SNARE proteins, thus inhibiting the release of neurotransmitter (Niemann, Blasi, and Jahn 1994; Schiavo et al. 1992). In T cells, the SNARE complex is constituted of a vesicular SNARE (v-SNARE), the vesicle-associated membrane protein 7 (VAMP7) in humans, and VAMP2 (ie. Synaptobrevin-2) in mice (Chitirala, Chang, et al. 2020; Matti et al. 2013), and two target SNAREs (t-SNAREs), the synaptosome-associated protein -23 (SNAP-23), and the syntaxin11 (Figure 4), which are both localized on the plasma membrane. VAMP7/VAMP2 and syntaxin-11 each contribute a single SNARE motif, while SNAP-23 provides two motifs. The assembly of these coiled-coil motifs into a tight four-helix bundle termed the "trans"-SNARE complex, has been demonstrated to secure the synaptic vesicle to the presynaptic membrane (Chang et al. 2023).

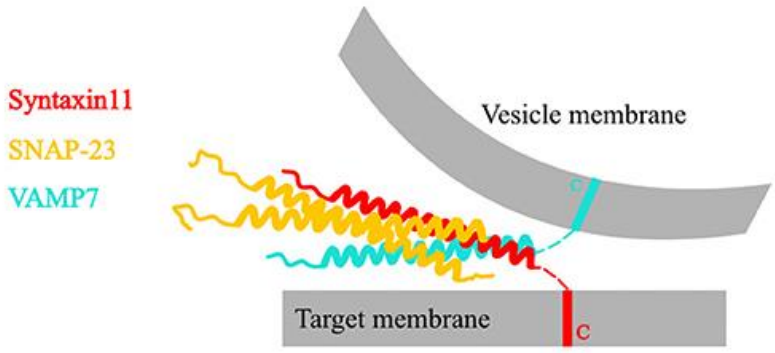

Figure 4: A diagram showing the SNARE complex during the fusion of the cytotoxic granule in human CD8$^+$ T cells.

This image was edited from Chitirala et al. (2019).

It has been shown that synaptotagmins and complexins orchestrate the mode of release in synaptic vesicles in neurons (Krishnakumar et al. 2011). It has been demonstrated that these particular proteins interact with SNARE proteins and induce conformational changes within them. Synaptotagmins, principally located in neurons, function as Ca^{2+} sensors in diverse cell types. These sensors have been shown to regulate SNARE-mediated fusion by impairing it in the absence of Ca^{2+} stimulation

(Burkhardt et al. 1990). Fowler et al. provided evidence for the role of synaptotagmin in lytic granule release, which suggests significant similarities between the mechanisms of neurotransmitter release and lytic granule release (Fowler, Andrews, and Huleatt 2007). In CTLs, synaptotagmin VII is associated with the transport of CG to the plasma membrane (Sleiman et al. 2020).

1.8 Mechanisms of target cell killing by T cells

1.8.1 Prf1/Gzm pathway

The Prf1/Gzm pathway is calcium-dependent, as it requires calcium for the fusion and release of CG content at the IS. The CGs contain molecules responsible for inducing cell death such as granzymes which are serine proteases and membrane-disrupting proteins like Perforin.

1.8.1.1 Perforin-1

Perforin-1 (Prf1) is a pore-forming protein with functional and structural similarities to bacterial toxins (Ivanova et al. 2022; Sauer et al. 1991). Specifically, Prf1 is responsible for creating pores in the target cell membrane, which then enables the entry of granzymes and the subsequent initiation of cell death (Tschopp, Masson, and Stanley 1986).

Perforins contain the membrane attack complex/perforin domain, which is responsible for the pore formation (Voskoboinik, Smyth, and Trapani 2006). At the immune synapse, perforin is secreted by cytotoxic lymphocytes and binds to target cell membranes via its Ca^{2+}-dependent C2 domain, allowing pro-apoptotic granzymes to enter the target cell (Law et al. 2010; Traore et al. 2013). The CTLs are protected from the effects of Prf1 by several mechanisms. Following granule fusion, Cathepsin B is released concurrently with Prf1, moves to the CTL surface, cleaves, and inactivates any Prf1 that might diffuse back (Balaji et al. 2002). In the CGs, Prf1 is inactivated by the pH of the CG, which was shown to range from 5.98 to 6.24 (Chitirala, Ravichandran, et al. 2020), thus preventing their membrane disruption. Once released into the neutral pH of the synaptic cleft, its functionality is restored as documented by Kuta, Reynolds, and Henkart (1989).

1.8.1.2 Granzymes

Granzymes (Gzms) can be classified into three subclasses (the Gzm A, B, and M locus) based on their location on different chromosomes. The most widely expressed in T cells is GzmB. It is located on chromosome 14 in both human and mouse genomes (Hay and Slansky 2022). GzmB has been demonstrated to induce rapid cell death by cleaving caspases (Beresford et al. 2001).

GzmB is synthesized in the cytosol as an inactive zymogen containing an N-terminal Gly-Glu dipeptide that blocks the formation of a catalytic triad (Caputo et al. 1993). Within the Golgi apparatus, the N-linked glycans of pro-GzmB are labeled with mannose-6-phosphate by a phosphotransferase (Griffiths and Isaaz 1993). There, dipeptidyl peptidase I (cathepsin C) cleaves the glycine and glutamic dipeptide

and activates GzmB (McGuire, Lipsky, and Thiele 1993). Next, the active GzmB is deposited on a serglycine backbone (Galvin et al. 1999) under acidic conditions of pH around 5.5 (Burkhardt et al. 1990). Through these events, GzmB activity is controlled within the CTLs until the point of release from the granules (Packard et al. 2007). It has been demonstrated that CTLs can protect themselves from GzmB-mediated killing through the expression of serine protease inhibitors, such as Serpin (Spi6) on their membrane (Zhang et al. 2006).

1.8.2 Fas/FasL pathway

In a Ca^{2+}-independent pathway (Atkinson et al. 1998), the death receptor Fas ligand (FasL), which is located on the surface of CTL, interacts with the Fas receptor (CD95) on the target cell (Purbhoo et al. 2004), thereby triggering programmed cell death and apoptosis through the caspase cascade (Nagata 1996). This pathway is capable of effective killing with only low antigen doses. The Fas pathway supports self-tolerance and survival of CTL by modulating responses to self and foreign antigens (Van Parijs, Peterson, and Abbas 1998), thereby safeguarding T cells from activation-induced cell death (Kataoka et al. 1998).

1.9 Classes of CGs

The utilization of density gradient centrifugation, immune isolation, and mass spectrometry allowed the identification of two distinct classes of fusion-competent CGs: single-core granules (SCGs) and multi-core granules (MCGs) (Figure 5). Morphological distinctions between these categories were discerned through transmission and scanning electron microscopy (Chang et al. 2022). SCGs are characterized by a single dense core of uniform diameter filling out the entire granule, while MCGs feature multiple small cores with diameters varying between 115 and 129 nm (Chang et al. 2022).

Both SCGs and MCGs have considerable quantities of GzmB, with MCGs exhibiting an elevated level of GzmB compared to SCGs. Mass spectrometry demonstrates that SCGs exhibit lysosomal-like characteristics and are predominantly enriched with cathepsins, whereas MCGs display greater heterogeneity and contain proteins typical of the endosomal compartment, such as the Rab family (Chang et al. 2022). Due to protein heterogeneity between SCG and MCG, Chang et al. proposed that variations in protein composition between MCGs and SCGs arise from the existence of two distinct maturation processes, which ultimately result in the formation of two discrete secretory pathways (Chang et al. 2022).

Prf1 and GzmB are released into the IS as two distinct forms in parallel (Bálint et al. 2020; Chang et al. 2022). These forms can be observed and tracked using total internal reflection fluorescence microscopy (TIRFM). They appear as follows: SCG releases their content as a single core fusion event that appears as a cloud of soluble protein rapidly dispersing within the IS. MCG releases its content as a multi-core fusion event, which appears as a small cloud of soluble protein accompanied by a release of several

particles called supramolecular attack particles (SMAPs). It was proposed that SCGs may facilitate the rapid elimination of single target cells, while MCGs are supposedly secreted as a secondary strategy for targets that resist the action of soluble cytotoxic proteins or for killing multiple target cells in a time-delayed manner (Chang et al. 2022).

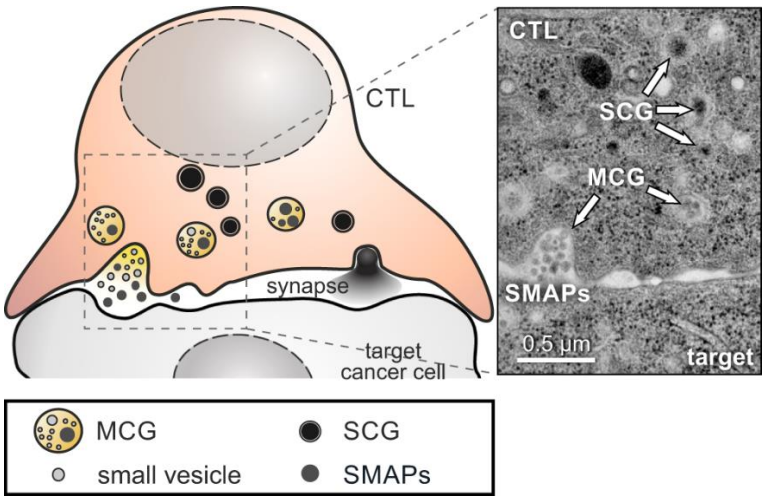

Figure 5: Cytotoxic T lymphocytes use two types of cytotoxic granules in the killing mechanism.

SCGs, which are rapidly diffusible, and MCGs, which deliver intact supramolecular attack particles (SMAPs) to the immunological synapse, as seen in the electron micrograph (Chang et al. 2022).

1.10 SMAPs

Bálint et al. identified SMAPs as particles approximately 120 nm in size, lacking a phospholipid membrane and membrane-associated proteins, including the lysosomal marker LAMP-1 (lysosomal-associated membrane protein 1) that labels CGs. SMAPs are exclusively present in MCGs, not SCGs. SMAPs contain over 285 proteins, including a core of GzmB, Prf1, and serglycin, enclosed within a glycoprotein shell of thrombospondin-1 (TSP-1).

1.10.1 Maturation of SMAPs and their killing mechanism

It is hypothesized that once TSP-1 is released at the cell surface (Kaur and Roberts 2024), it may bind to receptors on the cell surface such as CD36 (Magnetto et al. 1998) or CD47 (Isenberg et al. 2009). It is proposed that TSP-1 subsequently undergo internalization and retrograde trafficking to lysosomes. This process might contribute to the assembly of SMAPs as granule maturity is achieved (Rettig and Baldari 2020). It has been postulated that SMAPs are retained at the IS (Liu, Ye, and Cai 2020) for extended periods, enabling sustained target cell destruction even after the CTL has departed. Along with cytotoxic content within SMAPs, Oldenborg, Gresham, and Lindberg (2001) hypothesized that

SMAPs may form partnerships with myeloid cells, thereby ensuring that any cell that cannot be eliminated by SMAPs is subject to phagocytosis.

1.10.2 SMAP markers

To conduct live-cell imaging using TIRFM, it is necessary to utilize markers for both SCGs and MCGs due to the distinct cargos they carry. The SMAP marker TSP-1 has been demonstrated to be an effective label for SMAPs within MCGs (Chang et al. 2022). Furthermore, each SMAP shell is characterized by a high glycoprotein content, to which wheat germ agglutinin (WGA) specifically binds (Bálint et al. 2020).

TSP-1 is part of the thrombospondin family, which consists of five glycoproteins with functional remodeling characteristics that resemble other extracellular matrix (ECM) proteins. It is a 450 kDa multi-modular glycoprotein produced by the THSB1 gene that was identified as a vital component of platelet α-granules by Baenziger, Brodie, and Majerus (1972). It typically exists as a homotrimer, which consists of three identical subunits that retain TSP-1 in the ECM (Adams et al. 2008). TSP-1 binds to extracellular matrix components such as fibrinogen, fibronectin, laminin, and collagens, as well as integrins and receptors like CD36 (Dawson et al. 1997) and CD47(Roberts et al. 2012) implicated in cell-cell, and cell-matrix interactions (Tan and Lawler 2009).

WGA, a carbohydrate-binding lectin extracted from wheat germ, exhibits binding affinity for N-acetyl-D-glucosamine and N-acetylneuraminic acid (sialic acid) which are present on glycoconjugates and oligosaccharides. WGA binds to cells via its lectin domain by attaching to carbohydrates in the glycocalyx and surface membrane oligosaccharides. Its entry into the cell is facilitated by adsorptive endocytosis.

WGA, a carbohydrate-binding lectin extracted from wheat germ, exhibits a binding affinity for N-acetyl-D-glucosamine and N-acetylneuraminic acid (sialic acid) (Sharon and Lis 1972), which are present in glycoconjugates and oligosaccharides (Mansfield, Peumans, and Raikhel 1988). WGA binds to cells via its lectin domain by interacting with carbohydrates in the glycocalyx and surface membrane oligosaccharides. Its internalization into the cell occurs through adsorptive endocytosis.

1.11 Cytokines

As already stated, the main aim of CTL is killing the target cells through the release of Granzymes and Perforin. However, CTL also secretes a variety of cytokines that support the killing activity and modulate the immune response. These cytokines comprise interferon-gamma (IFN-γ), tumor necrosis factor-alpha (TNF-α), and beta (TNF-β) that contribute to the host defense in multiple ways (Jawed, Dutta, and Majumdar 2019). Furthermore, they also secrete cytokines such as interleukin-2 (IL-2), IL-

15, and IL-7, which are considered to play an important role in the slow and steady homeostatic proliferation of $CD8^+$ memory T cells (Kaech, Wherry, and Ahmed 2002).

1.11.1 Interferon-gamma (IFN-γ)

The two types of interferons are classified based on receptor specificity and sequence homology. IFN- γ is a proinflammatory cytokine that represents the type II interferons (Schoenborn and Wilson 2007). In vivo production of IFN-γ was attributed exclusively to $CD8^+$, $CD4^+$ T cells and NK cells.

In addition, recent evidence indicates that additional cell types, including B cells and APCs, are also capable of secreting IFN-γ (Rastogi et al. 2022). IFN-γ production is controlled by cytokines, such as IL-12 and 18, secreted by APCs. The receptor for IFN-γ (IFNGR) is a protein complex heterodimer, expressed in immune and non-immune cells (Villegas-Mendez et al. 2011). It comprises two IFNGR1 chains, responsible for ligand binding, and two IFNGR2 chains, which mediate signal transduction. It affects a variety of intracellular events in $CD8^+$T cells. These events include enhancing the ability of CTLs to kill using Fas/FasL in the absence of perforin (McKenzie et al. 2006). Bhat et al. (2017a) demonstrated that IFN-γ directly enhances MHC-I expression on target cells thereby boosting the overall T-cell-mediated killing.

1.11.2 Tumor necrosis factor alpha (TNF-α)

TNF-α is a proinflammatory cytokine that is expressed by various cell types after infection, including $CD8^+$ and $CD4^+$ T lymphocytes, NK cells, and DCs (Tracey and Cerami, 1994). Ye et al. (2018) documented the accumulation of TNF-α within the first few hours (5 hours) as a result of TCR engagement from naïve $CD8^+$ T cells. There are two TNF receptors, TNFR1, which is widely expressed in almost all cell types, whereas TNFR2 is mainly restricted to immune cells (Siegmund et al. 2016) and certain tumor cells (Uhlén et al. 2005). TNFR1 possesses a death domain that drives apoptosis and triggers nuclear factor kappa-light-chain-enhancer of activated B cells (NFκB)-driven inflammatory pathways. While TNFR2 lacks a death domain, it exerts a weak stimulatory effect on NFκB. TNF-α signaling influences the various phases of the immune process, including innate immune activation, dendritic cell maturation, and recruitment (Wajant, Pfizenmaier, and Scheurich 2003), T cell priming (Bromberg, Chavin, and Kunkel 1992), T cell proliferation (Boyman et al. 2004) and T cell function (Kägi et al. 1999). These effects in T cells are thought to occur through the increased activation of NF-κB signaling pathways, which impacts all these functional responses of T cells (Schütze et al. 1995). In addition, TNF-α enhances cytokine production and increases IL-2R levels (Scheurich et al. 1987; Yokota, Geppert, and Lipsky 1988).

1.11.3 Interleukin 2 (IL-2)

IL-2 is a pleiotropic cytokine, which is produced by activated T cells (Keene and Forman 1982) in the thymus. There are two distinct types of IL-2 receptors: a trimeric high-affinity IL-2Rαβγ receptor and a dimeric intermediate-affinity IL-2Rβγ receptor. The IL-2Rβγ receptor is widely and consistently expressed in various immune cells, including $CD4^+$ T cells, $CD8^+$ T cells, regulatory T cells, NK cells, and innate lymphoid cells. In addition, the IL-2Rαβγ receptor is uniquely expressed on Tregs and transiently expressed on activated T cells (Abbas et al. 2018). T cells in the resting state principally express intermediate-affinity IL-2 receptors. Upon binding of IL-2 to its receptor, it induces cytolytic activity, cell growth, and IL-2Rα transcription, thus forming high-affinity IL-2 receptors on activated T cells and amplifying their sensitivity to IL-2 (Liao, Lin, and Leonard 2013). In vitro, IL-2 has been demonstrated to enhance T-cell proliferation and differentiation (Gillis and Smith 1977; Smith 1988). Furthermore, IL-2 activates the mechanistic target of rapamycin complex 1 signaling pathways, resulting in elevated biosynthesis of inflammatory cytokines, cytolytic molecules and improved glucose metabolism in CTLs (Mitchell, Ravkov, and Williams 2010; Liao, Lin, and Leonard 2013). Proinflammatory cytokines like IFN-γ, IL-12, and type-1 interferons (IFN-α/β) work in conjunction with IL-2 to play critical roles in immune responses to intensify the effectiveness of the immune system (Jorgovanovic et al. 2020).

1.11.4 Interleukin 6 (IL-6)

IL-6 is a proinflammatory pleiotropic cytokine produced in response to external stimuli, including trauma, stress, and infection (Kishimoto 2005). It is originally identified as B cell stimulating factor-2, which triggers the differentiation of activated B cells into immunoglobulin-producing plasma cells (Kishimoto 1989). Multiple cells produce IL-6, including T cells, B cells, macrophages, dendritic cells, and epithelial cells (Mihara et al. 2012). The heterodimer of the IL-6 receptor is composed of IL-6Rα and the common cytokine receptor gp130 (Boulanger et al. 2003). According to Diehl et al. (2012), IL- 6 also inhibits T-helper type 1 cell differentiation and IFN-γ production through an independent mechanism. It also plays a central role in modulating $CD4^+$ Th cell differentiation and effector functions (Dienz and Rincon 2009). In contrast to $CD4^+$ T cells, little is known about the possible effect of IL-6 on $CD8^+$ T cells. IFN-γ can induce IL-6 receptor expression to enhance the immune response during infection (Suto et al. 2008; Rincon and Irvin 2012). It is reported that IL-6 suppresses activation-induced cell death by downregulating Fas and FasL in an IL-2-independent manner (Adkins et al. 1996; Ayroldi et al. 1998).

1.11.5 Interleukin 10 (IL-10)

IL-10 is an anti-inflammatory cytokine with structural similarities to IFN-γ. It is thought to be a general immunosuppressive cytokine that down-regulates cellular immune responses by acting on APCs and T

cells (Buelens et al. 1995; Moore et al. 1993). The IL-10 receptor (IL10R) is composed of two molecules of an IL-10-specific alpha chain IL10Ra and two molecules of IL10Rb, which are associated with other cytokines (Oft 2019). IL-10R is expressed on the surface of most hematopoietic cells, including B cells, T cells, and macrophages. IL-10 production in T cells is known to be enhanced by various cytokines including IL-2, IL-7, IL-4, IL-15 (Cohen et al. 1997), IFN-α (Schandené et al. 1997; Schandené et al. 1996) and IL-12 (Peng, Kasran, and Ceuppens 1997). A study by Mumm et al. (2011) stated that IL-10 promotes the expression of IFN-γ in $CD8^+$ T cells, leading to elevated MHC I and MHC II expression paradoxically. IL-10 regulates $CD8^+$ T cells through post-translational modifications, which modulate TCR sensitivity (Smith et al. 2018) and positive effect on $CD8^+$ T cell cytotoxicity (MacNeil et al. 1990).

1.12 Cyclosporin A (CsA)

Immunosuppressive drugs have the potential to disrupt various cytokine production and fall into four main classes that contain glucocorticoids, mechanistic target of rapamycin inhibitors, antiproliferative compounds, and calcineurin inhibitors (Hartono, Muthukumar, and Suthanthiran 2013). Calcineurin inhibitors consist of CsA and tacrolimus. (Azzi, Sayegh, and Mallat 2013). Cyclosporine, a cyclic undecapeptide, was initially extracted from the soil fungus *Tolypocladium inflatum* in the 1970s (Borel et al. 1994). By 1983, CsA was synthesized and recognized as an immunosuppressant in organ transplantation. Subsequently, over 30 CsA analogs with diverse biological activities, including antifungal, antiviral, and antiparasitic properties, have been synthesized (Survase et al. 2011).

Calcineurin is a regulator of CTL activity by modulating several molecular pathways. A recent study by Otsuka et al. (2021) has demonstrated that calcineurin influences LFA-1 activation, T-cell proliferation, and perforin production at the TCR level. In activated T cells, calcineurin affects the Nuclear Factor of the Activated T cells (NFAT) family of transcription factors by dephosphorylation, which promotes their translocation to the nucleus. Once in the nucleus, NFATs promote the transcription of several immune response genes, including cytokines such as IL-2, TNF-α, IFN-γ, and cell surface molecules such as CD25 (IL-2Rα). As a calcineurin inhibitor, CsA indirectly targets calcineurin via forming complexes with cytosolic proteins called immunophilins, specifically CsA-cyclophilin A. This interaction impairs the calcineurin-NFAT pathway, blocking NFAT-dependent gene expression and interfering with T-cell proliferation and pro-inflammatory cytokine production (Lee, Kim, and Choi 2018). The inhibitory activity of CsA may provide a new way to study the influence of cytokines on the cytotoxic activity of CTLs. It might also help to understand the release of CGs over time in culture.

1.13 Rationale and Aims of the Project

Cytotoxic T lymphocytes (CTLs) play a critical role in immunotherapy by specifically targeting and eliminating infected or cancerous cells, enabling precise treatment while protecting surrounding healthy tissue. Their potential in personalized therapies and long-term immunity is well recognized. Recent research by Bálint and colleagues has discovered a new capability of CTLs: a lytic cargo enclosed in a glycoprotein coat, that enhances their ability to target cells more aggressively (Bálint et al. 2020). However, challenges persist in utilizing CTLs for immunotherapy, including immune evasion by tumors and viruses, as well as manufacturing limitations and potential toxicity. The discovery of supramolecular attack particles (SMAPs) offers a highly promising alternative, with the potential to specifically kill cancerous or virally infected cells without directly modulating CTLs. However, difficulties remain in producing adequate quantities of SMAPs for use in therapeutic applications. The overall aim of my study is to investigate the factors influencing CTL cytotoxicity, with a special focus on CTL maturation and cytokine production. Additionally, I aim to explore strategies to enhance their function, particularly by inducing the production of SMAPs, to achieve more effective immunotherapies without the need for extensive ex vivo expansion.

2. Materials and Methods

2.1 Materials

Product	Company
(Δ9-Cis) PC (DOPC) $C_{44}H_{84}NO_8P$	Avanti Polar Lipids
10 N NaOH sodium hydroxide	Merck
1N HCL Hydrochloric acid	Merck
1N NaOH solution	Roth
1xPBS	Invitrogen
AIM VTM Medium	GIBCO
Ammonium chloride	Merck
Biotinyl Cap PE-(CAPBIO) $C_{57}H_{102}N_4O_{11}PNaS$	Avanti Polar Lipids
Bovine Serum Albumin (BSA)	Sigma-Aldrich
Calcium chloride dihydrate	Merck
Casein	Sigma Aldrich
Cyclosporin A (CsA)	ENZO-Life science
D-Glucose monohydrate	Merck
DGS-NTA (Ni) C53H93N2O15Ni	Avanti Polar Lipids
Dimethyl sulfoxide (DMSO)	Sigma-Aldrich
E64- protease inhibitor	Merck Millipore
EMbed-812 Epoxy Embedding Kit with DMP-30	Science services
EZ-Link™ Sulfo-NHS-LC-Biotin	Thermo Fisher Scientific
Fetal Calf Serum (FCS)	Invitrogen
GlutaMAX™ Supplement	Thermo Fisher Scientific
HEPES	Thermo Fisher Scientific
Hydrogen peroxide H_2O_2	Merck
Intercellular Adhesion Molecule-1 (ICAM-1)	The Kennedy Institute of Rheumatology Prof. Dustin
Interleukin-2 mouse recombinant (IL-2)	Thermo Fisher Scientific
Isopropanol 99,8%	Carl Roth
$MgCl_2$	Merck
$Na_2HPO_4 \times H_2O$	VWR
NaCl	Merck
Opti-MEM-GlutaMAX	Thermo Fisher Scientific
Osmium tetroxide	Carl Roth

Paraformaldehyde	Merck
PBS-Puffer (10xDulbelcco´s)-Pulver	AppliChem
Pefabloc	Merck Millipore
Penicillin/Streptomycin (10000 U/mL, 10 mg/mL)	Thermo Fisher Scientific
Pepstain A	Merck Millipore
Phosphate-buffered saline (DPBS, 1X), Dulbecco's formula	Thermo Fisher Scientific
Poly-L-ornithine (PLO)	Sigma-Aldrich
Potassium bicarbonate-$KHCO_3$	Merck
Potassium chloride	Sigma-Aldrich
RPMI Medium	GIBCO
Streptavidin	Europa Bioproducts
Sulfuric acid 95-98% H_2SO_4	VWR
Tris	Roth
TRIzol	Thermo Fisher Scientific
Uranyl acetate	Science services
β-Mercaptoethanol (BME)	Roth

2.1.1 Kits

Kit	**Company**
Dynabeads™ FlowComp™ Mouse $CD8^+$ Kit	Thermo Scientific
DynabeadsTM Mouse T-Activator CD3 /CD28	Thermo Scientific
LEGENDplex™ MU Th1 Panel (5-plex) w/ VbP V03	BioLegend
Nucleofection kit for mouse T-lymphocytes	Lonza
RNaseOUT™ recombinant ribonuclease inhibitor	Thermo Scientific
SuperScript™II Reverse Transkriptase	Thermo Scientific

2.1.2 Antibodies

Antibodies	Host	Immunogen	Manufacture and catalogue number	Working Dilution
APC Rat Anti-Mouse CD44	Mouse	Dexamethasone-induced, SJL mouse spontaneous myeloid leukemia M1 cells	BD Pharmingen 559250	1:200
Biotinylated-anti-mouse CD3ε	Mouse	H-2Kb specific cytotoxic T lymphocyte clone BM10-37	BD Pharmingen, clone 145-2C11	10 µg/mL
FITC Rat Anti-Mouse CD62L	Mouse	C3H/eb mouse B lymphoma 38C-13	BD Pharmingen 553150	1:200
PE Rat Anti-Mouse CD25	Mouse	IL-2-dependent BALB/c mouse helper T-cell clone HT-2	BD Pharmingen 558642	1:400
Purified NA/LE Hamster Anti-Mouse anti-CD3ε	Armenian Hamster IgG, κ	TNP-keyhole-limpet hemocyanin	BD Pharmingen 553968	30 µg/mL
Ultra-LEAF™ Purified Anti-mouse-IFN-γ antibody	Armenian Hamster	Recombinant-full-length murine IFN-γ	Biolegend 513208	1:200

2.1.3 Solutions

Culture medium	AIMV	90%
	FCS	10%
	2-Mercaptoethanol	50 µM
	Pen/Strep	0.5%
	Opti-MEM-GlutaM	
Inhouse-Complete transfection media	FCS	10%

	HEPES	10 mM
	sodium pyruvate	1 mM
	DMSO	1%
	NH_4Cl	155 mM
Erythrocyte lysis buffer	$KHCO_3$	10 mM
	EDTA	50 mM in H_2O
		pH 7.4
	NaCl	155 mM
Low calcium extracellular buffer	KCl	4.5 mM
	HEPES	5 mM
	$MgCl_2$	3 mM
	D-Glucose monohydrate	10.1 mM
		(Osmolarity:
		300-310 mOsm)
		pH: 7.4
	NaCl	140 mM
High calcium extracellular buffer	KCl	4.5 mM
	HEPES	5 mM
	$CaCl_2$	10 mM
	D-Glucose monohydrate	10.1 mM
		(Osmolarity:
		300-310 mOsm)
		pH: 7.4
	AIMV	2 mL
EM-Freezing medium	FCS	30%
	HEPES	10 mM
	25x Human Serum Albumin (HSA)	1%
HBS/HSA buffer	HEPES buffer containing	50 mL
	10 x HBS	0.5 mM
	1M $CaCl_2$	1 mM
	1M $MgCl_2$	2 mM
	$Na_2HPO_4 \times 2H_2O$,	58 mM
Isolation Buffer	$NaH_2PO_4 \times H_2O$	17 mM
	0.1 % BSA	0.5 g
	EDTA s	2 mM
		(Bzeih, 2016).

Liposome preparation	25% NTA (Stock = 0.4 Mm)	83.75 mM
	100% DOPC (Stock = 0.4 Mm)	130 mM
	2% Capbio lipids (Stock = 0.4 Mm)	200 mM
Mounting medium	Glycerol,	6 g
	Mowiol 4-88	2.4 g
	H_2O	6 mL
	Tris-HCl buffer	12 mL of 0.2 M (pH 8.5)
Nucleofection Solution (Lonza) Transfection	Mouse T Cell NucleofectorTM	90%
	Component A	1%
	Component B	1%
	FCS	5 %
	GlutaMAX	2 %
10 x HBS	HEPES (1M)	200 mM
	NaCl	pH7.2
	KCl	1.37 mM
	Na2HPO4 x H_2O	50 mM
	D-Glucose x H_2O	7 mM
		60 mM
1x PBS	Na_2HPO_4 x $2H_2O$	58 mM
	NaH_2PO_4 x H_2O	17 mM
	NaCl	83 mM
	$CaCl_2$	0.5 mM
	$MgCl_2$	2 mM
		(Osmolarity 321 mosm)
		pH 7.4
Paraformaldehyde (2%)	PFA 4%	6 mL
	1x PBS 6 mL	Up to 12 mL
	PFA	1.2 g
Paraformaldehyde (4%)		
	1x PBS	5350 mM

	10N NaOH	10,000 mM
	1N HCL	1000 mM
		pH 7.4
	H_2O_2	30%
Piranha solution	Sulfuric acid	70%
	FCS	10%
RPMI buffer- $CD8^+$T cell Isolation	2-Mercaptoethanol	50 µM
	Pen/Strep	0.5%
	HEPES	10 mM
	Modified biotin in 0.1% BSA	
	EDTA	2 mM
	Pepstatin A	1mg/mL (in DMSO)
Protease inhibitors	E64	10 mM (in water)
	4-benzenesulfonyl fluoride hydrochloride (Pefabloc SC)	in H_2O or equivalent.
	Store separately at -20°C	
Fixation	PFA in 1X D-PBS	4%
	NaOH	20 µl,
		pH 7.4

2.1.4 Consumables

Product	**Company**
24 well plate	Greiner Bio-One
5 mL Syringes	Henke-Ject Luer
6 well plate	Greiner Bio-One
Bath incubator	Julabo
BD Roundfilter (70 µm)	Becton Dickinson
Cell Strainer Sterile 70 µm Pore	Greiner Bio-One - EASYstrainer
Closure clips for dialysis tubes 45 mm wide	Neo Lab
Copper grids	Plano
Coverslip (15 mm in diameter)	Paul Marienfeld
Coverslip (25 mm in diameter)	Paul Marienfeld

Dialysis Membrane -Standard RC Tubing-6-8 kD	Fisher Scientific/ Spectrum labs
DynaMag^{TM}-15-Magnetic particle Concentrator	Invitrogen
Filter 0,45 Filtropur V50	Sarstedt
Filter 0.2 µm	Pall /VWR
Acrodisc PF Syringe Filter with 0.8 / 0.2 µm Super Membrane Non-Pyrogenic-Size-32mm.	
Flat specimen carrier	Leica
Microscope Slide	Roth
Neubauer chamber	Brand Gmbh
Nexterion Coverslip Glass D	Schott
Ni nets or carbon	Plano
Parafilm® M Sealing Film	Merck
Pasteur Pipette-2 mL	Falcon
Petri Dish-size 150 mm × 15 mm	Greiner Bio-One
pH indicator paper	Carl Roth
Pipette Filter Tip (10 µL, 200 µL, 1000 µL)	Sarstedt
Polyallomer Centrifuge Tubes	Beckmann Coulter
Polypropylene Centrifuge Tube 15 mL/ 50 mL	Greiner Bio-One
QPCR plates	Axon labortechnik
QPCR seal membrane	Axon labortechnik
Sapphire disks in flat specimen carriers (1.5 mm×0.1 mm)	Leica
Slide-A-Lyzer® Dialysis Cassettes	Thermo Scientific
Sticky-Slide VI (ibidis VI)	ibidi
SurPhob Tips, 200 µL, 1000 µL , sterile	Biozym
V-plate V03	BioLegend
Wheaton Coplin staining jars	Merck

2.1.5 Plasmids

Plasmid	**Concentration**
pMAX- GzmB-L-pHuji	Stock concentration (4.8 µg/µL)
pMAX-TSP-1-GFPSpark	Stock concentration (4 µg/µL)

2.1.6 Software

Software	Company
BD FACSAria III analyzer	BD (Becton, Dickinson and Company) Biosciences
BD FACSDiva 6.0	BD Biosciences
Bio-Rad EFX Manager 3.0	Bio-Rad Laboratories
CorelDRAW Graphics Suite 2021	Corel Corporation
FlowJo v10.0.7	BD Biosciences
Igor Pro, version 6.37	Wavemetrics
ImageJ version 1.53c	National Institutes of Health (NIH)
Office 2016	Microsoft Corporation
LEGENDplex™ Data Analysis Version 8.0	BioLegend
Olympus iTEM5.0 image (version, build1243).	Olympus Corporation
SigmaPlot, version 14.5	Systat Software
Visiview -Version:4.0.0.11	Visitron GmbH
Zeiss Efficient Navigator (ZEN) 2012	Carl Zeiss
Just Another Colocalization Plugin (JACoP) v2.1.4 Plugin	National Institutes of Health (NIH)
GraphPad Prism 9.1.2	GraphPad Software, Inc

2.1.7 Mouse strains

C57BL/6N	Stock Number: 005304, The Jackson Laboratory
GzmB-tdTom-KI	Background C57BL/6N

Mice of both sexes (C57BL6/N and GzmB-tdTomato-KI) were used in this study. They were housed at 22°C room temperature (RT) with 50-60% humidity and a standard 12-hour (h) light/dark cycle. They were maintained under specific pathogen-free (SPF) conditions and given food and water ad libitum.

2.1.8 Devices

Device	Company
32°C/ 5%CO_2 incubator- Hera cell	Thermo Fisher Scientific
37°C/ 5%CO_2 incubator- Hera cell	Thermo Fisher Scientific
AF 103X Safe	Scotsman
Argon gas	Nippon gases
Automatic Freeze Substitution (AFS2)	Leica
Avestin Extruder	Lipofast
Bath Incubator	Memmert
Centrifuge 5804 R	Eppendorf
Centrifuge mini spin plus	Eppendorf
DENovix spectrophotometer	DENovix Inc
DN100 Digital Net Camera Microscope	Nikon
Electron Microscope (Tecnai G2 Biotwin electron microscope)	Thermo Fisher Scientific
Fluorescence-Activated Cell Sorting (FACS)	BD Biosciences
Fridge/Freezer	Liebherr
Heated Magnetic Stirrer	IKA-Combimag RCT
Hera Freeze Heraus -80ºC	Thermo Fisher Scientific
Heraeus Labofuge 400 R centrifuge	Thermo Fisher Scientific
High Pressure Freezer (HPF) (EM PACT2)	Leica
IKA Shakers	IKA (Vortex 2)
Laminar Flow Hood	Thermo Fisher Scientific
Microwave	Severin
MilliQ-Direct Water Treatment System	Merck
Mini Centrifuge –Colour Sprout Plus Package	Biozym
Nucleofector Machine (Program: TCells ($CD8^+$) Mouse X-001)	Amaxa
Nucleofector™ 2b Device	Lonza
PCR Working Station Pro	Peqlab
pH Meter	Scott
Plasma cleaner PDC-002-CE	Harrick plasma
Plasmaflo Gas (PDC-FMC-2)	Harrick plasma
QPCR CFX96	Bio-Rad.lab

Rotating Mixer	Heidolph Reax2
Rotator	neolab
Structured Illumination Microscopy (SIM)	Zeiss
Total Internal Reflection Fluorescence microscopy (TIRF)	Visitron Systems GmbH
UltraMicrotome EM UC7	Leica
Vacuum Pump	KNF Neuberger Lab
Vortex Mixer 7-2020	neolab

2.1.9 Primer design for qPCR

Primer name	**Sequence (5' to 3')**	**Expected size (bp)**
TSP-1	NM_011580.4	204
Forward Primer	TGTGAGGTTTGTCTTTGGAA	870-889
Reverse Primer	ACCATGCTGGATAGTTCATC	1073-1054
IFN-γ	NM_008337	184
Forward Primer	GAACGCTACACACTGCATCT	112-131
Reverse Primer	GTCACCATCCTTTTGCCAGT	295-276

Primer from Qiagen:

Primer name	**Gene**	**QuantiTect primer**
TATA-box binding protein (TBP)	mTBP	Mm_Tbp_1_SG /QT00198443

2.2 Methods

2.2.1 Primary $CD8^+$T cell Isolation

All experimental procedures were performed and approved according to the regulation of the state of Saarland (Landesamt für Verbraucherschutz, AZ: 2.4.1.1). Murine CTLs were prepared via positive isolation from splenocytes through the following protocol. Mice (C57BL6/N, GzmB-tdTomato-KI, Charles River Laboratories) were euthanized by cervical dislocation after they were anaesthetized with CO_2 (AVMA guidelines 2007). Splenocytes were isolated from 8 to 13-week-old C57/BL6N or GzmB-tdTomato-KI mice, depending on the experiment (Dudenhöffer-Pfeifer et al. 2013). The spleen was extracted and smashed into splenocytes with a 3 mL syringe. Then, it was sieved through a 70 µm cell strainer (Corning Life Science) directly into a Petri dish filled with 2 mL preheated RPMI buffer (37°C). The splenocytes were transferred into a 15 mL Falcon tube and filled with RPMI till 10 mL. The cell suspension was spun down for 6 min at 1100 rpm with no brake applied. The supernatant was carefully

removed, and the pellet was resuspended for 30 seconds in 1 mL of Erylysis buffer to lyse the erythrocytes. This reaction was stopped by adding 9 mL warm RPMI. The suspension was spun down for another 6 minutes at 1100 rpm. After discarding the supernatant, the pellet was resuspended in 500 µL of Isolation buffer (IB). The positive isolation of the $CD8^+$ T cells is performed as follows. 25 µl FlowComp™ $CD8^+$ antibody was added to bind to the $CD8^+$ T cells. This mixture was incubated on ice for 10 minutes. Then, 6 mL of IB was added and the cell suspension was spun down at 1100 rpm for 8 minutes. The supernatant was removed, and the pellet was re-suspended in a mixture of 1 mL IB and 75 µl of FlowComp™ Dynabeads (Invitrogen). That mixture was incubated for 15 minutes on a rocker at 6°C cold room. The suspension was positioned for 2 minutes on a magnet to be able to fix the bead-bound $CD8^+$ T cells on the side of the tube, allowing it to discard the unbounded cells. The bead-bounded $CD8^+$ T cells were released from the beads by using 1 mL of FlowComp™ Release buffer on a rotator at room temperature (RT) for 10 minutes. The supernatant was placed in a magnet for 2 min to get the bead-free $CD8^+$ cells. This step was repeated to remove any residual beads. In the end, the naïve $CD8^+$ T-lymphocytes were collected by centrifugation for 6 min at 1100 rpm.

2.2.2 Primary T lymphocyte cell culture

Isolated naïve $CD8^+$ T lymphocytes were cultured at a density of 1×10^6 cells\ mL of culture medium in a 24-well plate. The culture medium consisted of AIM V medium supplemented with 10% FCS, 50 µM 2-mercaptoethanol (BME), and 100 U/mL of recombinant mouse Interleukin-2 (IL-2). Antibody-coated beads of anti-CD3/anti-CD28 antibody were added with a bead-to-cell ratio of 1:0.8 (number of cells: activator beads). Cells were maintained at 37°C with 5% CO_2 (saturated humidity) until day 9. However, in some experiments, cultures were maintained only until day 7. After day 2, cells were counted every day and split to be at a density of 1 $x10^6$ CTLs/1 mL of freshly prepared culture medium as mentioned above.

2.2.3 Restimulation protocol

Day 5 bead-activated GzmB-tdTomato-KI CTLs were collected, and beads were removed using a magnet. Afterward, CTLs were counted and incubated with fresh anti-CD3/anti-CD28 coated beads with a ratio of 1: 0.8 and AIM V medium with 10% FCS, 50 µM BME with no IL-2 for 4 h at 37°C. Later, the added beads were removed and CTLs were washed twice with warm IB at 900 rpm for 6 minutes to remove the dead cells. Then, CTLs were incubated with a fresh AIM V medium with 10% FCS, 50 µM BME, and 100 U/mL of recombinant mouse IL-2. After 12 h of incubation at 37°C and 5 % CO_2, CTLs were used either for TIRFM imaging or flow cytometry.

2.2.4 Suppression of the cytokine production with the use of Cyclosporin A (CsA)

A stock solution concentration of 100 µg/µL was prepared by dissolving 0.05 g CsA into 500 µL dimethyl sulfoxide (DMSO) and stored at -20°C. Isolated $CD8^+$ T-lymphocytes were cultured at 10^6 cells in AIM V medium containing 10% FCS, 50 µM BME, and 100 U/mL IL-2 in a 24-well plate. On day 2, the culture was separated into two batches; the first batch was the control (untreated group), which was cultured with AIM V medium supplemented with 10% FCS, 50 µM BME, and 100 U/mL IL-2 from day 2 till day 7. The second batch represented the $CD8^+$ T cells treated with CsA at a final concentration of 5 µg/mL according to Hajkova et al. (2017). To do so, 0.05 µL of the stock solution was added to the 1 mL medium. The second batch was treated daily with CsA starting on day 2 till day 7. To evaluate the exocytosis function of the control and the CsA treated T cell, $CD8^+$ T cells from both batches were electroporated with pMAX-GzmB-L-pHuji on days 3 and 7 and imaged on the following days (days 4 and 8) using TIRFM. Supernatant was collected on days 4 and 8 to study the effect of CsA on the secreted cytokines in the culture medium. 600 µL of the cell suspension was pipetted from the cultured CTLs on days 4 and 8 and centrifuged at 1100 rpm for 6 minutes after removing the beads with a magnet. Next, 500 µL of the supernatant was added to a mixture of protease inhibitors and then immediately frozen at -80°C. That mixture consisted of 0.5 µL Pepstatin A, 0.5 µL E64, and 2.5 µL Pefabloc and was added to prevent degradation of the cytokines before analysis. Extracellular cytokines including IL-2, 6, 10, IFN-γ, and TNF-α were measured using Cytokine Multiplex Assay Kits, and flow cytometry was performed.

2.2.5 Treatment of $CD8^+$ T cell culture with anti-mouse IFN-γ antibody

Isolated $CD8^+$ T-lymphocytes were cultured at 10^6 cells in AIM V medium with 10% FCS, 50 µM BME, and 100 U/mL IL-2 in a 24-well plate. On day 2, the culture was separated into two batches; the first batch was the control, which was cultured with AIM V medium supplemented with 10% FCS, 50 µM BME, and 100 U/mL IL-2. The $CD8^+$ T cells of the second batch were treated daily until day 7 with a monoclonal anti-mouse IFN-γ antibody against secreted cytokines at 1:200 dilutions in AIM V medium containing 10% FCS, 50 µM BME, and 100 U/mL IL-2. The exact concentration of anti-mouse IFN-γ antibody used in this experiment was calculated from the highest IFN-γ concentration measured by the LEGENDplex™ kit, approximately 400 Pg/mL from WT day 4. I used 12 times the measured concentration to ensure that all secreted IFN-γ was captured. $CD8^+$ T cells from both batches were electroporated with pMAX-GzmB-L-pHuji on days 3 and 7. T cell exocytosis function was assessed by TIRFM on the following days (4 and 8).

2.2.6 Electroporation protocol

Electroporation was performed on mouse CTLs on days 3, 5, 7, and 9 for some experiments, and on other days 6 or 4 and 8. It was done using the Nucleofector (Amaxa). About 6×10^6 cells were

resuspended with 2.5 µg plasmid DNA (pMAX-GzmB-L-pHuji and or pMAX-TSP-1-GFPSpark*)*. 100 µl electroporation buffer was used from the mouse T cell Nucleofector Kit. The mixture was subsequently transferred into electroporation cuvettes, where electroporation was promptly conducted using the customized X-001 pulse specifically designed for mouse CTLs. Electroporated cells were immediately transferred to 3 mL of pre-warmed recovery medium which was either complete Lonza recovery media including components A and B, supplemented with 10% FCS and GlutaMAX that was used or in-house recovery medium that consists of Opti-MEM-GlutaMAX with 10% FCS, 10 mM HEPES, 1 mM sodium pyruvate, and 1% DMSO. The transfected CTLs were used after 14−18 h at 32°C incubator from the time of transfection. After the incubation period, electroporated CTLs were washed twice with AIM-V medium to remove any dead cells. They were then resuspended in AIM-V medium supplemented with 10% FCS, 50 µM BME, and 100 U/mL IL-2 and placed in a 37°C incubator for the intended time of imaging. This preparation was used to visualize granule secretion at the immunological synapse formed on the supported lipid bilayer (SLB) using TIRFM.

2.2.7 CTL Preparation for Structured Illumination Microscopy (SIM)

On days 3 and 7, $CD8^+$ T lymphocytes from GzmB-tdTomato-KI mice were electroporated with 2.5 µg plasmid DNA, TSP-1-GFPSpark. Immediately after transfection, the CTLs were incubated at 32°C and used 14–18 hours later. After the incubation period, transfected CTLs were washed twice with an AIM-V medium to remove any dead cells. Next, CTLs were suspended in 50 µL low Ca^{2+} extracellular medium. To be able to visualize the cytotoxic granules in the unstimulated and stimulated cell status. CTLs of a density of $0.5−1 \times 10^6$ were added per coverslip in both cell statuses. For the unstimulated cell status, the suspension was settled down on coverslips coated with Poly-L-ornithine (PLO) (the preparation explained later) for 5 minutes, then 200 µL of 10 mM Ca^{2+} extracellular medium was added for an extra 10 minutes. For the stimulated CTLs, the previously mentioned cell suspension in a low Ca^{2+} extracellular medium was settled down on antiCD3ε-coated coverslips (the preparation explained later) for a total period of 15 minutes (5 minutes with low Ca^{2+} extracellular medium and 10 minutes in 10 mM Ca^{2+} extracellular medium). Subsequently, 4 mL of the 2% paraformaldehyde (PFA) solution with a pH of 7.4 was added to each coverslip and incubated for 6 minutes at RT, to immediately fix the CTLs. Afterward, the cells were washed three times with PBS with 4 minutes' interval between each washing step. Lastly, the cells were dipped briefly in distilled water. Through using fine tissue paper, excess water was gently removed by touching. Lastly, the cell side-facing coverslips were embedded using a 15 µL mounting medium for 15 mm coverslips on microscopic slides and were incubated for 10 minutes at 37°C. Next, the microscopic slides were kept at 4°C until imaging using Structured Illumination Microscopy (SIM).

2.2.8 Lipid bilayer preparation

2.2.8.1 Preparation of proteins

2.2.8.1.1 Monobiotinylation of anti-CD3ε antibody

At RT 200 mg/mL of EZ-link Sulfo-NHS-LC-LC-Biotin was diluted in DMSO. It was added to the pure anti-CD3ε antibody solution with an initial concentration of 1 mg/mL. The mixture was then allowed to incubate at RT for 30 minutes. After incubation, the product was purified overnight at 4°C in PBS using a dialysis cassette, and photometric assays were then used to determine the concentration of the resulting solution.

2.2.8.1.2 Intercellular Adhesion Molecule-1 (ICAM-1)

The drosophila S2 cell line expressing ICAM-1 was used to produce mouse ICAM-1 protein, purified from the culture, and the concentration was measured by a photometer. The cell line was provided by Prof. Michael Dustin and purified after S2 induction.

2.2.8.2 Lipids preparation

A lipid buffer that consisted of 100 % DOPC, 25 % NTA, and 2 % Capbio was prepared in separate Eppendorf tubes. Firstly, 188 µL of 100 % DOPC was pipetted in a tube; then, the 25 % NTA was prepared by mixing 211 µl NTA and 188 µl of 100 % DOPC. Finally, the 2% Capbio was made by mixing 7 µl Capbio with 246.6 µl of 100 % DOPC. The lipids were aerated first with nitrogen gas, then with Argon gas, without touching the lipids and the individual tubes were immediately sealed with parafilm. Lipid buffer was dried in a lyophiliser at -40°C for 2 h. Next, the lipid buffer was again aerated with argon gas. These buffers were used to prepare a suspension of liposomes with a range of vesicle sizes. The buffers were extruded 20 times in an Avestin extruder with a 100 nm pore membrane (Lipofast ®) until they became transparent to homogenize the size of the vesicles. This transparency is an indication of the formation of single unilamellar vesicles (SUVs) with a homogeneous particle size distribution. The lipids were sterile filtrated with 0.22 µm filter and diluted with DOPC to a concentration of 18:1 DGS-NTA(Ni), 18:1 Biotinyl Cap, and 18:1 (D9-Cis) PC in specific mixtures at a total lipid concentration of 4 mM.

2.2.8.2.1 Lipid bilayer coating slide preparation

Nexterion glass D coverslips were incubated for 20 minutes in a vertical glass rack with Piranha solution with 50 mL sulfuric acid, then 25 mL hydrogen peroxide was added. The waste of piranha solution was discarded into a glass beaker containing a big volume of water for dilution (1:25) and then discarded. Afterward, coverslips were washed under flowing milliQ water for about 5-10 min and dried by a vacuum pump (Dustin et al. 2007; Valvo et al. 2017). The coverslip was then cleaned for 10 minutes with a plasma cleaner (pressure 300), and the coverslip adhered to Sticky-Slide VI0.4 to form 6 flow

channels. Per slide, 300 µL of the previously prepared liposomes were mixed and added to the 6 wells (50 µL liposomes per well). The lipid was bubbled with argon for 1-2 minutes and sealed with parafilm after use. After 20 minutes, the chambers were washed 3 times with 150 µL HBS/HSA buffer (flow cell buffer). 100 µL of 5% casein was blocked with 100 µM NiSO4 for 20 minutes. This was followed by 7 µL of NiSO4 (10 mM NiSO4 stock) mixed with 700 µL of 5% casein, further washing steps were performed with 150 µL of HBS/HSA buffer 3 times. Then, 2.8 µL of streptavidin (1mg/mL stock), which has a high affinity for biotin, was mixed with 700 µL of HBS/HSA buffer in the above chamber and incubated for 20 minutes. The chambers were washed 3 times with 150 µL of HBS/HSA buffer. Next, 275 ng/mL ICAM-1-405 His-tag protein and 5, 10, 20 µg/mL biotinylated anti-mouse CD3ε was prepared as the following: 0,5 µL ICAM1-405 (stock concentration 0,1mg/mL ICAM-1-405) was mixed with 3 µL (5 µg/mL) 6 µL (10 µg\mL), 12 µL (20 µg/mL) anti-CD3ε antibody (stock 0.58 mg/mL). This mixture was added to 350µL HBS/HSA buffer for 20 minutes followed by a washing step with 150 µL of HBS/HSA buffer that was repeated three times. Immediately before imaging a specific chamber from the SLB, the HBS/HSA buffer was removed from that chamber and $0.5-1 \times 10^6$ $CD8^+$ T-cells in low Ca^{2+} extracellular solution were added per tunnel. All the steps used for SLB preparation were done at $20 \pm 2°C$.

2.2.9 Anti-CD3ε antibody coating of glass coverslips

A 15 mm or 25 mm diameter coverslip was used, depending on the cell density in the cell culture well. Prior to the anti-CD3ε antibody coating, a PLO coating of the coverslips was performed to increase cell adhesion and spreading, which in turn improved the accuracy and consistency of T-cell activation experiments. For the PLO coating, 50 µL of a 0.1 mg/mL solution of PLO was applied per coverslip under a cell culture hood, incubated for 30 minutes at RT, removed by aspiration, and used afterward.

For coverslips coated with anti-CD3ε, the previous step was repeated and followed by the addition of anti-CD3ε coating. The antibody was diluted at a concentration of 30 µg/ mL in PBS, incubated on the coverslip for 2 h at 37°C and used immediately. To assess T-cell CG functionality at the immunological synapse (IS) level, anti-CD3ε antibody-coated coverslips were used to create an IS. In contrast, PLO-coated coverslips were utilized to analyze CGs across the entire cell without stimulation from anti-CD3ε.

2.2.10 Mounting medium

The mounting medium was prepared by dissolving 6 g Glycerol, and 2.4 g Mowiol 4-88 in 6 mL H_2O and stirring for 2 h at RT. 12 mL of 0.2 M Tris-HCl buffer (pH 8.5) was then added and mixed overnight at 53°C. Next, the solution was centrifuged at 1700 × g for 20 min at RT, aliquoted the clear supernatant, and then stored at -20°C.

2.2.11 Total Internal Reflection Fluorescence Microscopy (TIRFM)

TIRFM is a high-performance technique providing high resolution and fast acquisition and minimizes the photobleaching effect on imaging live cells. TIRFM (Steyer and Almers 2001; Steyer, Horstmann, and Almers 1997; Stout and Axelrod 1989; Stemberger et al. 2007; Stinchcombe, Bossi, and Griffiths 2004; Stinchcombe and Griffiths 2007). It enables precise confinement of fluorescence excitation to a 100-300 nm layer adjacent to the coverslip on which the cells are attached. TIRF is based on the behavior of light traveling through an interface between two media with different refractive indices, which is described by Snell's law as follows:

$n(1) \times \sin\theta(1) = n(2) \times \sin\theta(2)$

with n being the refractive indices, θ the angle of the light at the interfaces (Figure 6).

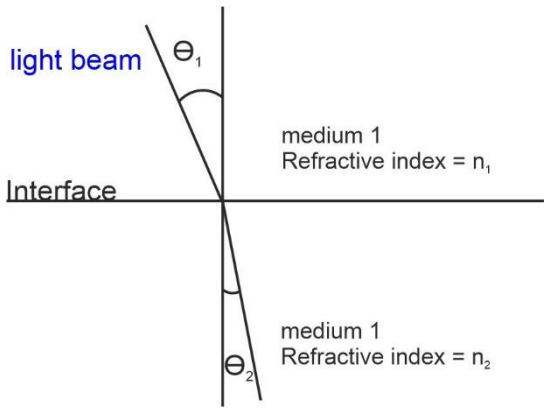

Figure 6: Simple explanation for Snell's Law.

$\theta_1$is the angle of incidence and $\theta_2$is the angle of refraction.

With $\mathbf{n_{(1)}}$ greater than $\mathbf{n_{(2)}}$, at a critical angle $\boldsymbol{\theta_{(c)}}$, then refraction occurs at 90 degrees (sin $\boldsymbol{\theta_{(2)}}$ = 1), and Snell's law reduces to $\theta_c = \sin^{-1}\left(\frac{n_2}{n_1}\right)$

At angles above the critical angle, total internal reflection is achieved, with essentially all light reflected into the first medium. Although the light does not enter deep into the second medium, it passes through the interface, propagating parallel to the surface and generating an electromagnetic field in the second medium immediately adjacent to the interface. This field is called the evanescent field, with a thickness (d) depending on the refractive indices of the angle θ and the light wavelength λ. Furthermore, the light intensity decays exponentially with the distance from the interface. Due to the narrow field depth, the excitation of the fluorophore is only limited to the interface and not to the entire sample, resulting in a higher signal-to-noise ratio image as compared to conventional wide-field epifluorescence illumination (Figure 7). Thereby, TIRFM imaging allows the measurement of the exocytosis of fluorescently marked vesicles and the visualization of the released content, i.e. whether it is dispersed or remains clustered.

The thickness of the evanescent field in our experimental setting can be calculated as follows: the refractive index $n_{(1)}$ of the microscope slide or coverslip is approximately 1.5 as is the immersion oil at 20 ºC, while the refractive index of the aqueous buffer solution of the cells or their cytoplasmic components is $n_{(2)}$ = 1.33 to 1.38 (Figure 7). The light wavelength is between 488 nm and 561 nm therefore the evanescent wave is about 100 to 300 nm thick in TIRFM as verified by Oheim et al. (2019).

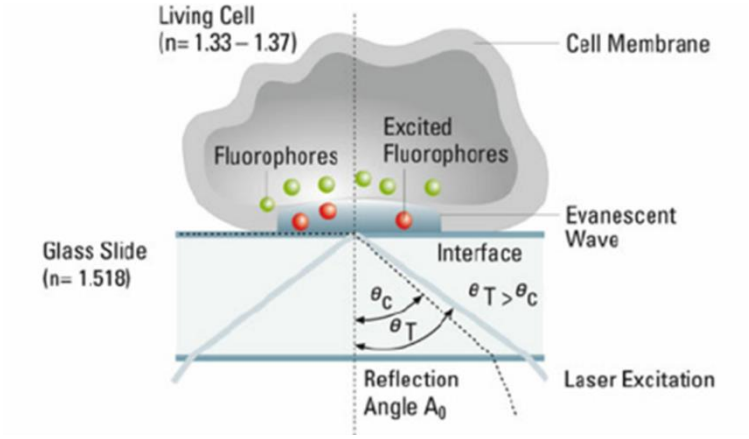

Figure 7: The principle of TIRF microscopy.

θ_C, is the critical angle, θ_T , is the angle of refraction (Parhamifar and Moghimi 2012).

For the TIRFM live cell exocytosis experiments, mouse CTLs were electroporated with GzmB-pHuji and in some experiments co-stained with Wheat germ agglutinin (WGA)-Alexa Fluor 488 as a cytotoxic granule marker.

2.2.11.1 Acquisition Conditions

The exocytosis of the fluorescently labeled vesicles was measured 14–18 h after transfection with the following procedure: 0.5-1 × 10^6 CTLs were suspended in 30 µl of extracellular buffer containing no Ca^{2+}. Afterward, $CD8^+$ T cells were given 2 minutes to settle on the SLB containing anti-CD3ε. The CTLs were imaged for 15 minutes at RT. This included 5 minutes of imaging in the previously cited low Ca^{2+} buffer followed by 10 min of acquisition in the 10 mM Ca^{2+} buffer to boost the vesicle fusion.

In all experiments, 10 µg/mL anti-CD3ε was used, while variable concentrations of anti-CD3ε (5, 10, and 20 µg/mL) were used only to test the effect of the anti-CD3ε stimulus on the fusion mode of CTLs (Table 6).

2.2.11.2 TIRFM setup

The components of the TIRFM setup (Visitrom GmbH) are given in Table 1. The cells were illuminated simultaneously with 488 nm (100 mW) laser to excite WGA-Alexa Fluor 488 and a 561 nm (100 mW) laser solid-state to excite pHuji or tdTomato. A dual-view camera splitter (Optosplit II) was used to separate the red and green channels. The images were taken with an acquisition frequency of about 10 Hz with an exposure time of 100 ms. Secretion was analyzed using ImageJ version 1.53c.

Table 1: TIRFM setup

IX83 inverted microscope	Olympus
UAPON100XOTIRF NA 1.49 objective	Olympus
iLAS2 illumination control system for uniform TIRF illumination	Roper Scientific SAS, France
Prime95B camera	Teledyne Photometrics
Filter cube containing FF444/520/590/Di01 dichroic and FF01–465/537/623 emission filter	Semrock,
Image splitter: OptoSplit II	Cairn
Splitter filter set:	Chroma Technology
590LP long-pass filter, 510/80 bandpass filter	
Controling software: Visiview 4.0.0.11	Visitron GmbH
561 nm 100 mW laser	
488 nm 100 mW laser	

2.2.12 Structured Illumination Microscopy (SIM)

SIM is a super-resolution microscopy technique that overcomes the diffraction limit of light by illuminating the cell with a series of exciting light patterns (gratting), resulting in a grid pattern. The acquisition of subsequent images of the illuminated surface is accomplished through the strategic shifting or rotating of the grid, thereby allowing the reconstruction of high-resolution images that exceed the diffraction limit. High resolution can be obtained through the processing of the acquired images (Monks et al. 1998). The setup was based on the Elyra PS.1 (Zeiss) and controlled by the Zen 2012 software. It was equipped with 63×, 1.4 NA Plan-apochromatic objective. The excitation was provided by laser emitting at 488 nm (HR diode laser), 561 nm (DPSS). The optimal grating was chosen automatically by the acquisition software. SIM illumination mode was adjusted to five phases times five rotations to obtain maximal resolution. Each cell was acquired with a Z-stacks of approximately 50 planes with a step size of 200 nm enabling the reconstruction of a high-resolution 3D image.

2.2.13 Flow cytometry

2.2.13.1 Quantification of different T-cell subsets

CTLs were collected on different days according to the aim of the experiment. For the study of the effect of T-cell maturation, $CD8^+$ T cells from wild-type (WT) or from GzmB-tdTomato-KI mice were collected from days 4, 6, 8, and 10. In some specified experiments, I used $CD8^+$ T cells only from days 4 and 8. 2×10^6 CTLs were collected from the cell culture. Next, the anti-CD3/anti-CD28 activator beads were removed, and the cells were centrifuged at 1100 rpm for 5 minutes. $CD8^+$ T lymphocytes were washed twice with 2 µL cold DPBS (1X) and suspended in 25 µL cold DPBS (1X). The cell suspension was divided into three 1.5 mL Eppendorf tubes. Each tube contained an equal density of approximately 0.5×10^6 CTLs per tube. The three tubes represent control and duplicates of the stained T-cell samples with the corresponding antibodies. CD25-PE was used as a marker of cellular activation and CD44-APC combined with CD62L-FITC to differentiate between effector memory T cells (Tem) and central memory T cells (Tcm). Cells were stained without fixation (live staining, 30 min RT, Dark). After incubation with the anti-bodies, the sample was centrifuged in 250 µL DPBS (1X) at 1100 rpm for 5 minutes.

This was followed by a wash step with 400 µL DPBS (1X) at 1100 rpm for 5 minutes. Subsequently, the fluorescence signal of the antibody-stained cells was measured using a BD FACSAria III analyzer. Parameters were set for forward scatter (FSC), side scatter (SSC), and fluorescence channels. An unstained control sample was measured to determine the autofluorescence baseline. Live cells were gated from the main population. Finally, fluorescence gating was performed using control samples to differentiate between the positive and negative populations in the corresponding fluorescence channels.

2.2.13.2 Quantification of mouse extracellular cytokines using LEGENDplex™

The extracellular mouse cytokines, including IL-2, 6, 10, TNF-α, and IFN-γ were measured using LEGENDplex™ MU Th1 Panel (5-plex) with V-plate (Figure 8). The principle of LEGENDplex™ is similar to that of a sandwich immunoassay but requires a much smaller sample volume. It is a bead-based immunoassay with beads that are classified differentially according to their size and internal fluorescence intensity. Each set of beads has a unique ID that is aligned with the specific antibody on its surface and acts as a capture bead for the analyzed cytokine.

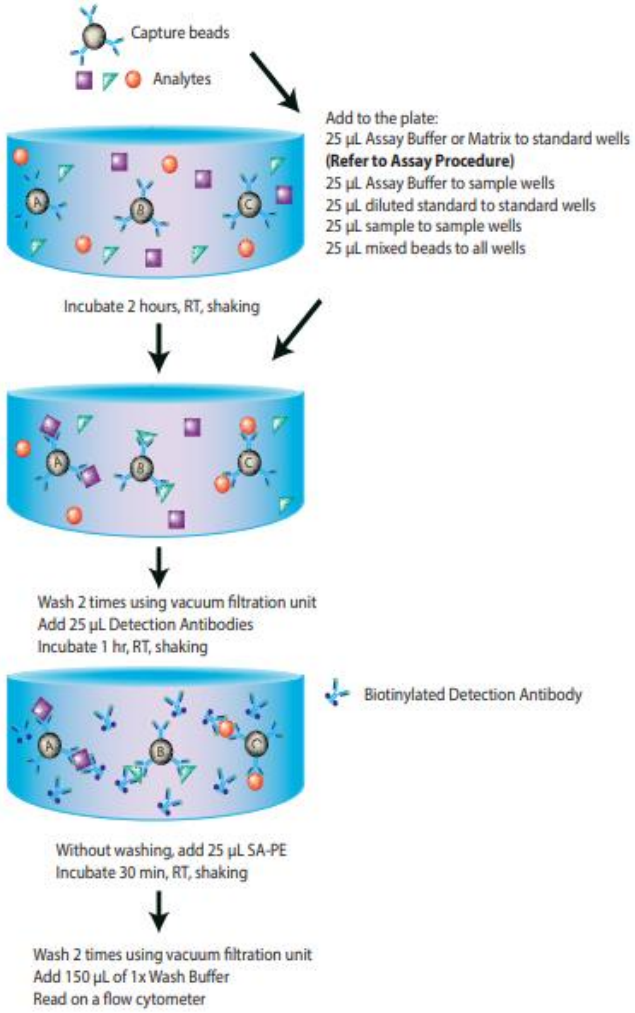

Figure 8: Summary of the protocol for the measurement of supernatant cytokines (IFN-γ, TNF-α, IL-2, IL-6, and IL-10).

Protocol was taken from LEGENDplex™ MU Th1 Panel (5-plex) kit.

The protocol started by mixing the lyophilized mouse Th panel standard cocktail with 250 µL Assay Buffer. After 10 minutes in RT, it was transferred into a polypropylene Eppendorf tube and labeled as C7 (see table 2). Then, the dilution for the individual antibody-immobilized beads (13 X to 1 X) for IL-2, 6, 10, IFN-γ, and TNF-α was performed. According to the manufacturer's protocol for 50 reactions, 1.5 mL of the mixed beads were needed. They were prepared by first sonicating the beads (13X) for 1 minute, taking 115 µL from each of the individual bead type (13X) (total bead volume 575 µL) to a fresh Eppendorf tube and mixed with 925 µL of Assay Buffer to have a final volume of 1.5 mL. The Wash Buffer provided in the kit was diluted from a stock concentration of 20 X to a final concentration of 1 X and stored between 2 -8 ºC until usage. For the sample preparation, the supernatant from the cell culture was diluted 2-fold with Assay Buffer.

The LEGENDplex™ assay was performed at RT in a V-bottom 96 well-plate that was marked into standard and sample wells. Firstly, the standard was diluted in 1:4 serial dilutions in seven 5 mL Eppendorf tubes as displayed in table 2.

Table 2: Preparation of serial dilutions for the standard curve used in LEGENDplex™ MU Th1 Panel (5-plex)

Tube \ Standard ID	Serial dilution	Assay Buffer (µL)	Standard to add
C7	---	---	---
C6	1:4	75	25 µL of C7
C5	1:16	75	25 µL of C6
C4	1:64	75	25 µL of C5
C3	1:256	75	25 µL of C4
C2	1:1024	75	25 µL of C3
C1	1:4096	75	25 µL of C2
C0	---	75	---

The standards were transferred in the 96 well plate in the same order as displayed in table 2, while the supernatant samples were loaded as shown in table 3.

Table 3: Overview of sample loading used in LEGENDplex™ MU Th1 Panel (5-plex)

	Assay Buffer	Standard	Sample
Standard wells	25 µL	25 µL	---
Sample wells	25 µL	25 µL	25 µL

Next, the diluted mixed beads were vortexed for 30 seconds, 25 µL from the mixed beads were added to each well (the final volume of each well was 75 µL). The plate was sealed using a plate sealer and positioned on a plate shaker at 500 rpm for 2 h at RT. Afterward, the plate was centrifuged at a speed of 1.200 × g for 5 minutes, the supernatant was discarded. Then, 200 µL wash buffer was added to each well, centrifuged again with the same settings as before and the supernatant was discarded. Following the second wash step, 25 µL from a biotinylated detection antibody cocktail is added to each well. The various antibodies will bind to their corresponding cytokines which were previously captured on the beads. This resulted in the formation of a capture bead-analyte-detection antibody complexes sandwich. Then, the plate is placed on a plate shaker at 500 rpm for 1 h at RT. Without the washing step, 25 µL of Streptavidin-Phycoerythrin (SA-PE) was added to each well, which bound specifically to the biotinylated detecting antibodies. This step results in fluorescence signals that are proportional to the amount of bound analyte. The plate was sealed using a plate sealer and aluminum foil to provide a dark environment. Then, the plate was placed on a plate shaker at 500 rpm for 30 minutes at RT. Afterward, centrifugation was done at a speed of 1.200 × g for 5 minutes and the supernatant was discarded. 150

µL of the Wash Buffer was added to each well. Next, the beads were resuspended and each of the sample and the standard wells were added into separate Eppendorf tubes. Each of the samples and the standard was run in triplicates to ensure the accuracy of the results. The analyte-specific subsets are isolated using beads distinguished by size and internal fluorescence intensity on a flow cytometer. This allows the quantification of the PE fluorescence signals that were read by BD FACS Aria III. This measurement was done to test the effect of restimulation of GzmB-tdTomato-KI $CD8^+$T cells or CsA on WT $CD8^+$T cells. For measuring extracellular cytokines, the supernatant from day 6 $CD8^+$ T lymphocytes was isolated after 4 h of the restimulation protocol (**Material and Methods section 2.2.3**). For the effect of the CsA on the WT $CD8^+$T, the culture supernatant was collected directly from days 4 and 8 **(Material and Methods section 2.2.4)**.

2.2.14 Transmission Electron Microscopy (TEM)

2.2.14.1 Preparation of cells for high-pressure freezing

Mouse CTLs from days 4 and 8 were collected from cell culture, activator beads were removed, and the cells were centrifuged at 900 rpm for 6 minutes. Cells were resuspended in AIM V medium supplemented with 30% FCS and 10 mM HEPES. 1 µL cell suspension (~4000 cells) was added on PLO (0.1 mg/mL) and anti-CD3ε (30 µg/mL) coated sapphire disks in flat specimen carriers (1.5 mm×0.1 mm). After 5-10 minutes incubation at RT, the samples were vitrified in a high-pressure freezer.

2.2.14.2 Freeze substitution, embedding, and TEM imaging

The flat specimen carriers with the frozen cells were cryo-transferred into the precooled (-130°C) chamber of an automatic freeze substitution device. The temperature was increased from -130 to -90°C over 2 h. Cryo-substitution was performed with 2% osmium tetroxide in anhydrous acetone and 2% water (Liu et al., 2010). The temperature was gradually increased from -90°C to -70°C over 20 h, from -70°C to -50°C over 20 h, and from -50°C to 10°C over 4 h. After washing with acetone, the cells were embedded in Epon-812 resin (30% Epon/acetone for 10 min at -10°C, 70% Epon/acetone for 1 h at -10°C, and pure Epon for 1 h at 20°C; Electron Microscopy Sciences). The temperature was gradually increased from 20 to 60°C over 4 h, and Epon was polymerized at 60°C for 1 d. Next, the carrier and the sapphire disk were removed from the Epon block with liquid nitrogen. The cell monolayer was localized at the surface of the block and could be observed with a light microscope. Ultrathin (70 nm) sections were cut parallel to the cell layer with an ultra-microtome and collected on pioloform-coated copper grids. After staining with 2% uranyl acetate, the sections were analyzed with an electron microscope (Liu et al. 2010). Only well-conserved cells with a visible nucleus and intact plasma membranes were analyzed. The TEM images were captured using Olympus iTEM5.0 image software (build1243). This experiment was done by **Dr. Claudia Schirra**.

2.2.15 Isolation of total RNA and cDNA synthesis

2.2.15.1 Isolation of total Ribonucleic Acid (RNA)

RNA was isolated from 5 million WT $CD8^+$ T lymphocytes collected on days 0, 4, and 8. T cells were collected from the cell culture, and the activator beads were removed. The cells were then centrifuged at 900 rpm for 6 minutes to remove cell debris. 5 million $CD8^+$ T cells were treated with 500 µL of TRIzol to isolate high-quality total RNA, which was then stored at -80°C until RNA analysis. Subsequently, 100 µL of chloroform was added and shaken vigorously for exactly 15 seconds. The mixture was then incubated for 3 minutes at RT to facilitate phase separation and remove contaminating DNA and proteins. Next, it was centrifuged at 11,400 rpm in an Eppendorf centrifuge for 15 minutes at 4°C. Three phases were created: the aqueous phase (upper phase), the interphase, and the chloroform phase (lower phase). Only the aqueous phase was transferred into a fresh tube and treated with 0.25 µL of isopropanol to efficiently precipitate, concentrate, and stabilize RNA molecules. The sample was then incubated for 10 minutes at RT and centrifuged at 11,400 rpm for 10 minutes at 4 °C to precipitate the RNA pellet. Afterward, the supernatant was removed, and the RNA pellet was washed with 1 mL of 75% ethanol (in diethylpyrocarbonate (DEPC)-treated H_2O to kill RNases). The RNA sample was centrifuged for 5 minutes at 8.900 rpm at 4°C. The RNA pellet was briefly dried, and the color of the RNA pellet changed from white to transparent. Finally, it was dissolved in DEPC-treated water.

2.2.15.2 Reverse Transcription-Polymerase Chain Reaction (RT-PCR)

Both deoxynucleotide triphosphates (dNTPs) and random primers containing a mixture of all four nucleotides (A, T, C, G) in random order were added to 1 µg of previously isolated RNA. H_2O was added to a final volume of 12 µL and the mixture was incubated at 65°C for 5 min.

Next, 5X First-Strand Buffer was mixed with dithiothreitol (DTT) and RNaseOUT™ recombinant ribonuclease inhibitor and incubated at 25°C for 2 minutes. To maintain enzyme activity and prevent RNA degradation during cDNA synthesis, SuperScript™ II RT (200 U/µl) was added. The mixture was then incubated at 25°C for 10 minutes, followed by incubation at 42°C for 50 minutes, and finally at 70°C for 15 minutes. The resulting mixture was stored at -20°C until measurement using qPCR CFX96 Bio-Rad.

2.2.15.2.1 Real-Time-Quantitative PCR (RT-qPCR)

RT-qPCR is a powerful technique that tracks the initial input of DNA into a PCR reaction based on the accumulation of fluorescent signals to quantify gene expression levels. The most widely used dye in qPCR is the DNA double-stranded dye SYBR® Green I. ABclonal Genious 2X SYBR Green Fast qPCR Mix (Low ROX Premixed) is an enhanced SYBR Green qPCR mix designed for use in non-ROX mode devices. It includes all components needed for qPCR except primers and templates. It is practical

for experimentation and applicable to multiple species. The above features enable it to be an optimal experimental tool for quantifying genes. The preparation of the reaction systems on ice has been carried out as described in Table 4.

Table 4: Component of the qPCR reaction.

Components	Volume
Genious 2X SYBR Green Fast qPCR Mix (Low ROX Premixed)	5 µl
Forward Primer (10 µM)	0.2 µl
Reverse Primer (10 µM)	0.2 µl
gDNA or cDNA (<50 ng)	1 µl
ddH_2O	to 10 µl

Genious 2X SYBR Green/Green Fast qPCR Mix (low ROX pre-mix) was dissolved at RT and placed on ice. Immediately before use, the mix was thoroughly shaken. After the previous components were added without creating bubbles, it was added to a qPCR plate sealed with an optical membrane. The qPCR reaction was programmed as described in Table 5. To collect all the solution, the qPCR plate was centrifuged at 2500 rpm.

Table 5: qPCR reaction program.

Stage 1	Denaturation	Reps: 1	95 °C	5 min
Stage 2	Cycles	Reps: 45	95 °C	5 seconds
			60 °C	1min
Stage 3	Melt Curve	Reps: 1	default	

This experiment was done by my colleague **Szumin Tu.**

2.2.16 Data Analysis

2.2.16.1 TIRFM data analysis

2.2.16.1.1 Exocytosis analysis

The exocytosis events of both GzmB-pHuji and WGA-Alexa 488 images were analyzed using ImageJ 2.1.0/Java 1.8.0_172 (64-bit). The included secretion events were marked by regions of interest (ROI). A pH-sensitive fluorophore, pHuji, was used to monitor the docking and exocytosis of CGs. Upon the transfer of pHuji from the acidic compartment of the CG to the alkaline extracellular environment, a transient and significant increase in fluorescence intensity is observed due to pH-dependent activation. Two distinct exocytic events were observed. Within the movies, events showed the usual kinetics of a fusion event, with a sudden increase in fluorescence due to pore opening followed by a fast drop down to background level due to the diffusion of GzmB-pHuji. We called these events single core fusions (SCFs). However, the presence of persistent fluorescent spots that remained visible after fusion events indicated the release of insoluble content aggregated into multiple particles, which correspond to SMAPs. These events were called multi-core fusions (MCFs). Data were analyzed automatically with IVEA, an activity recognition program based on artificial intelligence geared towards exocytosis recognition in different cell types (Chouaib et al. 2024). Movies in which several cells were measured simultaneously were cropped down to individual cells before analysis. IVEA automatically detected the fusion events and created a 12-pixel ROI radius centered on the center of mass of each fusion event. In addition, it measured the fluorescent intensity in a 50-frame pre-fusion and 300-frame post-fusion window. The average of fusion events (%) per culture, the number of SC fusion or MC fusion events (SCF or MCF) per movie, and the percentage of SC fusion or MC fusion events per cell were calculated using the following equations.

$$\text{The average fusion events (\%)} = \frac{\sum \text{Percentage of SCF or MCF per culture}}{\text{Total number of cultures}}$$

$$\text{Number of SCF or MCF per Movie} = \frac{\text{Count of SCF or MCF per movie}}{\text{Number of secreting cells per movie}}$$

$$\text{(\%) SCF or MCF per cell} = \frac{\text{Count of SCF or MCF per cell} \times 100}{\text{Total number of fusion events per cell}}$$

2.2.16.2 SIM data analysis

The colocalization analysis was performed using JACop analysis tool in ImageJ on the multi-channel fluorescence images (Bolte and Cordelières 2006). The analyzed coefficients included: Manders' Overlap Coefficient (MOC) (M1 and M2) and Pearson's Correlation Coefficient (PCC). MOC measures the fraction of signal from one channel that overlaps with the signal from another channel (Manders, Verbeek, and Aten 1993). PCC measures the linear correlation between the intensities of the two channels (Bolte and Cordelières 2006). In this analysis, both coefficients were measured using GzmB and TSP-1.

We measured the spatial heterogeneity of the TSP-1-GFPSpark signal in the SIM images using the coefficient of variation (CV) analysis (Luccardini et al. 2009). It was performed using an automated macro on background-subtracted images created by **Abed Chouaib**. The CV was calculated with the following equation:

$$CV = \frac{\text{Standard Deviation of the pixel intensity}}{\text{Mean fluorescence intensity of all pixels}} \times 100$$

The CV analysis was performed on the entire stack and limited to the cell cytoplasm.

2.2.16.3 Flow cytometry data analysis

2.2.16.3.1 Quantification of different T cell subsets

Using FlowJo v10.0.7 software, the percentage of each population was determined from the manually gated live cell population. The differences between these populations were based on varying expression levels of surface markers measured using a BD FACSAria III analyzer. Respectively, $CD44^{hi}$, and $CD62L^{lo}$ expression characterized the effector memory T cells, while $CD44^{hi}$, and $CD62L^{hi}$ expression marked the central memory T cells

2.2.16.3.2 Cytokines quantification

The acquired data were uploaded to the online LEGENDplex™ Data Analysis Software Version 8.0. The control and replicates measured sample files were uploaded in order. Manual gating was applied to isolate analyte-specific subsets. These were identified using beads differentiated by size and internal fluorescence intensity, acquired through a flow cytometer. Finally, a standard curve derived from the assay was utilized to determine the concentration of specifically measured cytokines in pg/mL (**Annex**).

2.2.16.4 Analysis of TEM data

The number of SCGs and MCGs per cell and SMAPs per MCG were analyzed manually. SCGs were recognized by smaller granular-sized homogeneous structures. In contrast, MCGs were heterogeneous in morphology and consisted of multiple rounded structures (Chang et al. 2022). The region of interest (ROI) was manually generated to document the outline of the plasma membrane, nucleus, and cytotoxic granules. The ROIs surrounding the CGs and SMAPs were manually delineated, and the respective areas were subsequently calculated using the ImageJ plugin. Next, the diameter of SMAPs was evaluated using the Feret's diameter (Haasters et al. 2009). Feret's diameter is the measured distance between two parallel tangents on opposite sides of the object. It is used to determine the size of irregularly shaped objects in image analysis (Zanier et al. 2015).

2.2.16.5 RT-qPCR data analysis

Quantification cycle (Cq) values are used to quantify the amount of target nucleic acid (DNA or RNA) present in a qPCR reaction. The average of the Cq value was done to both the cDNA of target genes (IFN-γ and TSP-1) and the TATA-binding protein (TBP), which is a transcription factor involved in the regulation of gene expression and has been applied as a reference gene or internal control. We used day 0 naïve $CD8^+$T cells as the control group and $CD8^+$ T cells from days 4 and 8 as the sample group. The threshold cycle (CT) is the cycle at which the fluorescence level approaches a certain amount (the threshold). The data is being analyzed by Bio-Rad EFX Manager 3.0. Concerning the ΔΔCT of the 2-ΔΔCT method, the first ΔCT is the difference in the threshold cycle between the reference genes and target genes: ΔCT = CT (a target gene) − CT (TBP). This value is used to measure the relative expression level of the target gene normalized to the reference gene (TBP) within a single sample. The ΔΔCT is the difference in ΔCT as explained in the above formula between the target and control group, which is ΔΔCT = ΔCT (target sample) −ΔCT (control group). This yields a change in the expression of the target gene relative to the control group. To convert ΔΔCT values into fold differences, representing how many times the target gene's expression has changed relative to the control group. We used the following formula: Fold Change = 2^(-ΔΔCT) (Schmittgen et al. 2000).

3. Results

3.1 Varying concentrations of anti-CD3ε did not affect the CTL fusion profile

Anti-CD3ε-stimulated T cells trigger intracellular signaling leading to the release of cytotoxic granules (CGs). Jenkins et al (2009) have shown that an increased concentration of target antigen enhances the cytotoxicity of Cytotoxic-T-Lymphocyte (CTL). In a related study, different concentrations of anti-CD3ε (5, 10, and 20 µg/mL) were tested on supported lipid bilayer (SLB) with day 7-8 CTLs to examine immune synapse (IS) formation and cytotoxicity (Estl et al. 2020). They found that 10 µg/mL anti-CD3ε produced the shortest CTL adhesion latency and the highest CG fusion. To further investigate how anti-CD3ε strength affects the release of two CG classes, CTLs from wild-type (WT) mice were collected on days 4, 5, 6, and 7. These CTLs were electroporated with GzmB-pHuji and then placed on an SLB in the following days (days 5, 6, 7, 8) with constant intercellular adhesion molecule-1 (ICAM-1) levels to facilitate CTL adhesion via lymphocyte function-associated antigen-1 (LFA-1). Different anti-CD3ε concentrations (5, 10, and 20 µg/mL) were used to induce the secretion of CG. Both cytotoxic granules: single core granules (SCGs) and multicore granules (MCGs) were labeled through GzmB-pHuji overexpression. Using pHuji, a pH-sensitive fluorescent protein, facilitated the ability to detect exocytosis with total internal reflection fluorescence microscopy (TIRFM) and to follow the release dynamic and the dispersion of granule content in real-time (Figure 9). CG fusion is characterized by a sharp increase in fluorescence intensity. pHuji is quenched in the acidic lumen of the CG (pKa = 7.7) and becomes unquenched when the fusion pore opens, leading to granule lumen neutralization (Shen et al. 2014)

The experiment began with the seeding of GzmB-pHuji electroporated CTLs onto the SLB in a low calcium extracellular solution. After 2-3 minutes, when the CTLs had settled, TIRFM imaging was initiated (**Materials and Methods 2.2.11.1**).

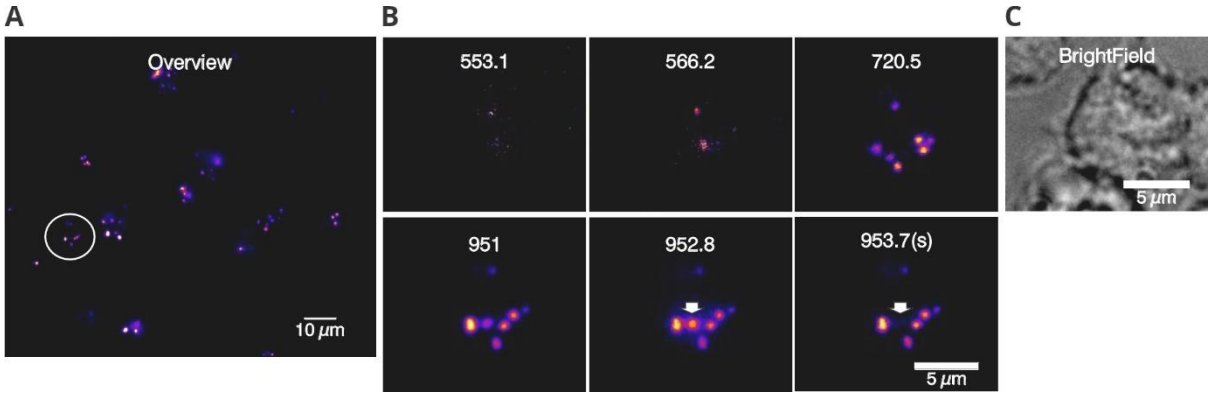

Figure 9: Various stages before and after CG release on SLB.

(A) Displayed a TIRFM overview snapshot of day 7 WT CTLs overexpressing GzmB-pHuji on an SLB with 10 µg/mL anti-CD3ε. (B) Enlarged time-lapse snapshots of a single core fusion event (solid white arrows) from the CTL highlighted by the white circle in (A). (C) The bright-field image of the corresponding cell is shown on the far right.

IS formation was identified by the time of appearance of the CGs in the TIRFM field of view. Subsequently, the fusion of CG was observed. SC fusion event was characterized by a fast decrease in fluorescence intensity accompanied by a fluorescence cloud corresponding to the diffusion of the CG content in the IS (Figure 9). MC fusion event also displayed a fluorescent cloud but after its dispersion, multiple GzmB-pHuji-labeled particles known as supramolecular attack particles (SMAPs) remained on the SLB. These were very stable as they have been described to last for several hours without substantial loss of fluorescence intensity (Bálint et al. 2020).

More than 20 transfected cells were measured per anti-CD3ε concentrations (Figure 10A). The different anti-CD3ε concentrations slightly impacted IS formation. CTLs took almost 60 seconds to form an IS on 20 µg/mL of anti-CD3ε, while at concentrations of 5 and 10 µg/mL, they took an average of 80 seconds (Figure 10B). The concentration of 10 µg/mL anti-CD3ε resulted in approximately 17% more secreting cells on average compared to the number of secreting cells observed at 5 µg/mL and 20 µg/mL of anti-CD3ε, which were around 7 and 13 secreting CTLs, respectively (Figure 10C).

The effect of different T cell receptors (TCR) stimuli on the CG fusion type was evaluated by identifying the percentage of SC and MC fusion events **(Materials and Methods section 2.2.16.1.1).** CTLs stimulated with 10 µg/mL anti-CD3ε exhibited the highest proportion of SC fusion events, approximately 80%. In comparison, the percentage of SC fusions observed with 5 µg/mL and 20 µg/mL anti-CD3ε were around 60% and 70%, respectively (Figure 10D). 5 µg/mL anti-CD3ε induced the highest percentage of MC fusion events of about 40 % higher than 10 µg/mL and 20 µg/mL which was around 20 % (Figure 10D). However, these differences were not statistically significant.

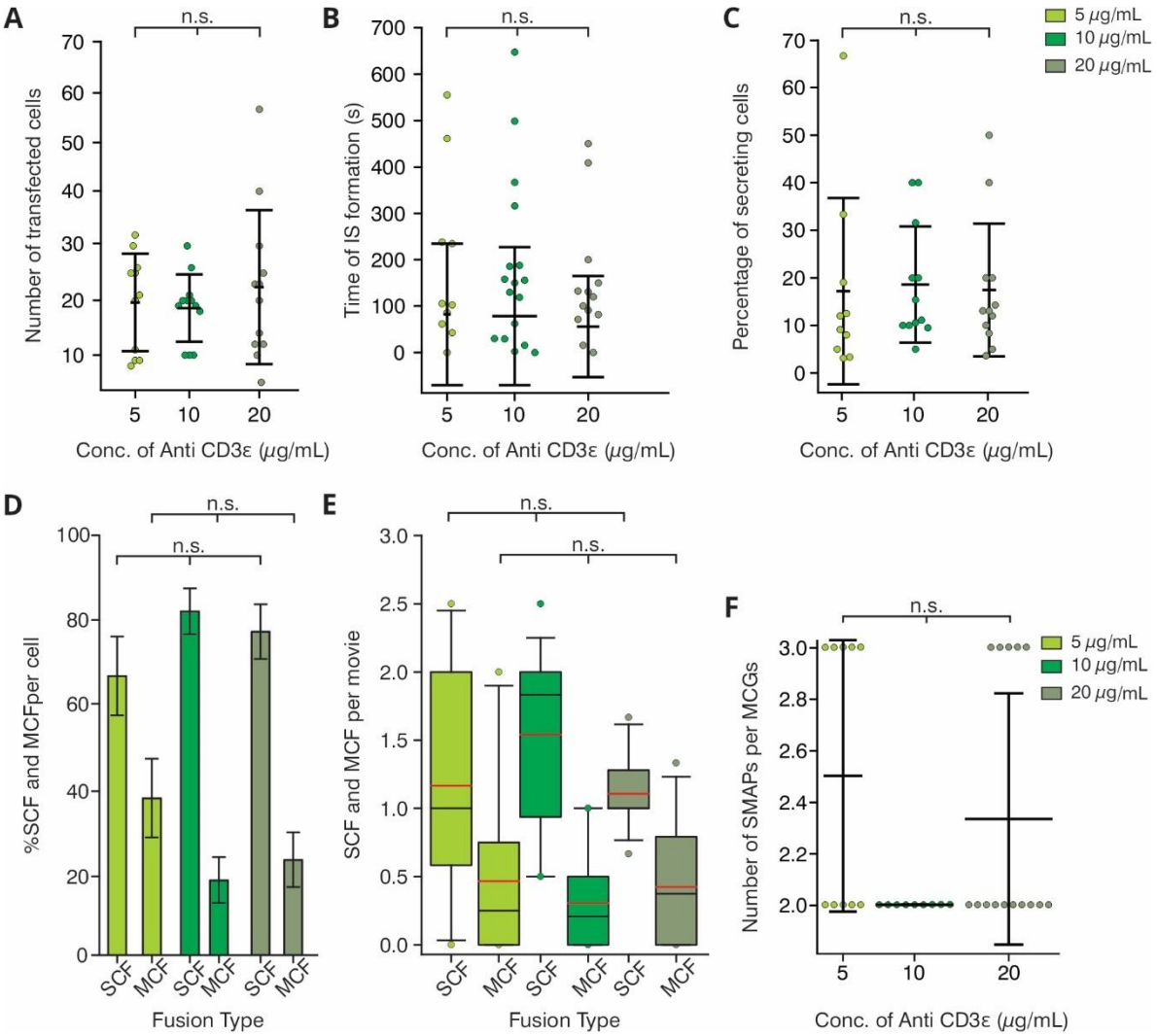

Figure 10: The strength of TCR stimulation did not modulate the fusion type of CG in CTLs.

Analysis of TIRFM imaging conducted on GzmB-pHuji transfected CTLs and seeded on SLB with 5, 10, and 20 µg/mL anti-CD3ε. The Measurements were performed on CTLs at days 5, 6, 7, and 8. (A-D) Scatter dot plots show (A) Number of transfected cells. (B) Duration of IS formation and (C) Percentage of secreting cells. (D) Bar graph displaying the percentage of SC and MC fusion events per cell. (E) Box plot presenting the number of SC and MC fusion events per movie. (F) A scatter dot plot shows the number of secreted SMAPs per MCGs. In the box plot, the center red line represents the mean, and the black line indicates the median. The box boundaries show the interquartile range (25th to 75th percentiles), with outliers displayed as individual points beyond the whiskers, which represent the 5th and 95th percentiles. In all scatter dot plots, the horizontal black line represents the mean and error bars represent the standard deviation (SD). In the bar graph, show the average value with the standard error of the mean (SEM) as error bars. Statistical analyses were performed using Kruskal-Wallis test. N_{mouse} =5, n_{cells} of 5 µg/mL (23), 10 µg/mL (36), and 20 µg/mL (35). Statistical significance is indicated as follows: n.s. (not significant)

The number of SC and MC fusion events per individual cell was measured to assess whether our observations were influenced by cell-to-cell variability **(Materials and Methods section 2.2.16.1.1).**

The results showed significant cell-to-cell variability, which was consistent across all three conditions (Figure 10E). This indicates that TCR stimulus did not affect the fusion type of CGs. Further examination showed that MC fusion events generated around 2–3 SMAPs, irrespective of the anti-CD3ε concentration. (Figure 10F).

In summary, CTL stimulation with 10 µg/mL anti-CD3ε was identified as the optimal concentration to increase the number of secreting cells. Further analysis revealed that changes in the fusion profile of CGs might be influenced more by the duration of culture than by the strength of T cell receptor (TCR) stimulation (Table 6). To explore this further, we examined how earlier and later culture days affected the ability of CTLs to exhibit SC and MC fusion events when stimulated with 10 µg/mL anti-CD3ε.

Table 6: The day of culture has a noticeable impact on the fusion profile of CG

Condition	Day of Culture	Number of SC fusion event	Number of MC fusion event
Anti-CD3ε 5 µg/mL	5	15	4
	7	5	1
	8	7	3
Anti-CD3ε 10 µg/mL	5	16	1
	6	8	1
	7	3	1
	8	10	4
Anti-CD3ε 20 µg/mL	5	28	5
	6	4	4
	7	3	2
	8	4	5

3.2 Prolonged culture time promoted MCGs secretion

TIRFM was used to track fusion events on different days in culture (Figure 11). WT CTLs overexpressing GzmB-pHuji were labeled on various days in culture (days 3, 5, 7, and 9) and seeded on the following days (days 4, 6, 8, and 10) on an SLB with 10 µg/mL anti-CD3ε for TIRFM imaging.

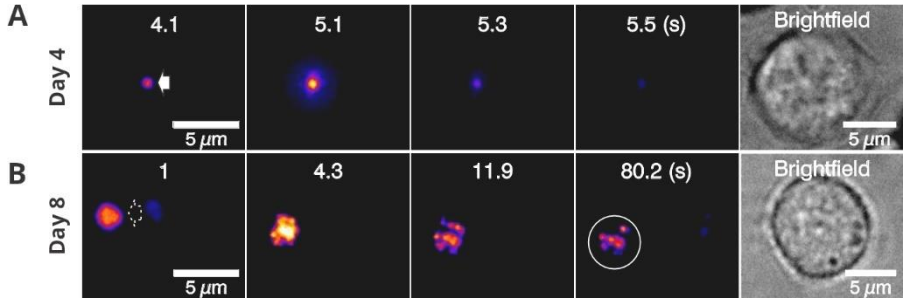

Figure 11: Fusion of the two classes of GzmB-labeled granules at the immune synapse.

Representative TIRFM snapshots of WT CTLs on days 4 and 8, transfected with GzmB-pHuji and seeded on SLB with 10 µg/mL anti-CD3ε. These snapshots show: (A) Single-core granule that underwent a rapid fusion event with a cloud of diffusible GzmB-pHuji that lasted approximately 0.4 seconds (solid white arrow), and (B) Multi-core granule that fused to form a small cloud of diffusible GzmB-pHuji with several released SMAPs (>2) (white circle)that remained attached to the SLB throughout the recording (dotted white arrow). The corresponding bright-field images are shown on the far left.

The analysis of the TIRFM movies revealed that increasing time in culture changed the overall behavior of CTLs. CTLs cultured for a longer duration (days 8 and 10) showed faster IS formation (approximately 90 seconds) and the number of secreting cells was higher. In contrast, at earlier time points (days 4 and 6) IS formation was slower (around 160 and 200 seconds, respectively) and the number of secreting cells was reduced (Figure 12A and B). To determine if the maturation in culture affects the class of CG, the percentage of average fusion events was calculated per culture. The data indicated that SC fusion events were dominant in the earlier days of culture (Figure 12C). As the culture progressed, MC fusion events increased to around 60 % on later days (Figure 12C). Even though the mean fusion events indicated a shift from SC to MC fusion events, it remains uncertain whether this reflects a true shift in biological processes or merely results from cell-to-cell variability. To address this, the percentage of SC and MC fusion events per cell was calculated **(Material and Methods section 2.2.16.1.1)**. The analysis confirmed a transition between SC fusion events at early times towards MC fusion events at later times in culture. To understand whether the observed shift in fusion type was due to a net decrease of SC fusion events in favor of MC fusion events, we calculated the number of the SC and MC fusion events in individual recordings. We found that CTLs showed a consistent number of SC fusion events over time in culture (1–2), while MC fusion events increased from 0 on day 4 to ~1 event per cell on days 8 and 10 (Figure 12E). Additionally, the number of SMAPs released remained relatively consistent (Figure 12F). In summary, these data confirmed the finding shown in Table 6 that CTLs exhibited more MC fusion events over time in culture.

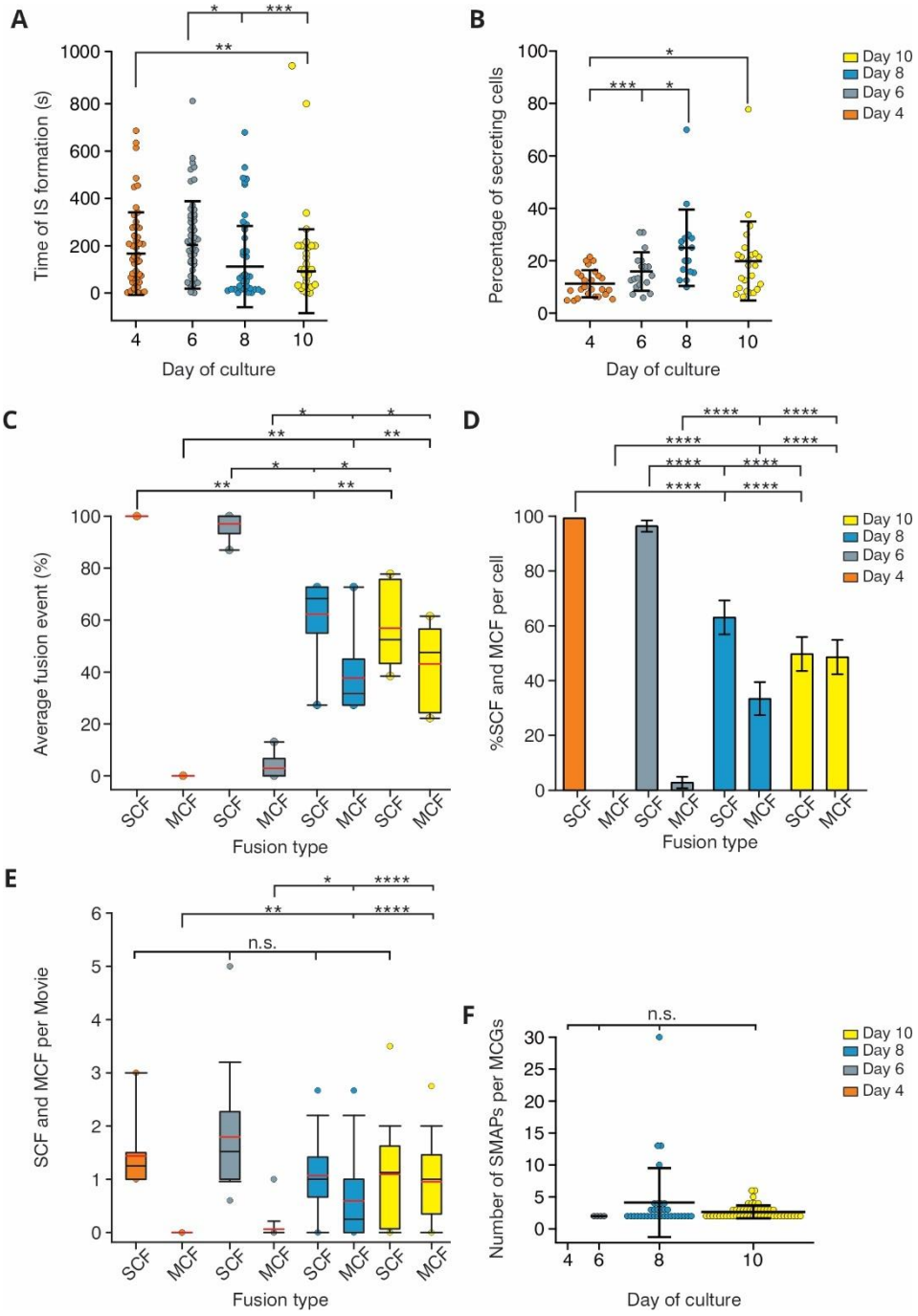

Figure 12: Cell maturation shifted the fusion profile in CTLs from SC to MC fusion events.

Analysis of the TIRFM data acquired from GzmB-pHuji transfected CTLs that were seeded on SLB containing 10 µg/mL anti-CD3ε on culture days 4, 6, 8, and 10. (A-B) Scatter dot plots display (A) Duration CTLs took to form IS, and (B) Percentage of secreting cells. (C) Box plot showing the percentage of the average fusion events per culture. (D) The average percentage of SC and MC fusion events per cell is presented as a bar graph. (E) Box plot displaying the number of SC and MC fusion events per movie. (F) Number of released SMAPs per MCGs is shown as a scatter dot plot. In the box plot, the center red line represents the mean, and the black line indicates the median. The box boundaries show the interquartile range (25th to 75th percentiles), with outliers displayed as individual points beyond the whiskers, which represent the 5th and 95th percentiles. In all scatter dot plots, the horizontal black line represents the mean and error bars represent the SD. The bar graphs display the average with SEM as error bars. Statistical analyses were performed using Kruskal-Wallis post-test. N_{mouse}= 6, n_{cells}=55. Statistical significance is indicated as follows: n.s. (not significant, p>0.05), *$p < 0.05$, **$p < 0.01$, ***$p < 0.001$.

3.3 CTL maturation did not influence T cell subtypes

Flow cytometry was used to identify T cell subtypes using CD62L and CD44 as a marker to differentiate between naïve CTL, central memory T cell (Tcm), and effector memory T cell (Tem) (Figure 13A). The statistical analysis revealed a slight, though non-significant, decrease in the percentage of naïve and central memory T cells (Figure 13Bi, ii). In contrast, a non-significant increase was observed in the Tem (Figure 13Biii). However, these minor changes are unlikely to account for the effect of cell maturation on the increased release of MCGs.

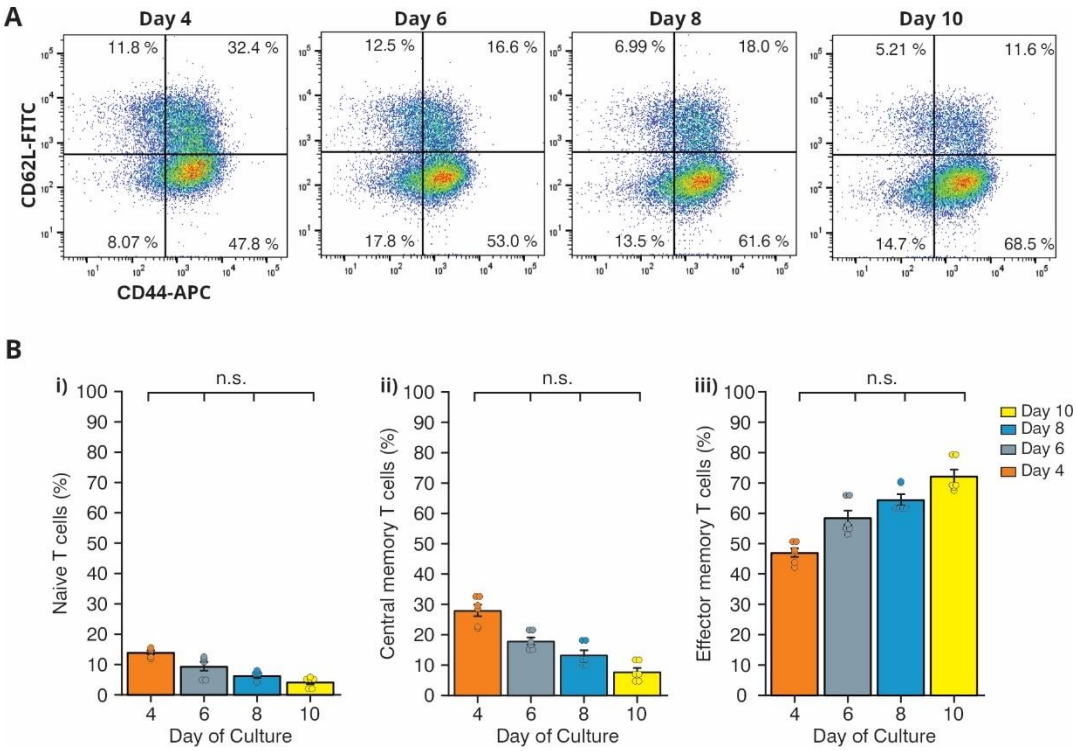

Figure 13: Duration in culture did not alter the subtypes of CTLs.

(A) Flow cytometry plots of WT-CTLs on days 4, 6, 8, and 10 using FlowJo software. (B) Statistical analyses of the effect of time in culture on $CD8^+$ T cell subtypes. The average percent of (i) naïve T cells, (ii) central memory, and (iii) effector memory T cells are shown. Error bars are SEM. Statistical analyses were performed with Kruskal-Wallis test. N_{mouse}= 3. Statistical significance is indicated as follows: n.s. (not significant).

3.4 Wheat germ agglutinin (WGA) as a marker for identifying possible intermediate form of CGs

To corroborate the prior findings in Figure 12, we aimed to mark the MG fusion events to determine the effect of cellular maturation on CTL fusion events. To this end, we employed WT CTLs overexpressing GzmB-pHuji and included WGA as a marker for MCGs. WGA selectively binds to glycoproteins in the shell surrounding SMAPs within MCGs (Bálint et al. 2020; Rettig and Baldari 2020).

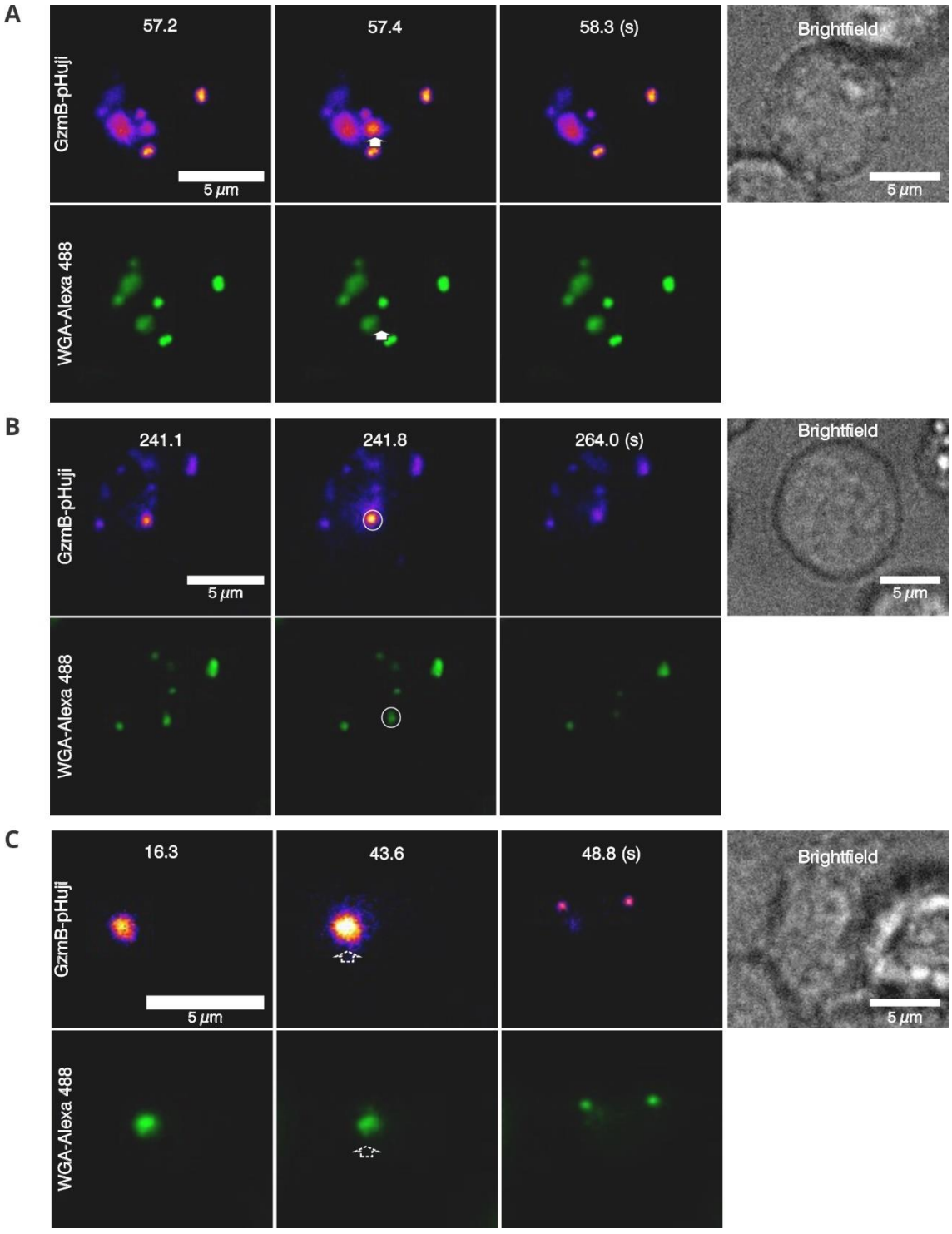

Figure 14: WGA and GzmB-pHuji Labeling identified a possible intermediate form of CG.

Presentation of TIRFM data conducted on day 6 WT CTLs overexpressing GzmB-pHuji, stained with WGA-Alexa 488, and seeded on SLB with 10 µg/mL anti-CD3ε. TIRFM snapshots showing different granule fusion events: (A) Single core granule, labeled as $GzmB^+$ WGA^-, which underwent a rapid fusion event, releasing diffusible GzmB-pHuji (solid white arrow); (B) Potential intermediate form of CG labeled as $GzmB^+$ WGA^+ (hollow white circle), exhibiting fusion kinetics similar to (A). (C) Multi-core granule labeled as $GzmB^+$ WGA^+ (dotted white arrow) that exhibited a fusion event, forming a cloud of diffusible GzmB-pHuji and two released SMAPs, which remained attached to the SLB throughout the recording. Bright-field images of the corresponding cells are shown on the far right.

The SCG and MCG fusion events were identified via the GzmB-pHuji channel. SCG fusion events were designated as $GzmB^+$ WGA^-, and MCG fusion events with released SMAPs were identified as $GzmB^+$ WGA^+ (Figure 14A and C). The statistical analysis of CTL functionality, including the time of IS formation, yielded results consistent with the previous experiment (Figure 12A). These results demonstrated that using WGA as a marker for MCGs had no discernible impact on CTL behavior in culture (Figure 15A). To corroborate our initial observation regarding the transition from SCG to MCG fusion events, we conducted a detailed analysis. This analysis aimed to ascertain the average number of fusion events and the extent of cell-to-cell variability. Additionally, we examined the number of CG fusion events and the number of released SMAPs from the MCGs. The results confirmed that T- cell maturation facilitated the release of MCG fusion events over time in culture (Figure 15C, D, E, and G). More interestingly, contrary to our expectations that all SC fusion events would be $GzmB^+$ WGA^-, we found that a subset of SC fusion events were $GzmB^+$ WGA^+ (Figure 14B). These double-labeled CGs, which exhibited fusion kinetics analogous to SCGs, were postulated to represent an intermediate form between SCGs and MCGs. The distribution of this intermediate form exhibited alterations over time in culture. On day 4, this intermediate form constituted nearly half of the total SC fusion events (47% ± 12.9, $p = 0.747$, $n_{cells} = 32$ cells). As MC fusion events increased, the occurrence of this intermediate form declined to 25% ± 14.5 on day 6, followed by a slight rise to 31.2% ± 23.7 on day 8 ($p = 0.577$, $n_{cells} = 36\text{-}33$). By day 10, the proportion of that intermediate form had decreased further, to 4.5% ± 4.5 ($p = 0.333$, $n_{cells} = 32$). This data indicated an inverse relationship between the percentage of the intermediate form and the emergence of MCGs over time. This suggests that these intermediate granules may represent a maturation step for MCGs. However, an alternative hypothesis is that they represent an independent class of CGs with rapid release and more cytotoxic content. In conclusion, the WGA labeling demonstrated a definitive correlation between culture duration and the increased release of MC fusion events with the discovery of possible intermediate granules.

Our findings suggest that the peak of SC fusion events occurred on day 4, while the peak of MC fusion events occurred on days 8 and 10, with a greater number of secreting CTLs observed on day 8. Consequently, we used only day 4 and day 8 CTLs for further investigation to gain deeper insights into intracellular CG dynamics.

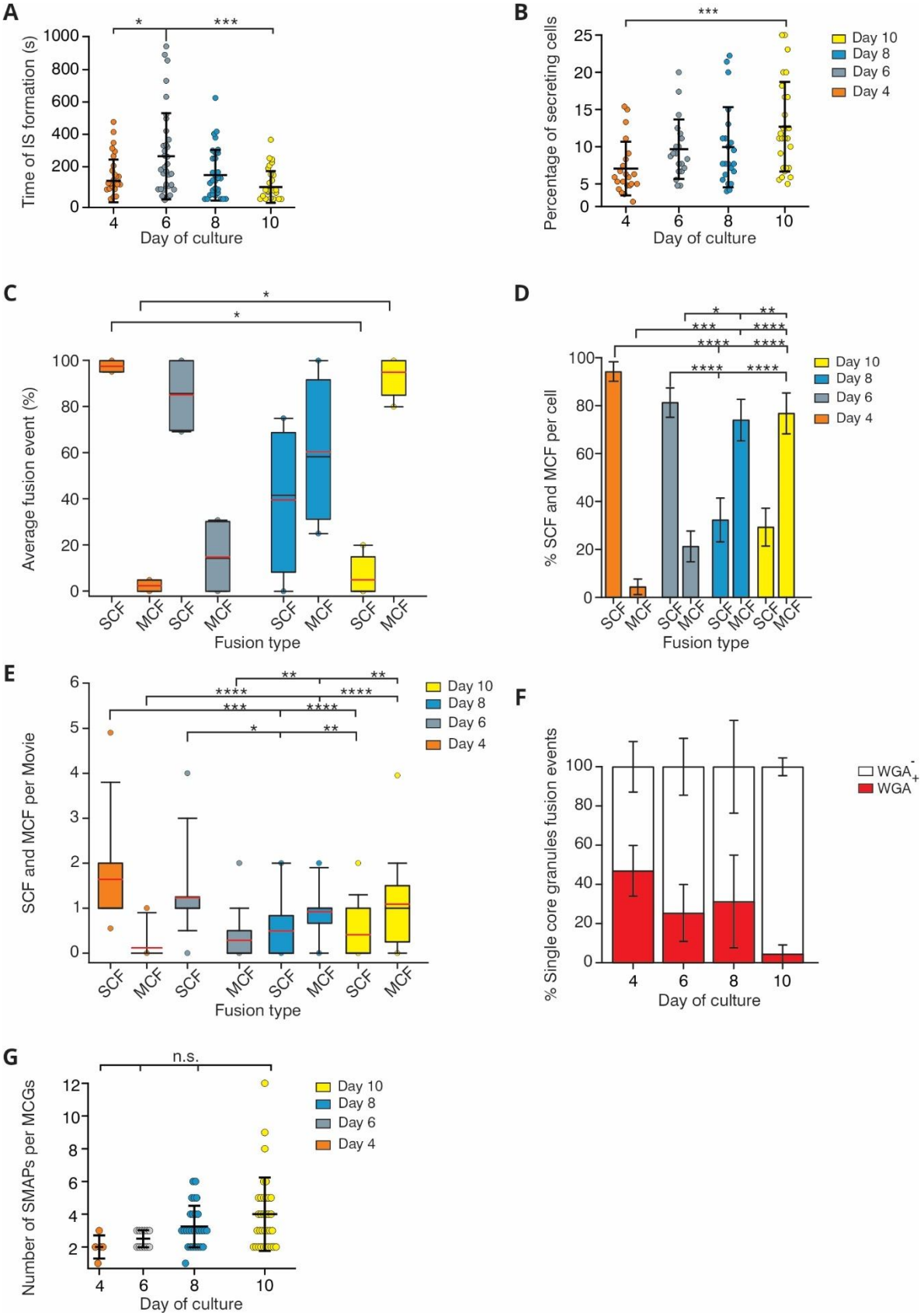

Figure 15: WGA confirmed the effect of T-cell maturation and revealed potential intermediate CG form.

Analysis of TIRFM data conducted on WT CTLs overexpressing GzmB-pHuji, stained with WGA-Alexa 488, and seeded on SLB on days 4, 6, 8, and 10 is illustrated. (A-B) Scatter dot plots display (A) Duration CTLs took to form IS and (B) The percentage of secreting cells. (C) A box plot shows the percentage of the average fusion

events per culture. (D) The average percentage of SC and MC fusion events per cell is presented as a bar graph. (E) A box plot displays the number of SC and MC fusion events per movie. (F) The percentage of the SC fusion events (WGA^+ (Red)\ WGA^- (White)) is shown as a bar graph. (G) Number of the released SMAPs per MCGs is shown as a scatter dot plot. In the box plot, the center red line is the mean and the black line is the median of the data. The box's boundaries represent the interquartile range (25th to 75th percentiles), with outliers shown as individual points beyond the whiskers, while the whiskers are the 10th/90th percentiles. The colored circles represent the 5th and 95th percentiles outliers. In all scatter dot plots, the horizontal black line represents the mean, and error bars represent the SD. In all bar graphs, error bars are the SEM. Statistical analyses were performed using Dunn's multiple comparison test, Kruskal-Wallis test, and Mann-Whitney Rank Sum Test. N_{mouse}= 5-6, n_{cells}= day 4 (32 cells), n_{cells}= day 6 (36 cells), n_{cells}= day 8 (33 cells), and n_{cells}= day 10 (32 cells). Statistical significance is indicated as follows: n.s. (not significant), $*p < 0.05$, $**p < 0.01$, and $***p < 0.001$.

3.5 Thrombospondin-1 (TSP-1) shifted from diffuse localization to CGs over time in culture

The previous results raised two key questions: first, whether the observed increase in MC fusion events over time in culture is driven by the relocalization or trafficking of MCGs to the IS; and second, whether this increase is due to enhanced MCG biogenesis.

To answer the first question, GzmB-tdTomato KI CTLs were transfected with TSP-1-GFPSpark as a SMAP marker within the MCG. Overexpression was preferred to immunostaining as there is no good mouse anti-TSP-1. After 14-18 h of the transfection, the CTLs were washed and settled down on coverslips under two separate conditions: first, on Poly-L-ornithine (PLO) as a non-activated control (resting CTLs), and second, on anti-CD3ε, which induced the formation of an IS (stimulated CTLs). After fixing the CTLs, they were imaged with SIM. In the resulting images, CGs were identified by the spotty endogenous GzmB-tdTomato signal shown in yellow, whereas TSP-1-GFPSpark is shown in cyan (Figure 16A). The co-localization between GzmB-tdTomato and TSP-1-GFPSpark appears in green in the merged channels (Figure 16A). Overall, the TSP-1-GFPSpark signal appeared to be different between days 4 and 8. On day 4, a diffuse dispersion of the TSP-1-GFPSpark was observed, with minimal colocalization with GzmB-tdTomato. By day 8, the distribution of TSP-1-GFPSpark had become more punctate, and the puncta colocalized with the GzmB-tdTomato-labeled CGs. The coefficient of variation (CV) of the TSP-1-GFPSpark signal was measured to quantify the degree of protein clustering.

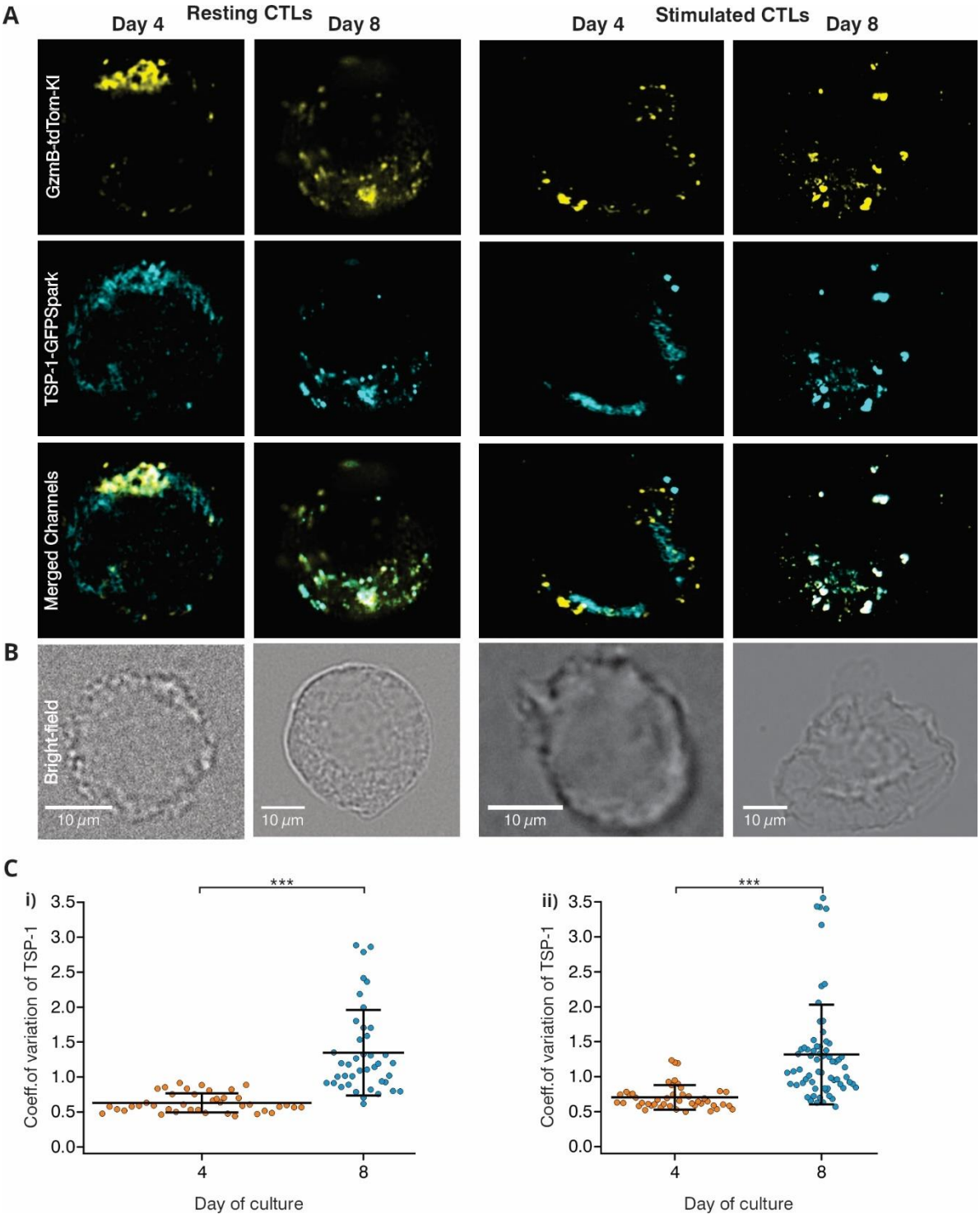

Figure 16: TSP-1 relocalized to CGs over time in culture

(A) Exemplary SIM images showing resting and stimulated days 4 and 8 CTLs, Labeled with the endogenous GzmB-tdTomato fluorescent (yellow) and overexpressing the MCGs marker, TSP-1-GFPSpark (cyan) and the merged channels. (B) Brightfield images. (C) Scatter dot plots display the coefficient of variation of the TSP-1 signal from days 4 and 8 CTLs comparing them in resting (i) and stimulated (ii) conditions. In all scatter dot plots, the horizontal black line represents the mean, and the error bars represent the SD. Statistical analyses were performed using the Mann-Whitney Rank Sum Test. N_{mouse}= 4, n_{cells} in the resting group (32-33), and n_{cells} in the activated group (39-41). Statistical significance is indicated as follows: ***p < 0.001.

The summary of the CV analysis is shown in Figure 16C. The CV of TSP-1-GFPSpark was significantly smaller on day 4 than on day 8. In fact, it was 1.8 times larger on day 8 than on day 4 irrespective of the activation state of the cells (i.e. whether they were seeded on antiCD3ε or not). The elevated CV on day 8 was attributable to the increased variability in the TSP-1 signal, which corresponds to an increase in punctate structures and a decrease in the dispersed cytoplasmic signal. Conversely, the decreased CV on day 4 (Figure 16C) indicated a more consistent and uniform distribution of the TSP-1 signal, with a reduction in the punctate structures.

To assess whether the punctate structures of TSP-1-GFPSpark were localized to the CGs over time in culture, we performed a co-localization analysis using Manders' overlap coefficient (MOC). The co- localization was measured in two different areas in both resting and stimulated CTLs. The first area is called the contact area (PLO) or the IS area (anti-CD3ε). It was identified as the area that would be imaged by TIRFM, corresponding to approximately 1 µm, i.e. 5 slices, above the coverslip. In the resting CTLs (Figure 17A), MOC revealed a significant increase in the degree of overlap of the GzmB-tdTomato with the TSP-1-GFPSpark signals on day 8 compared to day 4. Specifically, in resting CTLs, the contact zone values increased from 0.28 ± 0.05 on day 4 to 0.57 ± 0.04 on day 8 ($p < 0.001$, n_{cells}= 32-33), while the apical area values increased from 0.25 ± 0.04 on day 4 to 0.55 ± 0.04 on day 8 ($p < 0.001$, n_{cells}= 32-33) (Figure 17A). Similarly, in stimulated CTLs, the values at IS rose from 0.36 ± 0.03 on day 4 to 0.48 ± 0.03 on day 8 ($p = 0.007$, n_{cells}= 39-41), and in the area above the IS, values increased from 0.39 ± 0.03 on day 4 to 0.48 ± 0.03 on day 8 ($p = 0.037$, n_{cells}= 39-41) (Figure 17B). When analyzing the overlap of TSP-1-GFPSpark with GzmB-tdTomato, a similar trend was observed. In resting CTLs, the contact zone values increased from 0.41 ± 0.05 on day 4 to 0.75 ± 0.04 on day 8 ($p <0.001$, n_{cells}= 32-33), and the apical area values rose from 0.46 ± 0.05 on day 4 to 0.76 ± 0.03 on day 8 ($p < 0.001$, n_{cells}= 32-33) (Figure 17A). In stimulated CTLs, values at the IS increased from 0.50 ± 0.04 on day 4 to 0.72 ± 0.03 on day 8 ($p < 0.00$, n_{cells}= 39-41), while in the area above the IS, values were 0.64 ± 0.04 on day 4 and 0.72 ± 0.03 on day 8 ($p = 0.207$, n_{cells}= 39-41) (Figure 17B). Pearson's correlation coefficient (PCC) was also calculated to validate the MOC results. In resting CTLs, PCC confirmed the stronger correlation between GzmB-tdTomato and TSP-1-GFPSpark signals on day 8 compared to day 4. Specifically, at the contact zone, PCC values increased from 0.52 ± 0.03 on day 4 to 0.55 ± 0.04 on day 8 ($p < 0.001$, n_{cells}= 32-33), while at the apical area, values rose from 0.54 ± 0.02 on day 4 to 0.76 ± 0.04 on day 8 ($p < 0.001$, n_{cells}= 32-33) (Figure 17C).

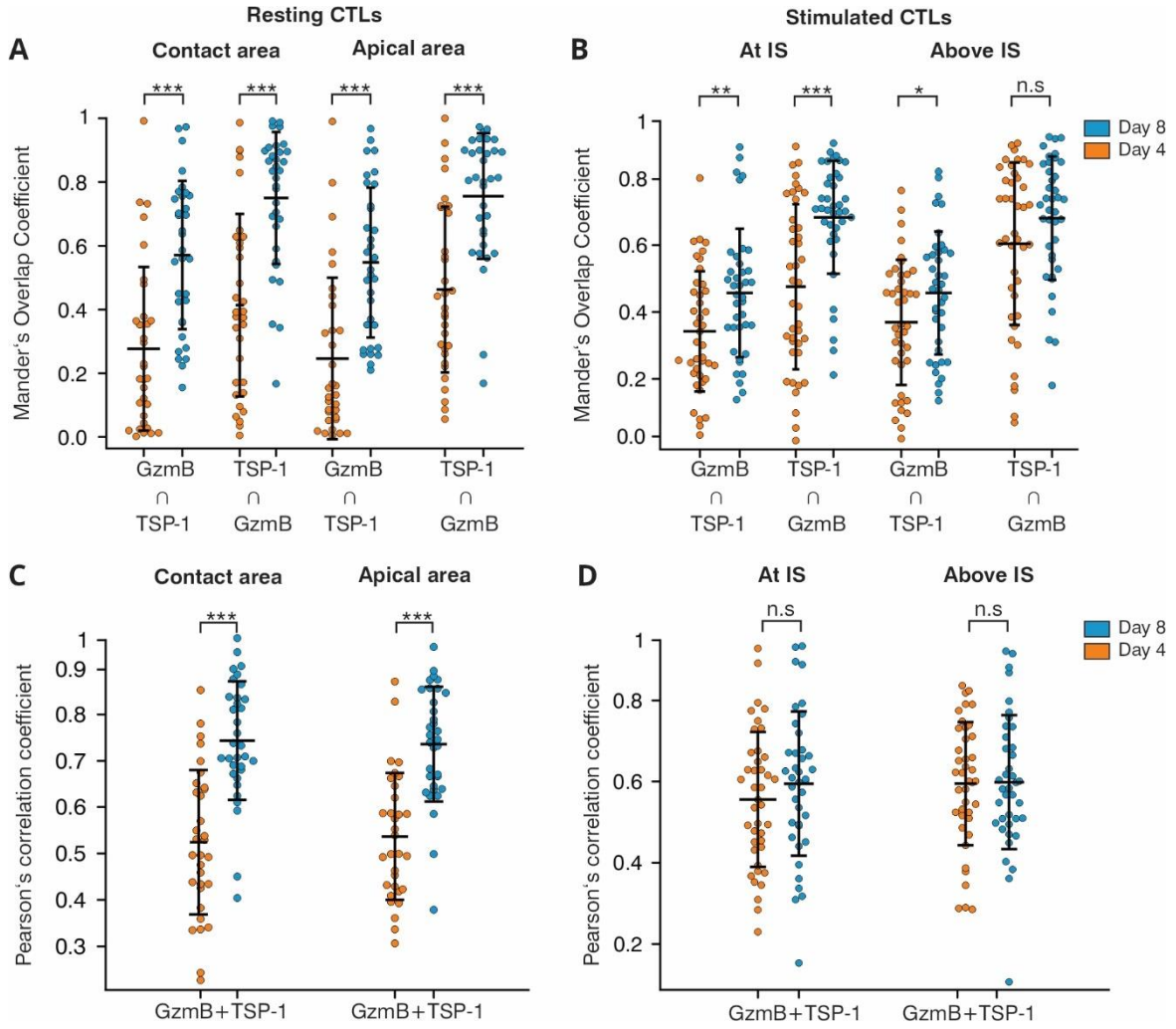

Figure 17: The co-localization between GzmB and TSP-1 channels over time was not affected by TCR stimulation.

(A-B) Scatter dot plots displaying the degree of the overlap between GzmB-tdTomato and TSP-1-GFPSpark signals quantified with the Mander's coefficient in (A) Resting and (B) Activated CTLs. (C-D) Scatter dot plots of the linear correlation between the pixel intensities of these signals evaluated by the Pearson's correlation coefficient of both (C) Resting and (D) Activated CTLs. For resting CTLs all these coefficients were assessed in the cell's contact zone with the coverslip and in their apical areas. For activated CTLs, the coefficients were measured at the immunological synapse (IS) and above IS areas. The horizontal black line in the scatter dot plots represents the mean and the error bars represent the SDs. Statistical analysis was performed using Student's t-test and Mann-Whitney Rank Sum Test. N_{mouse}= 4, n_{cells} in the resting CTLs (32-33) and n_{cells} in the activated CTLs (39-41). Statistical significance is indicated as follows: n.s. (not significant), *p < 0.05, **p < 0.01 and ***p < 0.001.

On the other hand, in the stimulated CTLs, the PCC analysis showed no significant increase in the correlation of both proteins at the IS and the above IS (Figure 17D). The latter finding contradicts the MOC analysis but might be explained by the fact that MOC and PCC each are calculated using different sets of pixel pairs (Aaron, Taylor, and Chew 2018, 2019). As the MOC calculates the colocalization on the overall threshold regions of the two channels, on the contrary, PCC calculates the linear correlation between the pixel intensities of these signals (Adler and Parmryd 2010; Dunn, Kamocka, and McDonald 2011). So, under certain conditions (like high level of background noise) the output from MOC is more

sensitive to detect a colocalization in comparison to the PCC. In summary, we showed that there is an increased localization of TSP-1-GFPSpark to the CGs over time in culture but no specific MCG over SCG re-localization to the IS at later days in culture. Therefore, our data suggest that the observed increase in MC fusion events in the culture might be attributable to the CG maturation.

3.6 T-cell maturation level has no impact on the endogenous expression levels of TSP-1

To further investigate the endogenous expression of TSP-1, high-quality total RNA was extracted from 5 million WT $CD8^+$ T lymphocytes at different developmental stages: day 0 (naïve CTLs), day 4, and day 8. The isolated RNA was first subjected to a reverse transcription-polymerase chain reaction (RT-PCR) to generate complementary DNA (cDNA), which was subsequently used as a template for specific DNA sequence amplification in cDNA-PCR. Real-time quantitative PCR (RT-qPCR) was then used to quantify TSP-1 gene expression.

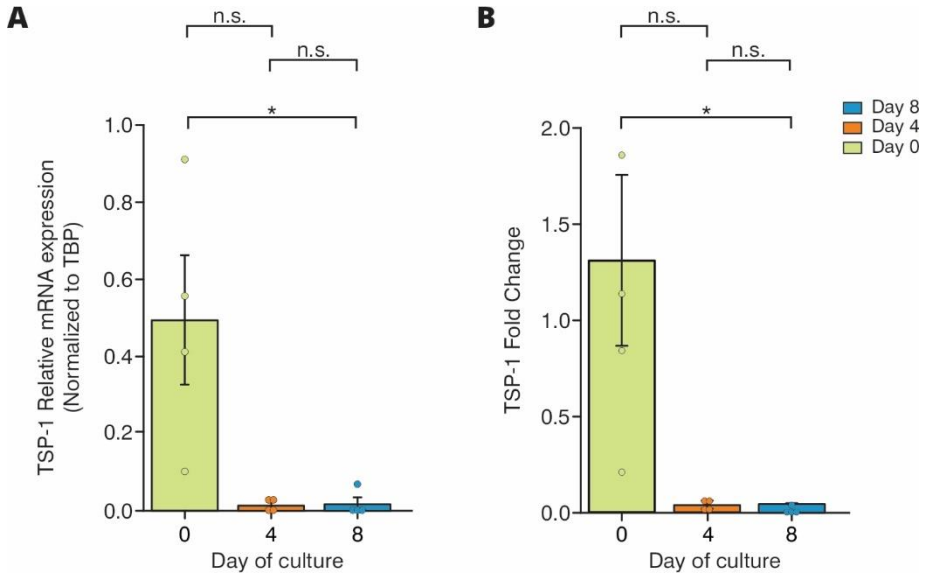

Figure 18: TSP-1 mRNA expression level decreased with culture progression.

RT-qPCR analysis of TSP-1 mRNA was performed on WT-CTLs on days 0, 4, and 8. (A-B) Bar graphs display (A) TSP-1 relative mRNA expression normalized to the housekeeping gene TATA-binding protein (TBP) and (B) TSP-1 fold change. In all bar graphs, error bars are the SEM. Statistical analyses were performed with ANOVA using Tukey Test and Student-Newman-Keuls post-test. N_{mouse}= 4. Statistical significance is indicated as follows: n.s. (not significant) and *$p < 0.05$.

Naïve CTLs exhibited the highest TSP-1 mRNA level of all the groups (0.494 ± 0.1678). By day 4, TSP-1 mRNA expression had decreased significantly to 0.014 ± 0.0079 (p = 0.029, N_{mouse}= 4). Although, a slight increase was observed on day 8, it remained low at 0.018 ± 0.0167 (p = 0.030, N_{mouse}= 4) (Figure 18A). Similarly, TSP-1 gene expression was markedly downregulated by over 30-fold on day 4 and nearly 100-fold on day 8 in comparison to naïve CTLs (Figure 18B). These findings

demonstrated a sharp downregulation of TSP-1 during culture, with no significant changes observed between days 4 and 8. This did not explain the increase in MCG release over time in culture.

3.7 Transmission electron microscopy (TEM) revealed distinct morphological changes in CGs over time in culture

To verify that the observed increase in MC fusion events was due to enhanced MCG biogenesis over time in culture, we performed an ultrastructural analysis of CTLs over time. For this, activated CTLs were harvested on days 4 and 8 of cell culture, incubated for 5-10 minutes at room temperature on PLO (0.1 mg/mL) and anti-CD3ε (30 µg/mL) coated sapphire disks in flat specimen carriers, and subjected to cryopreservation. Post-incubation, the samples were vitrified using a high-pressure freezer. TEM images were acquired following freeze substitution and embedding. On day 4, we observed many uniformly electron-dense SCGs (Figure 19A-C), while we found a small number of MCGs. Furthermore, all CGs appeared relatively small and the MCGs displayed few SMAPs (Figure 19D). By day 8, the abundance of SCGs was reduced and the number of MCGs appeared to increase (Figure 19E-F). The size of the CGs appeared to increase as well as the number of SMAPs per MCGs (Figure 19F).

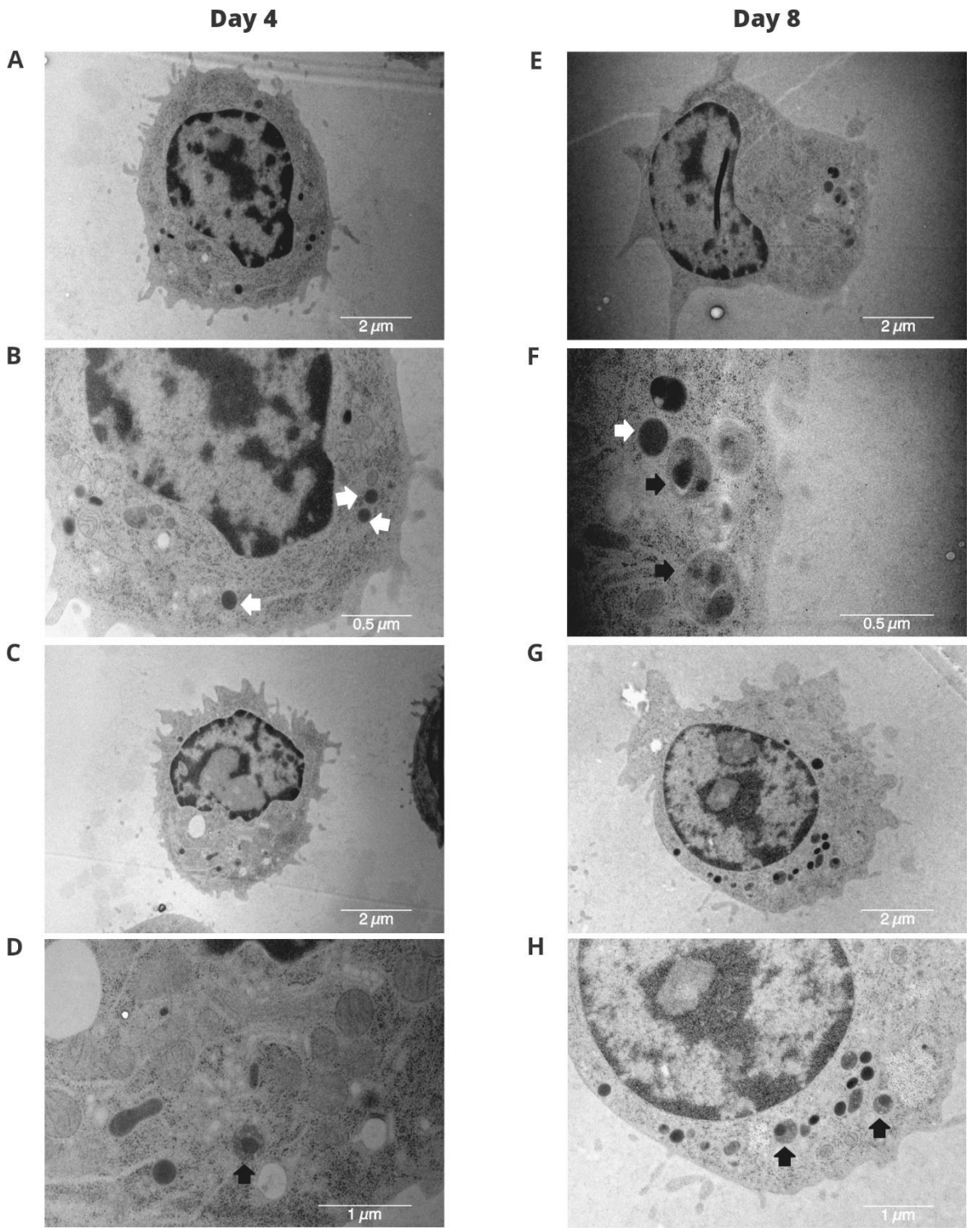

Figure 19: Progressive changes of CGs in CTLs over time in culture.

Four representative TEM images of WT CTLs on (A-D) day 4 and (E-H) day 8 are shown. Panels A, C, E, and G represent the cell overview, while panels B, D, F, and H show magnified portions of the corresponding images. SCGs are indicated with solid white arrows and MCGs with solid black arrows.

3.8 Detection of MCG biogenesis as early as day 4 in culture

The in-depth analysis of the TEM images showed that the number of SCGs per CTL stayed relatively stable over time in culture, starting from an average of about 3 on day 4 to reach 2 on day 8. By contrast, the number of MCGs per CTL almost doubled on day 8 (2 MCGs on average) in comparison to day 4 (1 MCG on average) (Figure 20A). This is also reflected by a stable SCG density and a significant increase in the MCG density in the CTL cytoplasm over time (Figure 20B).

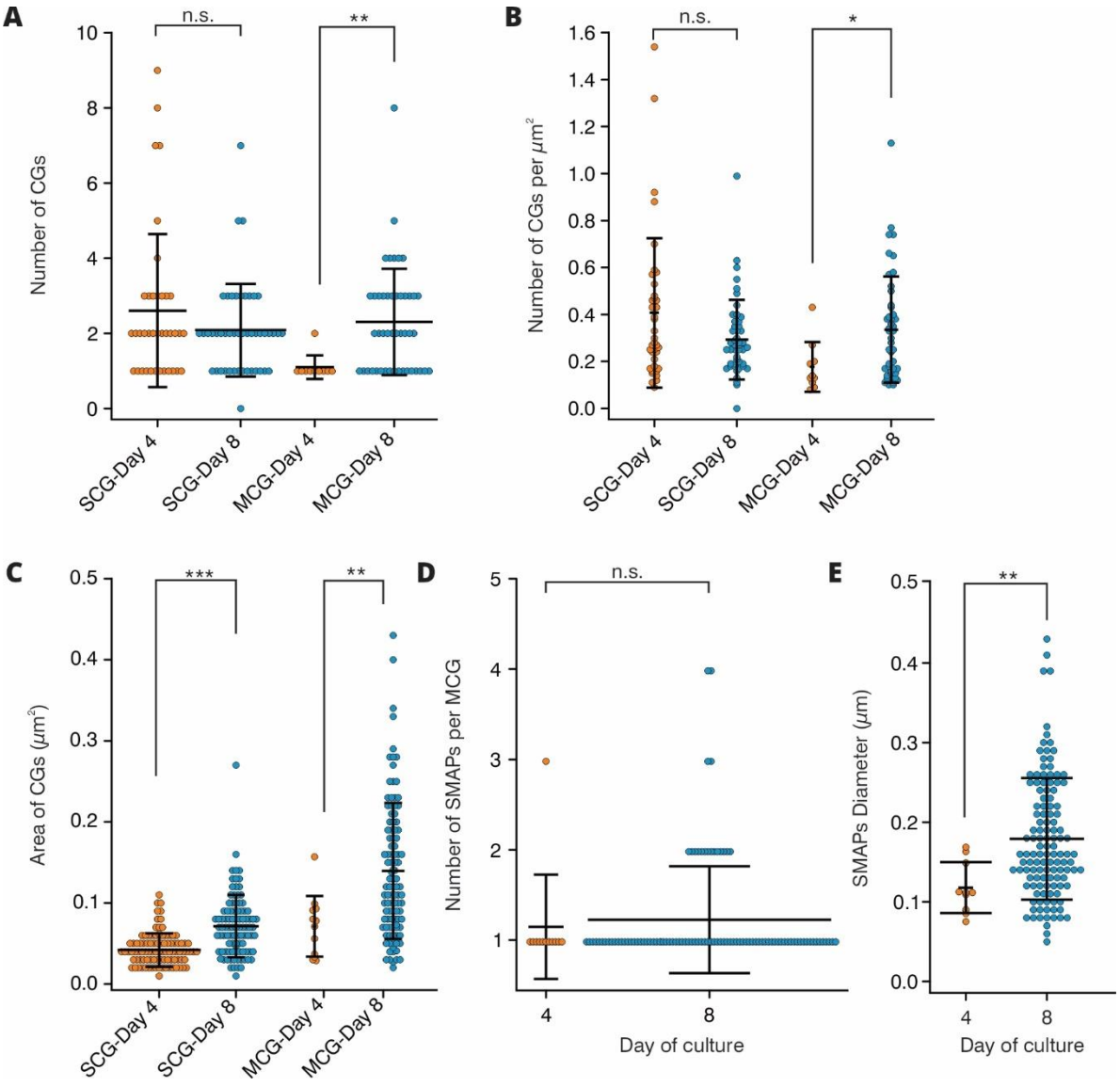

Figure 20: Time in culture enhanced MCG biogenesis in CTLs.

Quantitative analysis of the TEM images of WT CTLs on days 4 and 8 in culture. (A-D) Scatter dot plots display, (A) The total number of CGs per cell, (B) The number of CGs per cytoplasmic area in CTLs surface, (C) Area of SCGs and MCGs (µm^2), (D) Number of SMAPs per MCGs and their (E) Diameter. In all scatter dot plots, the horizontal black line represents the mean and the error bars represent the SD. Statistical analyses were performed using Mann-Whitney Rank Sum Test. N_{mouse}= 2, n_{cells} =27. Statistical significance is indicated as follows: n.s. (not significant), *$p < 0.05$, **$p < 0.01$ and ***$p < 0.001$.

During the culture period, the size of SCGs increased approximately 1.75 times, and MCGs exhibited a two-fold increase in size (Figure 20C). The observed increase in the size of MCGs over time in culture was not attributable to an increase in the number of SMAPs, as their number remained relatively stable (Figure 20D). Instead, the increase in MCG size was due to the increase in the diameter of SMAPs, which underwent a significant enlargement from 0.12 ± 0.01 µm on day 4 to 0.18 ± 0.01 µm on day 8 (p = 0.005, n_{cells} =27) (Figure 20E). In summary, these data suggested that later time in culture induced the biogenesis of MCGs, which might explain the rise in the MC fusion events that was observed with TIRFM (Figure 12C).

3.9 Restimulation of CTLs markedly amplified the number of MC fusion events

Our earlier results demonstrated that the highest percentage of MC fusion events occurred on days 8 and 10 (Figure 12C). Accordingly, we sought to explore whether a second stimulation with anti- CD3/anti-CD28 coated beads might accelerate the maturation of CTLs and enhance the MC fusion events at earlier time points. Based on our previous observation that MC fusion events started on day 6 CTLs (Figure 12C), we proceeded to apply the restimulation methodology (**Materials and Methods 2.2.3**) on day 5 GzmB-tdTomato-KI CTLs. The effect was then measured the following day.

In Figure 21A, the exemplary control CTL, ie. without restimulation, showed one SC fusion event, while the restimulated CTL displayed 4 MC fusion events (Figure 21B). In-depth analysis showed that the restimulation of the CTLs decreased the time of IS formation and had no impact on the number of secreting cells compared to the control (Figure 21C and D). More importantly, the proportion of SC fusion per culture was 97 ± 1.6% for control cells and dropped significantly by 18 % in the restimulated CTLs to 79 ± 3.8% (p = 0.005, n_{cells} = 34) (Figure 21E). Accordingly, the proportion of MC fusion events per culture showed a significant rise in the restimulated CTLs (21 ± 3.8%), as compared to the control (3 ±1.6%) (p = 0.005, n_{cells} = 34) (Figure 21E). Likewise, the percentage of SC fusion events per cell was markedly reduced from 96 ± 1.4% in the control to 88 ± 7.3% (p = 0.002, n_{cells} = 34) in the restimulated CTLs, while the percentage of MC fusion events per cell remarkably increased from 3 ± 1.3% in the control to 18 ± 3.5% (p <0.001, n_{cells} = 34) in the restimulated CTLs (Figure 21F). This result is confirmed by the analysis of the number of SC and MC fusion events per experiment (Figure 21G). Interestingly, the number of SMAPs is doubled in the restimulated CTLs (2.4 ± 0.4 SMAPs) in comparison to control CTLs (1 ± 0 SMAPs, p = 0.003, n_{cells} = 34) Figure (21H).

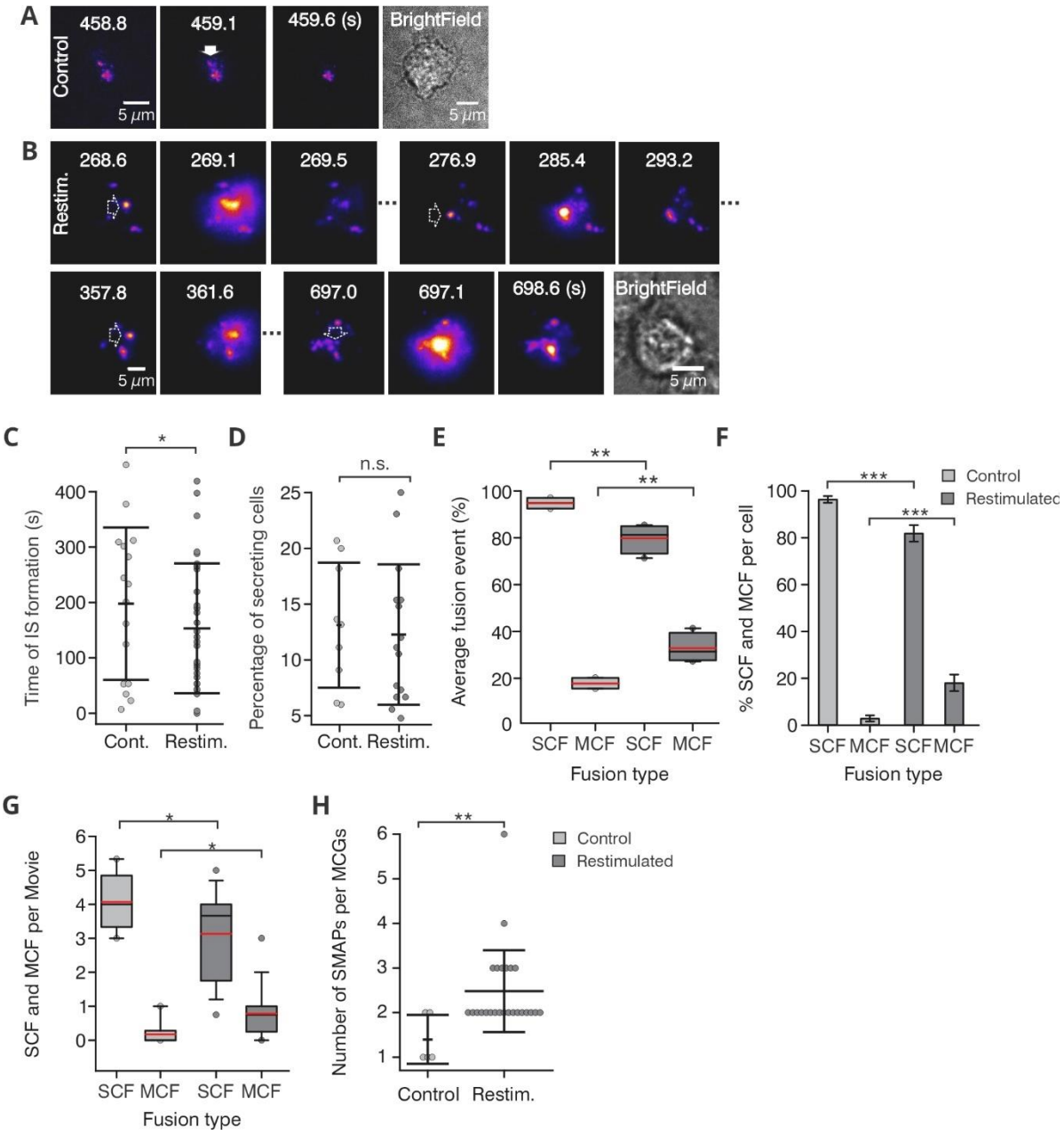

Figure 21: Restimulation substantially boosted MC fusion events in day 6 CTLs.

(A-B) TIRFM snapshots conducted on day 6 in (A) Control and (B) Restimulated GzmB-tdTomato-KI CTLs. The day 6 control CTL showed a single SC fusion event (solid white arrow, (A) that persisted for 0.5 seconds. In contrast, the restimulated CTLs exhibited an increase in MC fusion events (B), with the secretion of four multiple MC fusion events (dotted white arrow). (C-D) Scatter dot plots display (C) Duration that CTLs took to form the IS and (D) The percentage of secreting cells. (E) The box plot shows the percentage of the average fusion events per culture. (F) The average percentage of SC and MC fusion events per cell is presented as a bar graph. (G) The box plot displays the number of SC and MC fusion events per movie. (H) Number of released SMAPs per MCGs is shown as a scatter dot plot. In the box plot, the center red line represents the mean, and the black line indicates the median. The box boundaries show the interquartile range (25th to 75th percentiles), with outliers displayed as individual points beyond the whiskers, which represent the 5th and 95th percentiles. In all scatter dot plots, the horizontal black line represents the mean and error bars represent the SD. In all bar graphs, error bars are SEMs. Statistical analyses were performed using Student's t-test and Mann-Whitney Rank Sum Test. $N_{mice} = 4$, $n_{cells} = 34$. Statistical significance is indicated as follows: n.s. (not significant), $*p < 0.05$, $**p < 0.01$ and $**p < 0.001$.

The effect of the restimulation on different subtypes of $CD8^+$ T cells was checked with flow cytometry (Figure 22A). The percentage of naïve, central memory, and effector memory CTLs were similar in both groups (control and restimulated) of CTLs (Figure 22Bi-iii).

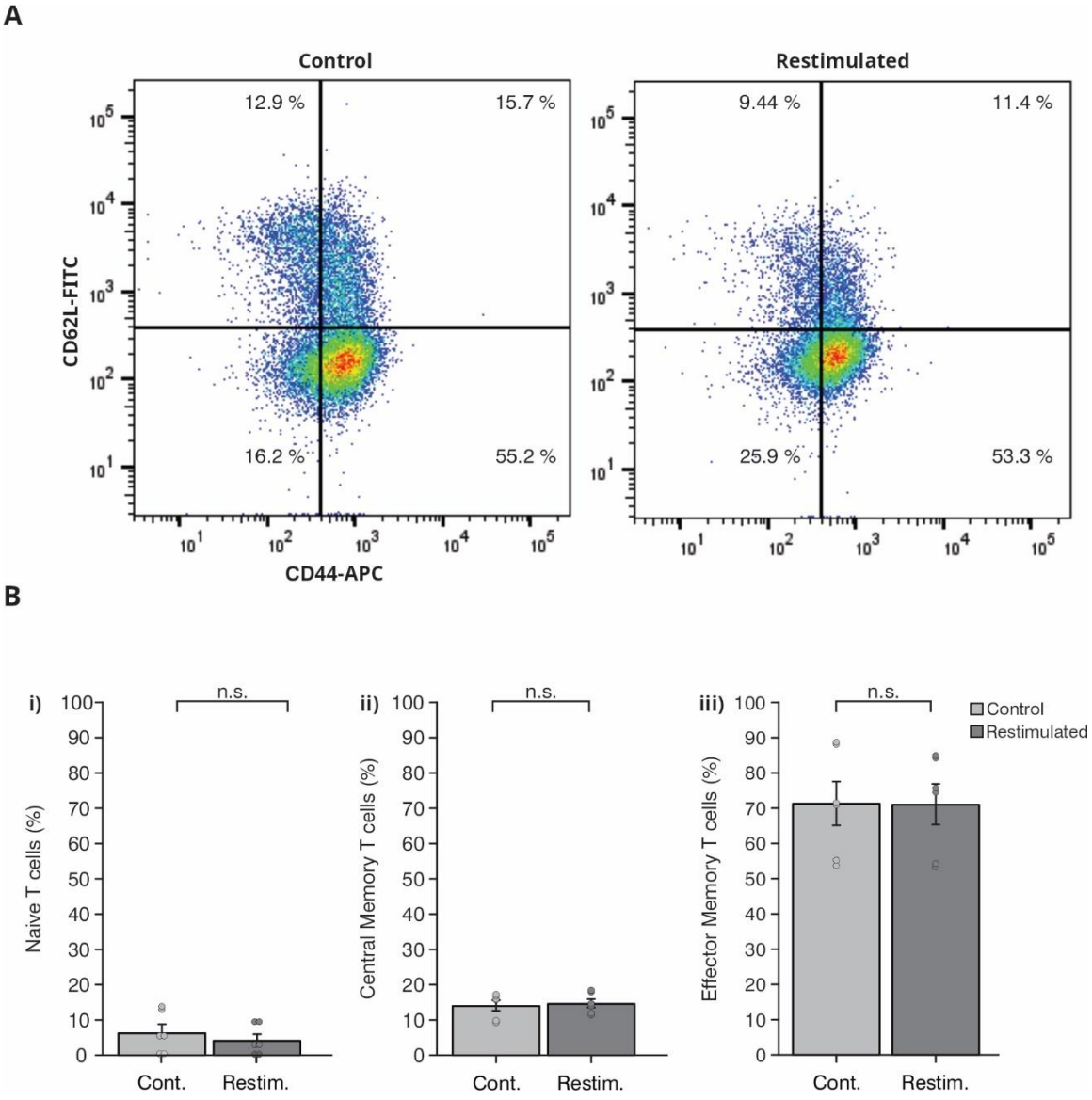

Figure 22: Restimulation had no impact on the subtypes of day 6 CTLs.

(A) Flow cytometry plots of day 6 in both control and restimulated CTLs using FlowJo software. (B) Statistical analyses of both conditions: Control and restimulated on the subtypes of $CD8^+$ T cells: (i) naïve T cells, (ii) central memory and (iii) effector memory. In all bar graphs, error bars are the SEMs. Statistical analyses were performed using Dunn's multiple comparison test. N_{mouse}= 3. Statistical significance is indicated as follows: n.s. (not significant).

In summary, restimulation of CTLs on day 5 likely accelerated the maturation process of MCGs, allowing a significant increase in the number of MC fusion events upon IS formation and doubling the number of SMAPs released per MC fusion event compared to control, without changing the subtypes of CTLs. The question that arises is how the restimulation process influenced the CTLs to induce an

increased number of MC fusion events. One possibility is that restimulation altered the cytokine secretion profile of CTLs, which in turn could have affected the fusion profile of CGs.

3.10 Second stimulation had a major impact on the extracellular level of Interferon-Gamma (IFN-γ)

To test whether the cytokines released by the CTLs influence the type of CG exocytosed by the CTLs, we collected the culture supernatant from control and restimulated day 6 CTLs. The extracellular cytokines were measured using LEGENDplex™ MU Th1 Panel (5-plex) including Interleukin-6 (IL-6), IL-10, IL-2, IFN-γ, and tumor necrosis factor-alpha (TNF-α).

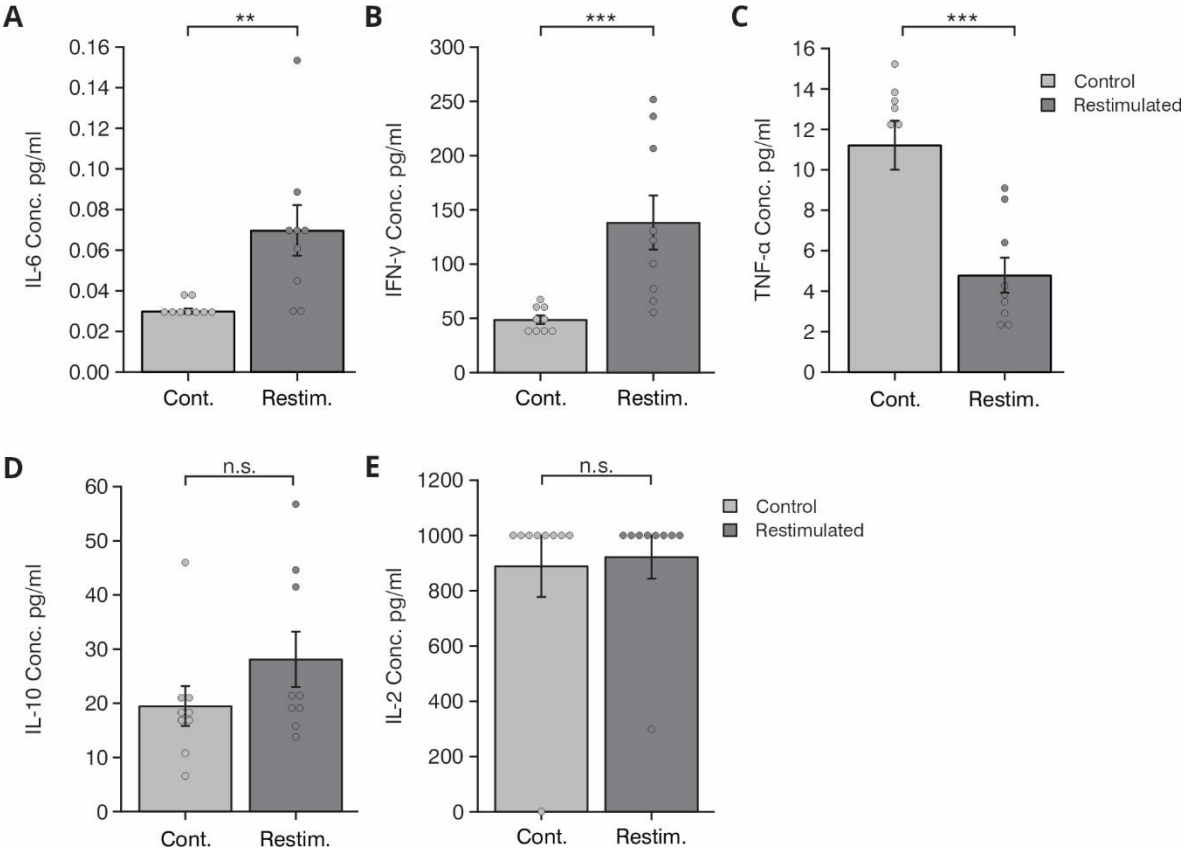

Figure 23: Restimulation had a differential effect on the extracellular cytokines of day 6 CTLs.

(A-E) Bar graphs represent the levels of extracellular cytokines, including (A) IL-6, (B) IFN-γ, (C) TNF-α, (D) IL-10, and (E) IL-2, which were measured on day 6 in both control and restimulated CTLs. In all bar graphs, error bars are SEM. Statistical analyses were performed using Mann-Whitney Rank Sum Test and Student's t-test. N_{mouse}= 3. Statistical significance is indicated as follows: n.s. (not significant), $^{**}p < 0.01$ and $^{***}p < 0.001$.

Restimulation resulted in a significant increase in extracellular IL-6, from 0.03 ± 0.001 to 0.07 ± 0.01 pg/mL (p = 0.005, N_{mouse}= 3) (Figure 23A), IFN-γ, from 48.7 ± 3.9 to 138.32 ± 25 pg/mL (p = 0.001) (Figure 23B), and TNF-α, from 11.2 ± 1.2 to 4.8 ± 0.9 ($p < 0.001$, N_{mouse}= 3) (Figure 23C). However, it

did not affect IL-10 levels (Figure 23D). IL-2 levels remained high due to the addition of recombinant IL-2 to the culture (Figure 23E). Furthermore, the levels of the remaining cytokines were either below the detection threshold or demonstrated no statistically significant change (**Annex**).

In conclusion, the most notable impact of restimulation was observed in the level of IFN-γ, which demonstrated the most pronounced increase compared to the other cytokines.

3.11 Cyclosporin A (CsA) modified the fusion profile of CG in older CTLs

The marked alterations in cytokine levels after restimulation (Figure 23) underscore their potential involvement in the fusion process. To gain a deeper insight into the underlying mechanisms, we intend to utilize CsA, a highly efficacious inhibitor of cytokine production in CTLs (Matsubara et al. 2021). This would allow an examination of the impact of cytokine production inhibition on the fusion machinery, particularly on days 4 and 8.

CsA was applied to the $CD8^+$ T-lymphocyte culture at a final concentration of 5 µg/mL, in accordance with the methodology outlined by Hajkova et al. (2017). Given that CsA has an inhibitory effect on IL- 2, which is crucial for T-cell proliferation, 100 U/mL of IL-2 was also incorporated into the culture. CsA increased the time for IS formation on day 4, from 44 ±15 to 101±31.2 seconds ($p = 0.045$, n_{cells} =12-36), but had no effect on IS formation at later time in culture (Figure 24A). Moreover, the addition of CsA did not affect the percentage of secreting cells (Figure 24B). The number of SC and MC fusion events on day 4 was not affected by the CsA treatment of the CTLs. This holds whether they are expressed as average percentage per culture (Figure 24C) or average percentage per cell (Figure 24D) or number of SCGs per movie (Figure 24E).

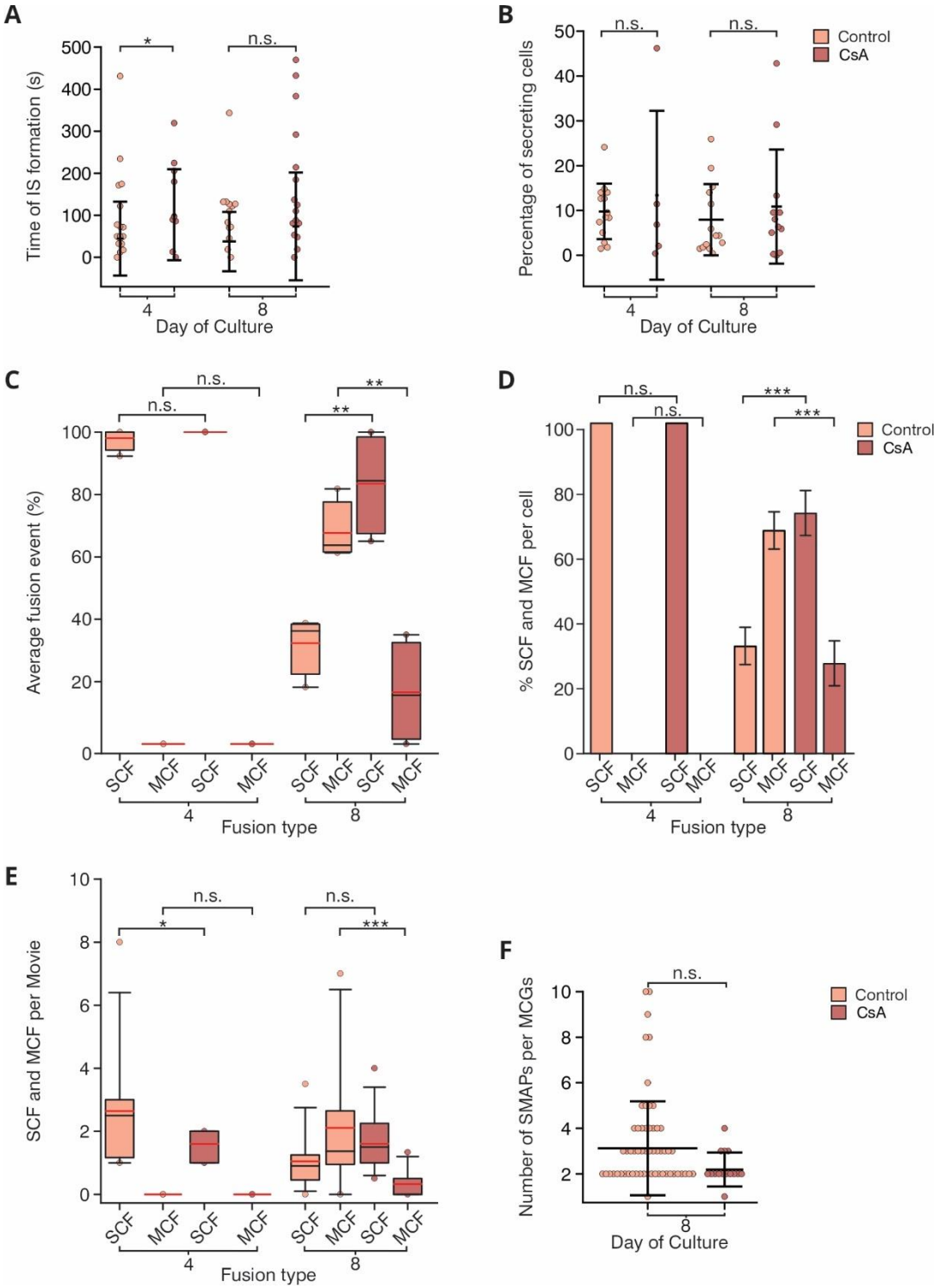

Figure 24: CsA negatively impacted the MC fusion events later in culture.

Demonstration of the analyzed data from TIRFM conducted on days 4 and 8 in both control and CsA-treated CTLs. (A-B) Scatter dot plots display (A) Duration CTLs took to form IS and (B) The percentage of secreting cells. (C) A box plot shows the percentage of the average fusion events per culture. (D) The average percentage of SC and MC fusion events per cell is presented as a bar graph. (E) A box plot displays the number of SC and MC fusion events per movie, (F) Number of released SMAPs per MCGs is shown as a scatter dot plot. In the box plot, the center red line represents the mean, and the black line indicates the median. The box boundaries show the interquartile range (25th to 75th percentiles), with outliers displayed as individual points beyond the whiskers, which represent the 5th and 95th percentiles. The colored circles highlight outliers that fall outside this range. In all scatter dot plots, the horizontal black line represents the mean and

error bars represent the SD. In all bar graphs, error bars are the SEMs. Statistical analyses were performed using Mann-Whitney Rank Sum Test and Student's t-test. N_{mouse} =2-4 on day 4, n_{cells} =12-36, on day 8, n_{cells} = 37. Statistical significance is indicated as follows: n.s. (not significant), *$p < 0.05$, **$p < 0.01$ and ***$p < 0.001$.

On the contrary, CsA treatment on day 8 induced an increase in the number of SC fusion events and a clear decrease in MC fusion events. Both fusion types were significantly altered when expressed as percentages (Figure 25D). However, due to strong cell-to-cell variability, significant changes were observed only in fusion events on day 8. On day 4, the number of SC fusion events decreased significantly from 2.6 ± 0.5 in the control to 1.6 ± 0.24 in the treated CTLs ($p = 0.013$, n_{cells} =12-36). On day 8, the number of MC fusion events per movie was significantly reduced upon CsA treatment, dropping from 2.1 ± 0.5 in the control to 0.3 ± 0.1 in the treated cells ($p < 0.0001$, n_{cells} = 37 Figure 25E). Finally, the number of SMAPs released during the MC fusion events was not changed by the CsA treatment of the cells. Note that, due to the absence of MC fusion events in both groups at day 4, no SMAPs were secreted as well (Figure 24F).

These data suggest that main effect of CsA was on day 8, it increased the number of SC fusion events and decreased the number of MC fusion events with a non-significant drop in the number of released SMAPs.

3.12 CsA did not change the subtypes of CTLs over time in culture

To fully understand the effect of CsA on the subtypes of T cells, flow cytometry measurement was performed (Figure 25). Analysis of the data showed a slight, non-significant change induced by CsA especially in the effector memory CTLs in more mature cells (day 8). However, this slight change probably did not explain the effect of CsA on the number of MC fusion events. In light of the impact of CsA treatment on CG fusion type and its capacity to suppress the release of diverse cytokines in CTLs. It is crucial to ascertain which cytokines are most influenced by CsA treatment.

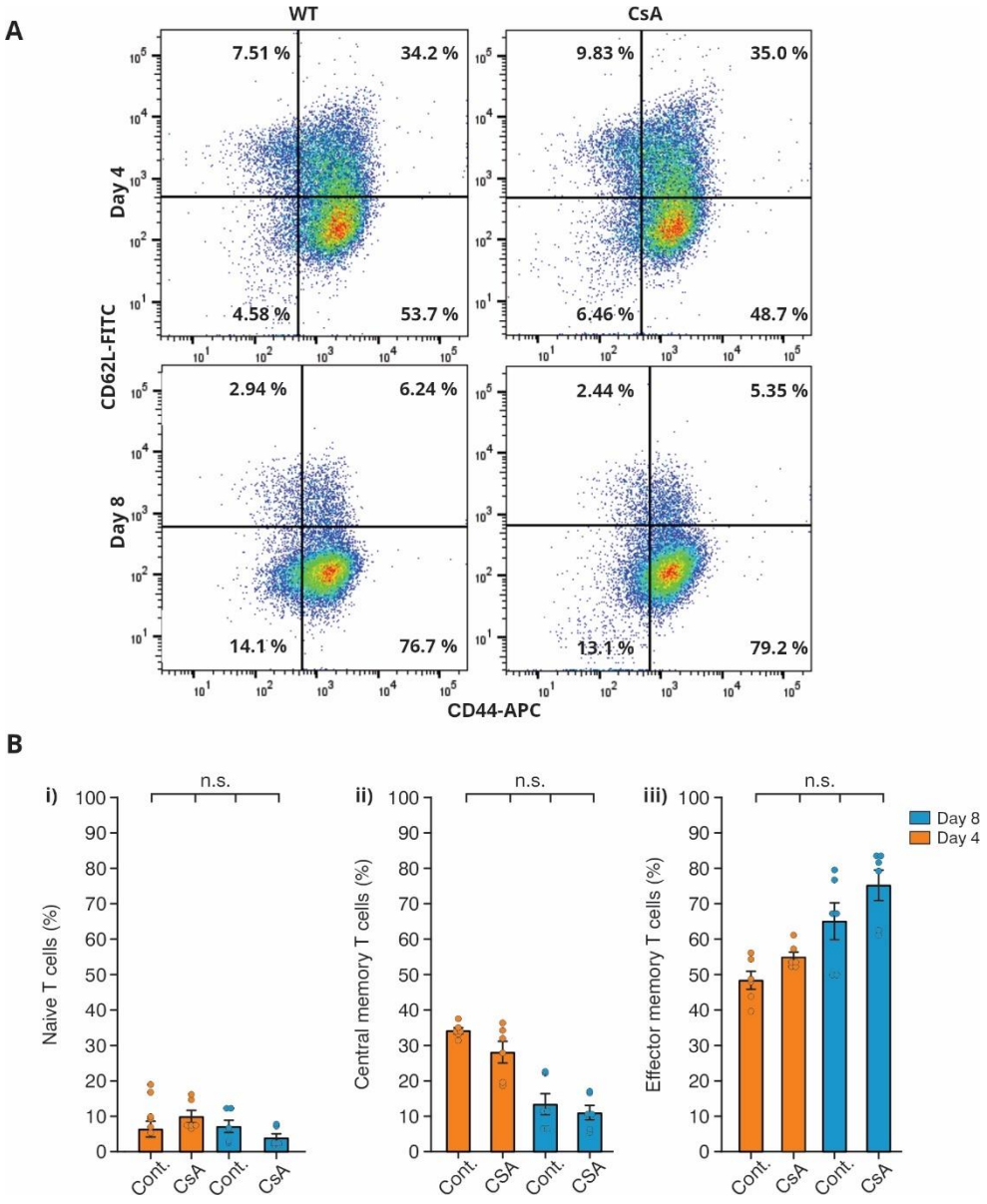

Figure 25: CsA did not affect the different subtypes of CTLs.

(A) Display of the flow cytometry plots of days 4 and 8 in both control and CsA-treated CTLs using FlowJo software. (B) Statistical analyses of the effect of time in culture on different subtypes of both control and CsA-treated $CD8^+$ T cells; (i) naïve T cells, (ii) central memory and (iii) effector memory. In all bar graphs, error bars are the SEM. Statistical analyses were performed using Dunn's multiple comparison test. N_{mouse}= 3. Statistical significance is indicated as follows: n.s. (not significant).

3.13. CsA modulated the secretion of extracellular cytokines in CTLs

The extracellular cytokines, including IL-6, IL-10, IL-2, IFN-γ, and TNF-α, were measured using the LEGENDplex™ MU Th1 Panel (5-plex) in the supernatants collected from both control and CsA-treated groups on two different maturation days: days 4 and 8.

The level of IL-6 significantly decreased in the control cells from 0.39 ± 0.28 pg/mL on day 4 to 0.05 ± 0.00 pg/mL on day 8 (p = 0.014, N_{mouse}= 3, Figure 26A). The concentration of IFN-γ was the highest

on day 4 at 365.76 ± 115.12 pg/mL and declined significantly by a factor of 10 to 34.66 ± 18.65 pg/mL on day 8 (p = 0.009, N_{mouse}= 3, Figure 26B). Interestingly, CsA treatment significantly reduced IFN-γ levels on both days, with concentrations of 145.09 ± 31.77 pg/mL on day 4 and 17.30 ± 10.85 pg/mL on day 8 (p = 0.001, N_{mouse}= 3, Figure 26B). In contrast, the extracellular TNF-α levels remained unchanged, regardless of the culture day or CsA treatment (Figure 26C).

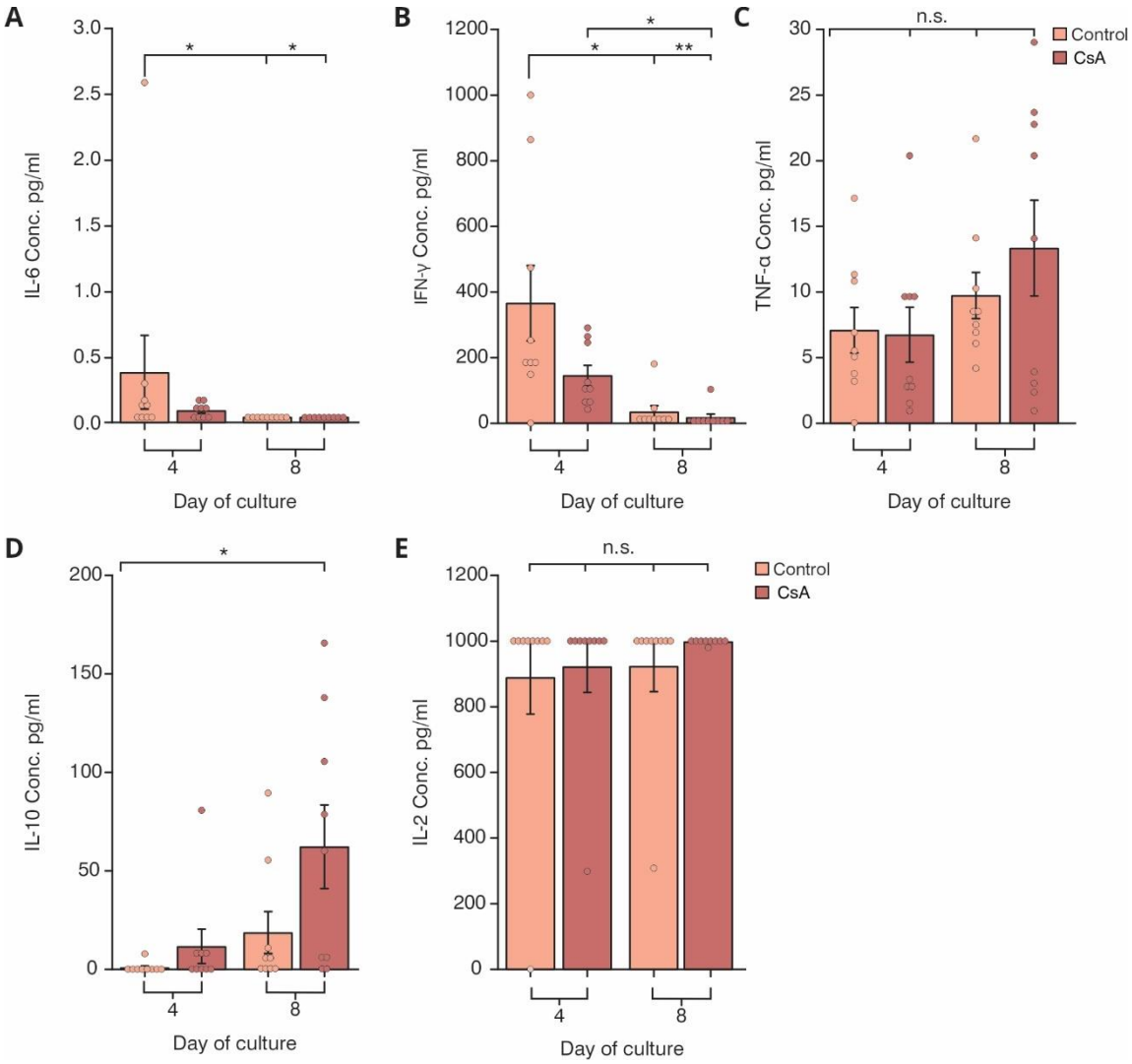

Figure 26: CsA had variable effects on the levels of extracellular cytokines in CTLs.

(A-E) Bar graphs represent the levels of extracellular cytokines, including (A) IL-6, (B) IFN-γ, (C) TNF-α, (D) IL-10, and (E) IL-2, were measured in both the control and CsA-treated CTLs. In all bar graphs, error bars are the standard error of the mean (SEM). Statistical analyses were performed using Mann-Whitney Rank Sum Test and Equal Student's t-test. N_{mouse}= 3. Statistical significance is indicated as follows: n.s. (not significant), *p < 0.05 and **p < 0.01.

IL-10 levels showed high variability across cultures. Although IL-10 concentrations increased over time from 0.89 ± 0.86 pg/mL on day 4 to 18.71 ± 10.62 pg/mL on day 8 (p = 0.004, N_{mouse}= 3), this increase was not significant (Figure 26D). Similarly, CsA treatment increased IL-10 concentrations on both days (11.70 ± 8.73 pg/mL on day 4 and 62.26 ± 21.27 pg/mL on day 8), but these changes were not

statistically significant (Figure 26D). Finally, CsA did not affect IL-2 levels (Figure 26E)., as recombinant IL-2 was added to the culture in both groups to support T-cell proliferation (Liddicoat and Lavelle 2019).

According to the previous finding, the addition of CsA has a significant impact on various extracellular cytokines including IL-6, IL-10, IFN-γ and TNF-α. Given the varying detection thresholds, IFN-γ was identified as the cytokine that could be most reliably detected, as levels of other measured cytokines were below the established limit of detection (**Annex**). Therefore, it would be interesting to check both the endogenous and the exogenous levels of the IFN-γ and how specifically removing IFN-γ would affect MC fusion events.

3.14. Reduction in IFN-γ mRNA expression levels over time during culture

The endogenous expression of IFN-γ in CTLs was studied using Real-time quantitative PCR (RT-qPCR). A high-quality total RNA was extracted from wild-type $CD8^+$ T lymphocytes at various stages of development, specifically on days 0 (naïve CTLs), 4, and 8. This procedure was summarized in the **Materials and Methods section 2.2.15**. Day 4 CTLs displayed the highest IFN-γ mRNA expression level, with an average of 1.4 (relative expression normalized to TBP) with a significant difference to both naïve and day 8, in which they both have low levels of 0.5 and 0.6 (Figure 27A). To compare the IFN-γ gene upregulation or downregulation between naïve and later maturation stages of CTLs, IFN-γ fold change was calculated in comparison to the naïve CTLs. IFN-γ gene expression level was downregulated around 2.48 times on naïve and day 8 CTLs compared to day 4, which was at 3.05 (Figure 27 B).

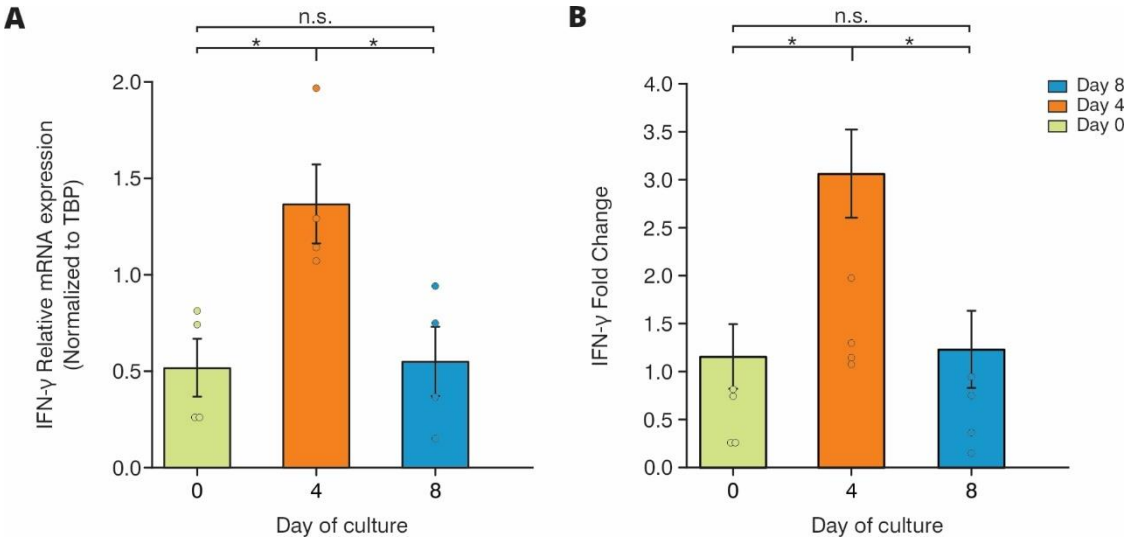

Figure 27: Cell maturation affected IFN-γ mRNA expression levels.

RT-qPCR analysis of IFN-γ mRNA was performed on WT-CTLs on days 0, 4, and 8. Bar graphs display (A) IFN-γ relative mRNA expression normalized to the housekeeping gene TATA-binding protein (TBP) and (B) IFN-γ fold

change. In all bar graphs, error bars are the standard error of the mean (SEM). Statistical analyses were performed using the Multiple Comparison Procedures Holm-Sidak method. N_{mouse}= 4. Statistical significance is indicated as follows: n.s. (not significant) and *$p < 0.05$.

3.15 IFN-γ modulated the fusion profile of CGs in day 8 CTLs

Previous data revealed that both the extracellular and the endogenous levels of IFN-γ were significantly reduced over time in culture (Figures 26B and 27). Therefore, it is tempting to hypothesize that the level of IFN-γ can impact the biogenesis of MCGs and, consequently, allow MC fusion events to occur upon IS formation. To test this hypothesis, we aimed to remove the free IFN-γ from the culture supernatant. For this, we used an excess of specific anti-IFN-γ that we added to the culture medium. The highest concentration of the extracellular IFN-γ that we detected was 365.76 ± 115.12 pg/mL in the supernatant of day 4 old CTL (Figure 26B). Thus, we used the anti-IFN-γ at a dilution of 1:200, which corresponds to a final concentration of 5 µg/mL. This antibody was added to the CTLs culture starting from day 2 till day 7. Release of the SC and MC fusion events was assessed by overexpressing GzmB-pHuji and imaging using TIRFM on culture days 4 and 8.

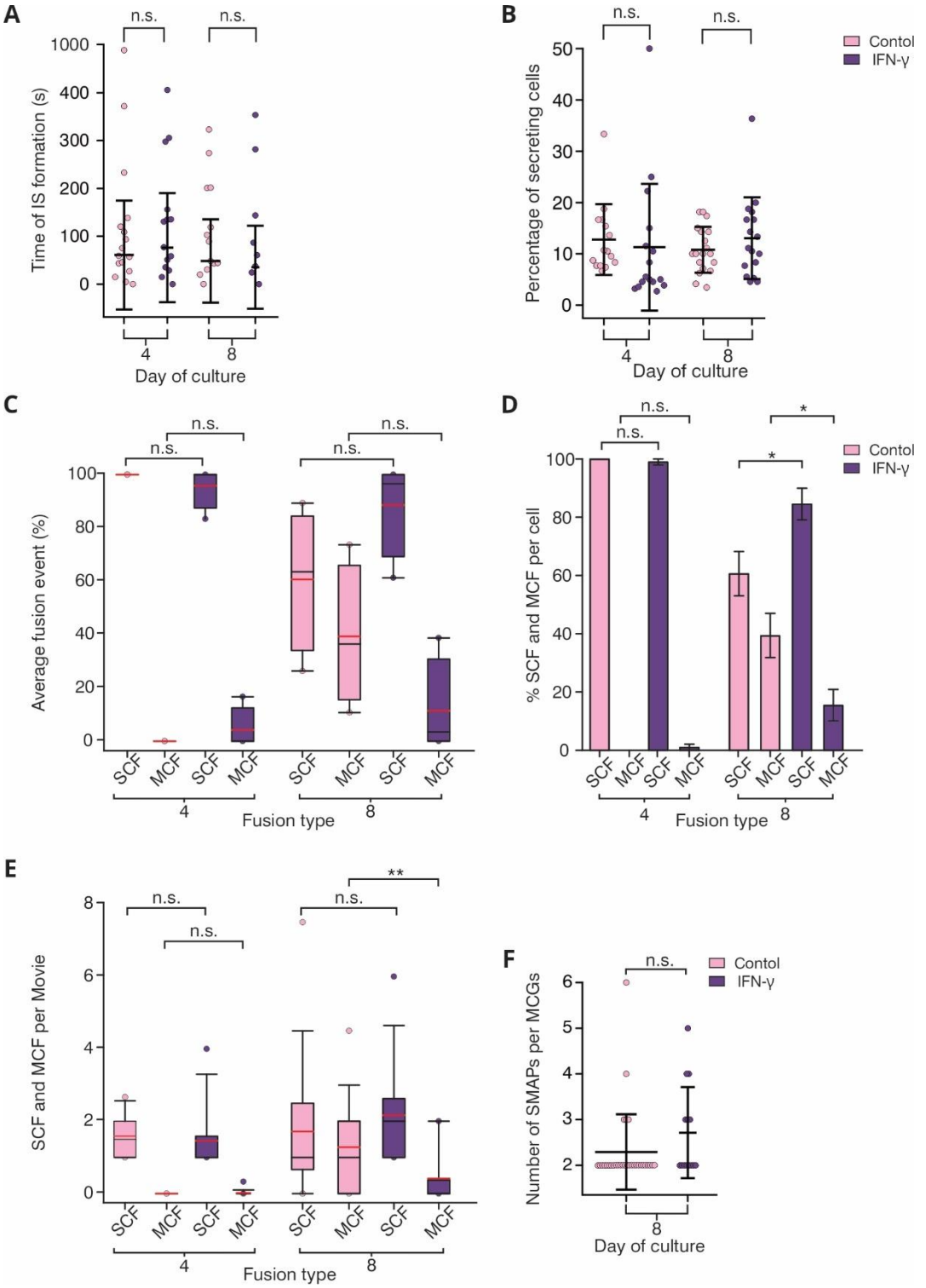

Figure 28: Anti-mouse IFN-γ reduced MC fusion events on more mature CTLs in culture.

Presentation of the analyzed data from TIRFM conducted on days 4 and 8 in both control and anti-IFN-γ-treated CTLs. (A-B) Scatter dot plots display (A) Duration CTLs took to form IS and (B) The percentage of secreting cells. (C) A box plot shows the percentage of the average fusion events per culture. (D) The average percentage of SC and MC fusion events per cell is presented as a bar graph. (E) A box plot displays the number of SC and MC fusion events per movie. (F) Number of released SMAPs per MCGs is shown as a scatter dot plot. In the box plot, the center red line represents the mean, and the black line indicates the median. The box boundaries show the interquartile range (25th to 75th percentiles), with outliers displayed as individual points beyond the whiskers, which represent the 5th and 95th percentiles. The colored circles highlight

outliers that fall outside this range. In all scatter dot plots, the horizontal black line represents the mean and error bars represent the standard deviation (stdev). In all bar graphs, error bars are the standard error of the mean (SEM). Statistical analyses were performed using Mann-Whitney Rank Sum Test. N_{mouse} =2-4 on day 4, n_{cells} =12-36, on day 8, n_{cells} =37. Statistical significance is indicated as follows: n.s. (not significant), *$p < 0.05$, **$p < 0.01$ and ***$p < 0.001$.

Anti-IFN-γ antibody treatment did not change the time of IS formation nor the percentage of the secreting cells (Figures 28A and B). On day 4, antibody treatment did not alter the CG fusion profile. However, on day 8, an increase in SC fusion events and a decrease in MC fusion events were observed (Figure 28C, E). Despite this, the differences were not significant due to large cell-to-cell variability. These differences became more apparent by expressing the data as percent SC and MC fusion per cell. On day 8, SC fusion events increased from 60.61 ± 7.81% in the control to 83.8 ± 5.6% in the treated cells ($p = 0.030$, n_{cells} =37), while MC fusion events decreased from 40.1 ± 7.7% in the control to 14.8 ± 5.3% in the treated cells ($p = 0.015$, n_{cells} =37) (Figure 28D). Furthermore, the number of SMAPs remained consistent between control and treated cells. On day 4, the control had no SMAPs as there were no MC fusion events, while the anti-IFN-γ-treated group had only one MC fusion event with 2 SMAPs. On day 8, SMAPs released from the MC fusion events in the anti-IFN-γ-treated group were around 3 SMAPs per MC fusion event. While in the control group, the average of the secreted SMAPs was around 2 SMAPs per MC fusion event (Figure 28F). These data suggested that IFN-γ plays an important role in regulating the secretion of MCGs at later days in culture.

4. Discussion

In recent years, immunotherapy has been revolutionary in cancer treatment by targeting and destroying cancer cells using the body's immune system. Nevertheless, tumor cells exploit a series of biochemical pathways to reduce the cytotoxicity of cytotoxic T lymphocytes (CTLs). This enables tumor cells to escape recognition and elimination by the immune system (Tuomela, Ambrose, and Davis 2022). In adaptive cell therapy, CTLs are expanded ex vivo and re-introduced into the patient to enhance their ability to target and eliminate cancer cells. My work focused on understanding the factors that influence CTL cytotoxicity, to develop innovative immunotherapies that avoid the need for long-term ex vivo expansion.

4.1 The strength of TCR stimulation did not influence the fusion profile of CGs in CTLs

Various in vivo studies have shown the complex relationship between antigen strength using anti-CD3ε and T-cell cytotoxicity (Billeskov et al. 2017; Kaech, Wherry, and Ahmed 2002). For more in vitro investigation, my study tested a range of biotinylated anti-CD3ε concentrations. (5, 10, 20 µg\mL) on anti-CD3/anti-CD28 bead-stimulated CTLs seeded on supported lipid bilayer (SLB). This was done along with fixed concentrations of Intercellular Adhesion Molecule 1 (ICAM-1), to have a stable adhesion mechanism, that helps in studying T-cell signaling and immune synapse (IS) formation. Using Total Internal Reflection Fluorescence Microscopy (TIRFM) and sufficient extracellular Ca^{2+}, we observed the exocytosis of cytotoxic granules (CGs) labeled via GzmB-pHuji overexpression. We found that 10 µg/mL antiCD3ε concentration represented the optimal T-cell receptor (TCR) stimulus for the rapid induction of CTL adhesion to the SLB in agreement with Estl et al. (2020). It was observed that 10 µg/mL of anti-CD3ε increased slightly the percentage of the secreting CTLs. We hypothesized that this may be due to the formation of a more stable IS at this concentration. This finding is consistent with the hypothesis proposed by Estl et al. (2020), which suggests that the stability of the IS is dependent on the strength of the TCR stimulus. Different TCR stimuli showed no effect on the number of the released supramolecular attack particles (SMAPs) (Figure 10F). An in-depth investigation of the data showed that the number of single-core (SC) and multi-core (MC) fusion events might be affected by the culture days (days 5, 6, 7, and 8). This prompted the question: could earlier or later periods in the culture, while using the optimal TCR stimulus, potentially lead to a change in the secretion profile of CTLs?

4.2 Different times in culture boosted the MCG secretion in CTLs

To address the previous question, wild-type (WT) CTLs overexpressing GzmB-pHuji were imaged at culture days 4, 6, 8, and 10 using TIRFM. This study revealed that later culture times promoted faster and more stable IS formation, possibly due to faster-acting reorganization at the IS (Valitutti et al. 1995). Actin reorganization has been demonstrated to facilitate the orientation of the microtubule-

organizing center (MTOC) (Yamamoto et al. 2022), thereby increasing the number of secreting CTLs and improving the secretion efficiency of the CTLs. We found that younger CTLs (day 4) in culture secreted solely single core granules (SCGs). As they mature with the prolongation of the culture, CTLs progressively increased the quantities of MC fusion events. A comprehensive examination of the data indicated that the quantity of SMAPs released from MCGs remained constant throughout the study. This degree of consistency is likely attributable to the stability of the processes involved in the generation and \ or packaging of SMAPs within MCGs throughout the culture period. It was unclear whether the difference in the type of CG fusion reflected different T cell subsets. Next, T cell subsets were examined using different cell surface markers, clusters of differentiation 62L (CD62L) and CD44, via flow cytometry. This study indicated that the time in culture didn't change the CTLs subtypes. This might be explained as both central and effector memory cells reached a dynamic equilibrium rapidly after central memory cells differentiated into effector memory T cells upon antigenic stimulation (Sallusto, Geginat, and Lanzavecchia 2004). The equilibrium between both subsets is important for the orchestration of an efficacious immune response, thereby emphasizing the adaptive flexibility of T cells in response to stimuli.

4.3 Identification of an intermediate form of CG by WGA

To verify that time in culture increased MC fusion events, WT CTLs overexpressing GzmB-pHuji on days 4, 6, 8, and 10 were exogenously labeled with Wheat germ agglutinin (WGA). WGA is a lectin that is known to bind to the glycoprotein shell of SMAPs (Bálint et al. 2020). Statistical analysis showed that WGA did not interfere with the secretion machinery (Figure 12A). Exogenous labeling with WGA not only confirmed that the culture duration influenced the mode of CG fusion but also led to the identification of a novel CG category. This finding aligns with the study by Cassioli et al., which revealed heterogeneity in MCG through using fluorescent WGA labeling in live CTLs, indicating sequential transport with TSP-1 being introduced at a later stage in MCG biogenesis than TSP-4 (Cassioli et al. 2024). This new category was found to exhibit fusion dynamics similar to those of SCGs, along with a glycoprotein content characteristic of SMAPs.

It is noteworthy that this novel category of CG exhibited an inverse correlation with the duration of the culture period, which suggested that it may represent a transitional stage preceding MCG assembly. The maximum number of SC fusion events that were WGA^+ was observed on day 4, while the number of MC fusion events peaked on day 8. Subsequent studies will therefore concentrate on days 4 and 8 to gain further insight into these differences.

4.4 TSP-1 trafficking and colocalization is related to the maturation of CTLs

The objective of this experiment was to ascertain whether culture time affects CG trafficking, and thereby their release, and to determine whether this process is driven by TCR stimulation or T cell maturation. To address that aim, CTLs from days 4 and 8 of GzmB-tdTomato-KI mice were modified to overexpress TSP-1-GFPSpark, which is known to be associated with MCGs. They were seeded on coverslips with or without stimulation of anti-CD3 and imaged with SIM. An analysis of the CG labeling with GzmB-tdTomato and TSP-1-GFPSpark was done.

TSP-1 exhibited different patterns of intracellular localization on days 4 and 8. On day 4, the TSP- 1-GFPSpark was observed to be distributed rather uniformly throughout the cytoplasm and additionally on a few punctate structures. While on day 8, the TSP-1 was found in larger punctate structures with less dispersed cytoplasmic signal. This observation was confirmed by measuring the coefficient of variation (CV) that assessed the variability of the TSP-1-GFPSpark signal. The CV analysis confirmed the relocalization of TSP-1-GFPSpark from the cytoplasm to a punctate form. That might be explained as TSP-1 was trafficked and colocalized with CG to support SMAP assembly. Notably, this relocalization occurred irrespective of whether T cells were unstimulated or stimulated, indicating that it is more likely attributable to cellular maturation. To further explore this relocalization, the colocalization of TSP-1-GFPSpark with granzyme B (GzmB) was examined. In both resting and stimulated conditions, GzmB-tdTomato demonstrated higher colocalization with TSP-1-GFPSpark on day 8 than on day 4. Similarly, TSP-1-GFPSpark displayed enhanced colocalization with GzmB-tdTomato on day 8 than on day 4, which can be primarily related to higher quantities of MCGs and the release of SMAPs during this period (Figure 12C).

On day 4, a partial colocalization of TSP-1-GFPSpark with GzmB-tdTomato was observed, which suggested that MCGs may be initially present early in the culture. This data indicated a significant difference in the TSP1-GFPSpark trafficking between days 4 and 8. However, these findings may be the result of artifacts caused by the overexpression of TSP-1-GFPSpark. This issue could have been addressed with the use of an appropriate mouse model co-expressing GzmB-tdTomato and TSP1-GFPSpark, or by using an appropriate anti-TSP-1 antibody. As these solutions were not available, an investigation was conducted into the endogenous TSP-1 mRNA levels during CTL maturation. The results of the RT-qPCR analysis demonstrated downregulation of TSP-1 expression on days 4 and 8 in comparison to naïve CTLs. This finding is aligned with the observations reported by Cassioli et al. (2024), who documented a comparable decline in TSP-1 expression in human $CD8^+$ T cells. Despite this reduction, the residual TSP-1 levels remained sufficient to contribute to SMAP formation, as proposed by the Cassioli et al. study. The variable expression levels of TSP-1 were already described by Li et al. (2006), who emphasized that TSP-1 expression and function are subject to dynamic regulation in response to T cell activation.

4.5 Early MCG biogenesis was observed on day 4

To confirm the previous observation that the generation of MCG was found to be initiated on day 4. Days 4 and 8 CTLs were seeded on anti-CD3ε coated sapphire discs and imaged using transmission electron microscopy (TEM). The results of the study showed that the number of SCGs on days 4 and 8 remained constant. On day 8, there was an observed increase in the abundance of larger MCGs, along with an elevation in the size of SMAPs compared to day 4. These findings might explain the increased MC fusion events on day 8. This result also suggests that, at day 4, CTLs may primarily rely on SCG secretion as their main attack mechanism. In contrast, the older CTLs on day 8 appear to adopt a dual strategy, possibly maintaining secretion of larger SCG, which are likely to contain more GzmB, while also utilizing MCGs with larger SMAPs as an extension of their attack arsenal.

As the previous data indicated MCG biogenesis is already detectable on day 4, so it is of interest to consider strategies to accelerate SMAP production in CTLs, to optimize their cytotoxic functionality for further therapeutic applications.

4.6 CTL restimulation: A catalyst for enhanced SMAP production

My approach involved restimulation on day 5 and TIRFM imaging on the next day using GzmB-tdTomato-KI CTLs, as earlier restimulation (e.g., on day 4) might disrupt the maturation of the CTLs.

This strategy was designed to target T cells at the stage when they begin secreting MCGs along with SCGs (Figure 12C), thereby maximizing the release of MCGs and possibly the biogenesis of SMAPs. Restimulation was observed to enhance T cell functionality, evidenced by the acceleration of IS formation and elevation of MC fusion events. This was achieved without any alteration to T cell subtypes. This method raised a new question: Could the pronounced effects of restimulated CTLs result from alterations in intracellular machinery, particularly in cytokine production?

To answer this question, a multiplex bead-based assay was employed to quantify pro-inflammatory cytokines (IFN-γ: Interferon-gamma, TNF-α: Tumor Necrosis Factor-alpha, IL-6: Interleukin-6), anti-inflammatory cytokines (IL-10), and regulatory cytokines (IL-2, used as a control) in CTLs. Along with the consistent exogenous application of the IL-2, restimulation was observed to enhance the production of IFN-γ and IL-6, which are key pro-inflammatory cytokines that are known to promote $CD8^+$ T cell cytotoxic activity. The observed increase in IL-6 may result from the synergistic effect between IFN-γ and TNF-α, as they have been shown to work together to activate IL-6 expression in immune cells (Adhikari et al. 2020). Concurrently, there was a reduction in TNF-α level, indicating a shift toward a cytokine profile that is more optimized for cytotoxic responses. Unaltered IL-10 levels indicated that restimulation preserves immune equilibrium while enhancing cytotoxic functionality. It is also crucial to acknowledge that the levels of IL-6, TNF-α, and IL-10 were measured at the limit of detection. This observation necessitates a cautious interpretation of the findings and the need for further investigation.

The change in the cytokine profile after restimulation led to the question of whether changes in the mode of CG release are also associated with extracellular cytokine levels. Addressing this issue requires the use of immunosuppressive drugs such as cyclosporin A (CsA), which are known to affect cytokine production in T cells (Liddicoat and Lavelle 2019).

4.7 CsA altered the fusion profile of CGs in CTLs at a later stage in culture

CsA, a calcineurin inhibitor, reduces T-cell proliferation and the production of various cytokines. CsA achieves this by forming a complex with cyclophilin A and inhibiting the calcineurin-NFAT signaling pathway (Lee, Kim, and Choi 2018). As a result, CsA modulates the production of several cytokines including IL-2 and effector cytokines such as IFN-γ, and TNF-α (Andersson et al. 1992; Liu et al. 1991). In this study, CsA was introduced to the culture on day 2 and maintained at a constant level until day 7, in conjunction with an exogenous supply of IL-2. By adding IL-2, it is ensured that cellular proliferation is maintained. CsA influenced the timing of IS formation exclusively during the initial phase of the culture period, without affecting the percentage of secreting CTLs. More importantly, on day 8, CsA altered the mode of fusion, shifting from MC fusion events to SC fusion events. These effects of CsA on CTLs at different time points in culture were noted without any alterations to the CTL subtypes. Also, CsA did not affect the amount of SMAPs released within the MCG.

At the extracellular cytokine level, CsA caused a notable decline in IFN-γ and a slight reduction in IL- 6. This may be due to the inhibition of the nuclear factor of activated T-cells (NFAT)-dependent gene expression by CsA (Tomono et al. 1996). IFN-γ has been linked to the effective response of CTLs (Salerno et al. 2017), which could be responsible for the shift in the mode of CG fusion caused by CsA. Also, CsA did not change the level of TNF-α and IL-10 observed across culture days. This result could be explained as IL-10 production is already stimulated by IL-2 and IFN-γ (Cohen et al. 1997; Schandené et al. 1997; Schandené et al. 1996). Even though the CsA is well-known for its ability to suppress T-cell responses, our observations indicated that CG is still being released from T cells. Two potential explanations for this finding have been proposed. Firstly, T cells may activate the mechanistic target of Rapamycin complex (mTORC1) pathway to circumvent CsA-induced immunosuppression and ensure their survival, as proposed by Wißfeld et al. (2024). Secondly, the exogenous IL-2 supplied in the culture may have interacted with other cytokines as part of a regulatory mechanism, thereby mitigating the effects of CsA. We established that modifications in the fusion profile may be attributable to alterations at the extracellular cytokine level.

My investigation indicated that the primary alterations in fusion type of CG might be associated with the inhibition of IFN-γ production which was observed at two levels: extracellularly (Figure 26), and intracellularly at the mRNA level (Figure 27). Therefore, it would be beneficial to explore deeply the role of IFN-γ in cell culture.

4.8 IFN-γ: A key intracellular modulator driving MC fusion events

To investigate the role of IFN-γ on the CG mode of fusion, anti-IFN-γ antibody was applied to the culture till day 7. TIRFM analysis revealed that anti-IFN-γ antibody treatment had no impact on IS formation or the percentage of secreting cells. Furthermore, the anti-IFN-γ antibody demonstrated a similar effect to that observed with CsA, namely a shift in the fusion profile from MC to SC fusion events. This evidence lends support to the hypothesis proposed by Bhat et al. (2017b), that $CD8^+$ T cells depend on autocrine IFN-γ to maintain their cytolytic and kinetic functions. Given that, it is hypothesized that the primary action of CsA may be through the suppression of IFN-γ. These findings emphasize the critical role of IFN-γ in orchestrating cytotoxicity, where it serves as a cytotoxic cytokine in combination with granzyme B and perforin, ultimately initiating apoptosis in tumor cells (Maimela, Liu, and Zhang 2019; Tau et al. 2001).

5. Outlook

The recognition of an intermediate form of cytotoxic granules (CGs) has the potential to facilitate a deeper comprehension of the morphology, biogenesis, and functional role of single core granules (SCGs) and multicore granules (MCGs) (Bálint et al. 2020). However, further investigation is necessary to ascertain whether the intermediate form is directly involved in the biogenesis of MCGs. This could assist in identifying the regulatory factors influencing MCG release and elucidating the distinct roles of SCGs, MCGs, and the intermediate form.

To gain more in-depth insight, the intermediate form can be characterized using mass spectrometry to identify its protein composition and elucidate its provenance within the biogenesis pathway. This will facilitate a more comprehensive understanding of the trafficking mechanisms that regulate granule maturation and their subsequent release. Furthermore, an examination of the correlation between IFN- γ and other proteins involved in the trafficking process, such as Munc13, as well as SNARE proteins, including VAMP2/7/8 and SNAP23, will provide insights into their functions within the context of CG trafficking and secretion pathways. Functional assays, such as killing assays, may be employed to evaluate the efficacy of SCGs, MCGs, and the intermediate form in CTL-mediated target cell killing. This will assist in identifying the functional role of each granule type and determining whether the intermediate form contributes to cytotoxicity. Furthermore, size exclusion liquid chromatography (Jainarayanan et al. 2023) can be employed to isolate supramolecular attack particles (SMAPs) from the restimulated day 6 CTLs and control day 8 to investigate the differences in their composition and function.

In light of the observed effect of IFN-γ on MCG release, further investigation into its role in granule biogenesis is warranted. To this end, correlative electron microscopy in conjunction with a GzmBtd-Tomato knock-in mouse model, can be employed to visualize granule biogenesis and maturation in IFN-γ-depleted cells on day 8. This approach will elucidate whether IFN-γ exerts an influence not only on MCG release but also on the preceding processes of biogenesis and maturation.

A pulse-chase protocol can be used to elucidate the biogenesis pathways and intracellular origins of SCGs, MCGs, and the intermediate form. The temporal dynamics of granule formation can be monitored by electroporating mouse WT cells with the pMAX-Granzyme B-L-HaloTag construct (for labeling both MCG and SCG). Afterward, a fluorescent ligand for HaloTag like Janelia Fluor® will be added for a short period (pulse) and then followed with a nonfluorescent HaloTag as HaloTag® Biotin Ligand over a period of time (chase). When setting up the pulse-chase protocol, several factors will need to be checked, such as the incubation time required for Janelia Fluor® to stain the newly synthesized lytic granules. and the ability of the Halo Tag® biotin to block the signal from the pMAX Granzyme B-L Halo Tag. Live cell imaging and biochemical validation can then be used to monitor the dynamics of granule biogenesis over time. Colocalization studies can be conducted using markers for

distinct intracellular compartments (TGN46 for trans-Golgi network, LAMP1 for lysosomes, Rab5 for early endosomes, and Rab7 for late endosomes). By integrating colocalization studies with correlative electron microscopy, we will provide a comprehensive understanding of granule trafficking and maturation.

In conclusion, further research integrating molecular characterization, colocalization studies, and functional assays will be essential to elucidate the complex pathways governing SCG, MCG, and intermediate granule biogenesis. This will not only enhance our understanding of granule maturation and trafficking but also clarify their role in CTL cytotoxicity and immune regulation.

6. References

Aaron, J. S., A. B. Taylor, and T. L. Chew. 2018. 'Image co-localization - co-occurrence versus correlation', *J Cell Sci*, 131.

———. 2019. 'The Pearson's correlation coefficient is not a universally superior colocalization metric. Response to 'Quantifying colocalization: the MOC is a hybrid coefficient - an uninformative mix of co-occurrence and correlation'', *J Cell Sci*, 132.

Abbas, A. K., E. Trotta, R. Simeonov D, A. Marson, and J. A. Bluestone. 2018. 'Revisiting IL-2: Biology and therapeutic prospects', *Sci Immunol*, 3.

Adams, J. C., A. A. Bentley, M. Kvansakul, D. Hatherley, and E. Hohenester. 2008. 'Extracellular matrix retention of thrombospondin 1 is controlled by its conserved C-terminal region', *J Cell Sci*, 121: 784-95.

Adhikari, A., B. Cobb, S. Eddington, N. Becerra, P. Kohli, A. Pond, and J. Davie. 2020. 'IFN-γ and CIITA modulate IL-6 expression in skeletal muscle', *Cytokine X*, 2: 100023.

Adkins, B., K. Chun, K. Hamilton, and M. Nassiri. 1996. 'Naive murine neonatal T cells undergo apoptosis in response to primary stimulation', *J Immunol*, 157: 1343-9.

Adler, J., and I. Parmryd. 2010. 'Quantifying colocalization by correlation: the Pearson correlation coefficient is superior to the Mander's overlap coefficient', *Cytometry A*, 77: 733-42.

Alarcón, B., D. Mestre, and N. Martínez-Martín. 2011. 'The immunological synapse: a cause or consequence of T-cell receptor triggering?', *Immunology*, 133: 420-5.

Andersson, J., S. Nagy, C. G. Groth, and U. Andersson. 1992. 'Effects of FK506 and cyclosporin A on cytokine production studied in vitro at a single-cell level', *Immunology*, 75: 136-42.

Atkinson, E. A., M. Barry, A. J. Darmon, I. Shostak, P. C. Turner, R. W. Moyer, and R. C. Bleackley. 1998. 'Cytotoxic T lymphocyte-assisted suicide. Caspase 3 activation is primarily the result of the direct action of granzyme B', *J Biol Chem*, 273: 21261-6.

Ayroldi, E., O. Zollo, L. Cannarile, D' Adamio F, U. Grohmann, D. V. Delfino, and C. Riccardi. 1998. 'Interleukin-6 (IL-6) prevents activation-induced cell death: IL-2-independent inhibition of Fas/fasL expression and cell death', *Blood*, 92: 4212-9.

Azzi, J. R., M. H. Sayegh, and S. G. Mallat. 2013. 'Calcineurin inhibitors: 40 years later, can't live without', *J Immunol*, 191: 5785-91.

Baenziger, N. L., G. N. Brodie, and P. W. Majerus. 1972. 'Isolation and properties of a thrombin-sensitive protein of human platelets', *J Biol Chem*, 247: 2723-31.

Balaji, K. N., N. Schaschke, W. Machleidt, M. Catalfamo, and P. A. Henkart. 2002. 'Surface cathepsin B protects cytotoxic lymphocytes from self-destruction after degranulation', *J Exp Med*, 196: 493-503.

Bálint, Š, S. Müller, R. Fischer, B. M. Kessler, M. Harkiolaki, S. Valitutti, and M. L. Dustin. 2020. 'Supramolecular attack particles are autonomous killing entities released from cytotoxic T cells', *Science*, 368: 897-901.

Beresford, P. J., D. Zhang, D. Y. Oh, Z. Fan, E. L. Greer, M. L. Russo, M. Jaju, and J. Lieberman. 2001. 'Granzyme A activates an endoplasmic reticulum-associated caspase-independent nuclease to induce single-stranded DNA nicks', *J Biol Chem*, 276: 43285-93.

Bhat, P., G. Leggatt, N. Waterhouse, and I. H. Frazer. 2017a. 'Interferon-gamma derived from cytotoxic lymphocytes directly enhances their motility and cytotoxicity', *Cell Death Dis*, 8: e2836.

———. 2017b. 'Interferon-γ derived from cytotoxic lymphocytes directly enhances their motility and cytotoxicity', *Cell Death Dis*, 8: e2836.

Billeskov, R., Y. Wang, S. Solaymani-Mohammadi, B. Frey, S. Kulkarni, P. Andersen, E. M. Agger, Y. Sui, and J. A. Berzofsky. 2017. 'Low Antigen Dose in Adjuvant-Based Vaccination Selectively Induces CD4 T Cells with Enhanced Functional Avidity and Protective Efficacy', *J Immunol*, 198: 3494-506.

Blott, E. J., and G. M. Griffiths. 2002. 'Secretory lysosomes', *Nat Rev Mol Cell Biol*, 3: 122-31.

Bolte, S., and F. P. Cordelières. 2006. 'A guided tour into subcellular colocalization analysis in light microscopy', *J Microsc*, 224: 213-32.

Borel, J. F., C. Feurer, H. U. Gubler, and H. Stähelin. 1994. 'Biological effects of cyclosporin A: a new antilymphocytic agent. 1976', *Agents Actions*, 43: 179-86.

Boulanger, M. J., D. C. Chow, E. E. Brevnova, and K. C. Garcia. 2003. 'Hexameric structure and assembly of the interleukin-6/IL-6 alpha-receptor/gp130 complex', *Science*, 300: 2101-4.

Boyman, O., H. P. Hefti, C. Conrad, B. J. Nickoloff, M. Suter, and F. O. Nestle. 2004. 'Spontaneous development of psoriasis in a new animal model shows an essential role for resident T cells and tumor necrosis factor-alpha', *J Exp Med*, 199: 731-6.

Bromberg, J. S., K. D. Chavin, and S. L. Kunkel. 1992. 'Anti-tumor necrosis factor antibodies suppress cell-mediated immunity in vivo', *J Immunol*, 148: 3412-7.

Buelens, C., F. Willems, A. Delvaux, G. Piérard, J. P. Delville, T. Velu, and M. Goldman. 1995. 'Interleukin-10 differentially regulates B7-1 (CD80) and B7-2 (CD86) expression on human peripheral blood dendritic cells', *Eur J Immunol*, 25: 2668-72.

Burkhardt, J. K., S. Hester, C. K. Lapham, and Y. Argon. 1990. 'The lytic granules of natural killer cells are dual-function organelles combining secretory and pre-lysosomal compartments', *J Cell Biol*, 111: 2327-40.

Caputo, A., R. S. Garner, U. Winkler, D. Hudig, and R. C. Bleackley. 1993. 'Activation of recombinant murine cytotoxic cell proteinase-1 requires deletion of an amino-terminal dipeptide', *J Biol Chem*, 268: 17672-5.

Cassioli, Chiara, Nagaja Capitani, Claire C. Staton, Claudia Schirra, Francesca Finetti, Anna Onnis, Nadia Alawar, Szu-Min Tu, Ludovica Lopresti, Vanessa Tatangelo, Carmela Tangredi, Salvatore Valvo, Hsin-Fang Chang, Annachiara Miccoli, Ewaldus B. Compeer, Jemma Nicholls, Bruce Blazar, Giuseppe Marotta, Matthew J. A. Wood, Livio Trentin, Laura Patrussi, Michael L. Dustin, Ute Becherer, and Cosima T. Baldari. 2024. 'Thrombospondins 1 and 4 undergo coordinated transport to multicore cytotoxic granules to regulate SMAP biogenesis and function in CTL-mediated cytotoxicity', *bioRxiv*: 2024.04.25.590546.

Chang, H. F., C. Schirra, M. Ninov, U. Hahn, K. Ravichandran, E. Krause, U. Becherer, Š Bálint, M. Harkiolaki, H. Urlaub, S. Valitutti, C. T. Baldari, M. L. Dustin, R. Jahn, and J. Rettig. 2022. 'Identification of distinct cytotoxic granules as the origin of supramolecular attack particles in T lymphocytes', *Nat Commun*, 13: 1029.

Chang, H. F., C. Schirra, V. Pattu, E. Krause, and U. Becherer. 2023. 'Lytic granule exocytosis at immune synapses: lessons from neuronal synapses', *Front Immunol*, 14: 1177670.

Chitirala, P., H. F. Chang, P. Martzloff, C. Harenberg, K. Ravichandran, M. H. Abdulreda, P. O. Berggren, E. Krause, C. Schirra, T. Leinders-Zufall, F. Benseler, N. Brose, and J. Rettig. 2020. 'Studying the biology of cytotoxic T lymphocytes in vivo with a fluorescent granzyme B-mTFP knock-in mouse', *Elife*, 9.

Chitirala, P., K. Ravichandran, D. Galgano, M. Sleiman, E. Krause, Y. T. Bryceson, and J. Rettig. 2019. 'Cytotoxic Granule Exocytosis From Human Cytotoxic T Lymphocytes Is Mediated by VAMP7', *Front Immunol*, 10: 1855.

Chitirala, P., K. Ravichandran, C. Schirra, H. F. Chang, E. Krause, U. Kazmaier, M. A. Lauterbach, and J. Rettig. 2020. 'Role of V-ATPase a3-Subunit in Mouse CTL Function', *J Immunol*, 204: 2818-28.

Chouaib, Abed Alrahman, Hsin-Fang Chang, Omnia M. Khamis, Santiago Echeverry, Lucie Demeersseman, Sofia Elizarova, James A Daniel, Salvatore Valitutti, Sebastian Barg, Constantin Pape, Ali H. Shaib, and Ute Becherer. 2024. 'Highly adaptable deep-learning platform for automated detection and analysis of vesicle exocytosis', *bioRxiv*: 2024.08.02.606323.

Cohen, S. B., S. L. Parry, M. Feldmann, and B. Foxwell. 1997. 'Autocrine and paracrine regulation of human T cell IL-10 production', *J Immunol*, 158: 5596-602.

Comrie, W. A., A. Babich, and J. K. Burkhardt. 2015. 'F-actin flow drives affinity maturation and spatial organization of LFA-1 at the immunological synapse', *J Cell Biol*, 208: 475-91.

Davis, S. J., and P. A. van der Merwe. 2001. 'The immunological synapse: required for T cell receptor signalling or directing T cell effector function?', *Curr Biol*, 11: R289-91.

Dawson, D. W., S. F. Pearce, R. Zhong, R. L. Silverstein, W. A. Frazier, and N. P. Bouck. 1997. 'CD36 mediates the In vitro inhibitory effects of thrombospondin-1 on endothelial cells', *J Cell Biol*, 138: 707-17.

Diehl, S. A., H. Schmidlin, M. Nagasawa, B. Blom, and H. Spits. 2012. 'IL-6 triggers IL-21 production by human CD4+ T cells to drive STAT3-dependent plasma cell differentiation in B cells', *Immunol Cell Biol*, 90: 802-11.

Dienz, O., and M. Rincon. 2009. 'The effects of IL-6 on CD4 T cell responses', *Clin Immunol*, 130: 27-33.

Dudenhöffer-Pfeifer, M., C. Schirra, V. Pattu, M. Halimani, M. Maier-Peuschel, M. R. Marshall, U. Matti, U. Becherer, J. Dirks, M. Jung, P. Lipp, M. Hoth, M. Sester, E. Krause, and J. Rettig. 2013. 'Different Munc13 isoforms function as priming factors in lytic granule release from murine cytotoxic T lymphocytes', *Traffic*, 14: 798-809.

Dunn, K. W., M. M. Kamocka, and J. H. McDonald. 2011. 'A practical guide to evaluating colocalization in biological microscopy', *Am J Physiol Cell Physiol*, 300: C723-42.

Dustin, M. L., T. Starr, R. Varma, and V. K. Thomas. 2007. 'Supported planar bilayers for study of the immunological synapse', *Curr Protoc Immunol*, Chapter 18: 18.13.1-18.13.35.

Estl, M., P. Blatt, X. Li, U. Becherer, H. F. Chang, J. Rettig, and V. Pattu. 2020. 'Various Stages of Immune Synapse Formation Are Differently Dependent on the Strength of the TCR Stimulus', *Int J Mol Sci*, 21.

Feldmann, J., I. Callebaut, G. Raposo, S. Certain, D. Bacq, C. Dumont, N. Lambert, M. Ouachée-Chardin, G. Chedeville, H. Tamary, V. Minard-Colin, E. Vilmer, S. Blanche, F. Le Deist, A. Fischer, and G. de Saint Basile. 2003. 'Munc13-4 is essential for cytolytic granules fusion and is mutated in a form of familial hemophagocytic lymphohistiocytosis (FHL3)', *Cell*, 115: 461-73.

Fowler, K. T., N. W. Andrews, and J. W. Huleatt. 2007. 'Expression and function of synaptotagmin VII in CTLs', *J Immunol*, 178: 1498-504.

Galvin, J. P., L. H. Spaeny-Dekking, B. Wang, P. Seth, C. E. Hack, and C. J. Froelich. 1999. 'Apoptosis induced by granzyme B-glycosaminoglycan complexes: implications for granule-mediated apoptosis in vivo', *J Immunol*, 162: 5345-50.

Gillis, S., and K. A. Smith. 1977. 'Long term culture of tumour-specific cytotoxic T cells', *Nature*, 268: 154-6.

Golubovskaya, V., and L. Wu. 2016. 'Different Subsets of T Cells, Memory, Effector Functions, and CAR-T Immunotherapy', *Cancers (Basel)*, 8.

Grakoui, A., S. K. Bromley, C. Sumen, M. M. Davis, A. S. Shaw, P. M. Allen, and M. L. Dustin. 1999. 'The immunological synapse: a molecular machine controlling T cell activation', *Science*, 285: 221-7.

Griffiths, G. M., and S. Isaaz. 1993. 'Granzymes A and B are targeted to the lytic granules of lymphocytes by the mannose-6-phosphate receptor', *J Cell Biol*, 120: 885-96.

Gruenberg, J., and H. Stenmark. 2004. 'The biogenesis of multivesicular endosomes', *Nat Rev Mol Cell Biol*, 5: 317-23.

Haasters, F., W. C. Prall, D. Anz, C. Bourquin, C. Pautke, S. Endres, W. Mutschler, D. Docheva, and M. Schieker. 2009. 'Morphological and immunocytochemical characteristics indicate the yield of early progenitors and represent a quality control for human mesenchymal stem cell culturing', *J Anat*, 214: 759-67.

Hajkova, M., B. Hermankova, E. Javorkova, P. Bohacova, A. Zajicova, V. Holan, and M. Krulova. 2017. 'Mesenchymal Stem Cells Attenuate the Adverse Effects of Immunosuppressive Drugs on Distinct T Cell Subopulations', *Stem Cell Rev Rep*, 13: 104-15.

Hartono, C., T. Muthukumar, and M. Suthanthiran. 2013. 'Immunosuppressive drug therapy', *Cold Spring Harb Perspect Med*, 3: a015487.

Hay, Z. L. Z., and J. E. Slansky. 2022. 'Granzymes: The Molecular Executors of Immune-Mediated Cytotoxicity', *Int J Mol Sci*, 23.

Henkart, P. A. 1985. 'Mechanism of lymphocyte-mediated cytotoxicity', *Annu Rev Immunol*, 3: 31-58.

Homann, D., L. Teyton, and M. B. Oldstone. 2001. 'Differential regulation of antiviral T-cell immunity results in stable CD8+ but declining CD4+ T-cell memory', *Nat Med*, 7: 913-9.

Isenberg, J. S., D. S. Annis, M. L. Pendrak, M. Ptaszynska, W. A. Frazier, D. F. Mosher, and D. D. Roberts. 2009. 'Differential interactions of thrombospondin-1, -2, and -4 with CD47 and effects on cGMP signaling and ischemic injury responses', *J Biol Chem*, 284: 1116-25.

Ivanova, M. E., N. Lukoyanova, S. Malhotra, M. Topf, J. A. Trapani, I. Voskoboinik, and H. R. Saibil. 2022. 'The pore conformation of lymphocyte perforin', *Sci Adv*, 8: eabk3147.

Jainarayanan, A. K., J. Capera, P. F. Céspedes, M. Conceição, M. Elanchezhian, T. Thomas, S. Bonner, S. Valvo, E. Kurz, R. S. Mahla, G. Berridge, S. Hester, R. Fischer, L. B. Dustin, M. J. A. Wood, and M. L. Dustin. 2023. 'Comparison of different methods for isolating CD8(+) T lymphocyte-derived extracellular vesicles and supramolecular attack particles', *J Extracell Biol*, 2: e74.

Jawed, J. J., S. Dutta, and S. Majumdar. 2019. 'Functional aspects of T cell diversity in visceral leishmaniasis', *Biomed Pharmacother*, 117: 109098.

Jorgovanovic, D., M. Song, L. Wang, and Y. Zhang. 2020. 'Roles of IFN-γ in tumor progression and regression: a review', *Biomark Res*, 8: 49.

Joseph, N., B. Reicher, and M. Barda-Saad. 2014. 'The calcium feedback loop and T cell activation: how cytoskeleton networks control intracellular calcium flux', *Biochim Biophys Acta*, 1838: 557-68.

Kaech, S. M., E. J. Wherry, and R. Ahmed. 2002. 'Effector and memory T-cell differentiation: implications for vaccine development', *Nat Rev Immunol*, 2: 251-62.

Kägi, D., A. Ho, B. Odermatt, A. Zakarian, P. S. Ohashi, and T. W. Mak. 1999. 'TNF receptor 1-dependent beta cell toxicity as an effector pathway in autoimmune diabetes', *J Immunol*, 162: 4598-605.

Kaiser, C. A., and R. Schekman. 1990. 'Distinct sets of SEC genes govern transport vesicle formation and fusion early in the secretory pathway', *Cell*, 61: 723-33.

Kataoka, T., M. Schröter, M. Hahne, P. Schneider, M. Irmler, M. Thome, C. J. Froelich, and J. Tschopp. 1998. 'FLIP prevents apoptosis induced by death receptors but not by perforin/granzyme B, chemotherapeutic drugs, and gamma irradiation', *J Immunol*, 161: 3936-42.

Kaur, S., and D. D. Roberts. 2024. 'Emerging functions of thrombospondin-1 in immunity', *Semin Cell Dev Biol*, 155: 22-31.

Keene, J. A., and J. Forman. 1982. 'Helper activity is required for the in vivo generation of cytotoxic T lymphocytes', *J Exp Med*, 155: 768-82.

Kishimoto, T. 1989. 'The biology of interleukin-6', *Blood*, 74: 1-10.

———. 2005. 'Interleukin-6: from basic science to medicine--40 years in immunology', *Annu Rev Immunol*, 23: 1-21.

Krishnakumar, S. S., D. T. Radoff, D. Kümmel, C. G. Giraudo, F. Li, L. Khandan, S. W. Baguley, J. Coleman, K. M. Reinisch, F. Pincet, and J. E. Rothman. 2011. 'A conformational switch in complexin is required for synaptotagmin to trigger synaptic fusion', *Nat Struct Mol Biol*, 18: 934-40.

Kurowska, M., N. Goudin, N. T. Nehme, M. Court, J. Garin, A. Fischer, G. de Saint Basile, and G. Ménasché. 2012. 'Terminal transport of lytic granules to the immune synapse is mediated by the kinesin-1/Slp3/Rab27a complex', *Blood*, 119: 3879-89.

Kuta, A. E., C. R. Reynolds, and P. A. Henkart. 1989. 'Mechanism of lysis by large granular lymphocyte granule cytolysin: generation of a stable cytolysin-RBC intermediate', *J Immunol*, 142: 4378-84.

Law, R. H., N. Lukoyanova, I. Voskoboinik, T. T. Caradoc-Davies, K. Baran, M. A. Dunstone, M. E. D'Angelo, E. V. Orlova, F. Coulibaly, S. Verschoor, K. A. Browne, A. Ciccone, M. J. Kuiper, P. I. Bird, J. A. Trapani, H. R. Saibil, and J. C. Whisstock. 2010. 'The structural basis for membrane binding and pore formation by lymphocyte perforin', *Nature*, 468: 447-51.

Le Floc'h, A., and M. Huse. 2015. 'Molecular mechanisms and functional implications of polarized actin remodeling at the T cell immunological synapse', *Cell Mol Life Sci*, 72: 537-56.

Lee, J. U., L. K. Kim, and J. M. Choi. 2018. 'Revisiting the Concept of Targeting NFAT to Control T Cell Immunity and Autoimmune Diseases', *Front Immunol*, 9: 2747.

Lewis, R. S. 2001. 'Calcium signaling mechanisms in T lymphocytes', *Annu Rev Immunol*, 19: 497-521.

Li, S. S., Z. Liu, M. Uzunel, and K. G. Sundqvist. 2006. 'Endogenous thrombospondin-1 is a cell-surface ligand for regulation of integrin-dependent T-lymphocyte adhesion', *Blood*, 108: 3112-20.

Liao, W., J. X. Lin, and W. J. Leonard. 2013. 'Interleukin-2 at the crossroads of effector responses, tolerance, and immunotherapy', *Immunity*, 38: 13-25.

Liddicoat, A. M., and E. C. Lavelle. 2019. 'Modulation of innate immunity by cyclosporine A', *Biochem Pharmacol*, 163: 472-80.

Liu, J., J. D. Farmer, Jr., W. S. Lane, J. Friedman, I. Weissman, and S. L. Schreiber. 1991. 'Calcineurin is a common target of cyclophilin-cyclosporin A and FKBP-FK506 complexes', *Cell*, 66: 807-15.

Liu, J., Y. Ye, and L. Cai. 2020. 'Supramolecular attack particle: the way cytotoxic T lymphocytes kill target cells', *Signal Transduct Target Ther*, 5: 210.

Liu, Y., C. Schirra, L. Edelmann, U. Matti, J. Rhee, D. Hof, D. Bruns, N. Brose, H. Rieger, D. R. Stevens, and J. Rettig. 2010. 'Two distinct secretory vesicle-priming steps in adrenal chromaffin cells', *J Cell Biol*, 190: 1067-77.

Lowin, B., M. Hahne, C. Mattmann, and J. Tschopp. 1994. 'Cytolytic T-cell cytotoxicity is mediated through perforin and Fas lytic pathways', *Nature*, 370: 650-2.

Luccardini, C., A. V. Yakovlev, M. Pasche, S. Gaillard, D. Li, F. Rousseau, R. Ly, U. Becherer, J. M. Mallet, A. Feltz, and M. Oheim. 2009. 'Measuring mitochondrial and cytoplasmic Ca2+ in EGFP expressing cells with a low-affinity calcium Ruby and its dextran conjugate', *Cell Calcium*, 45: 275-83.

MacNeil, I. A., T. Suda, K. W. Moore, T. R. Mosmann, and A. Zlotnik. 1990. 'IL-10, a novel growth cofactor for mature and immature T cells', *J Immunol*, 145: 4167-73.

Magnetto, S., G. Bruno-Bossio, C. Voland, J. Lecerf, J. Lawler, P. Delmas, R. Silverstein, and P. Clezardin. 1998. 'CD36 mediates binding of soluble thrombospondin-1 but not cell adhesion and haptotaxis on immobilized thrombospondin-1', *Cell Biochem Funct*, 16: 211-21.

Maimela, N. R., S. Liu, and Y. Zhang. 2019. 'Fates of CD8+ T cells in Tumor Microenvironment', *Comput Struct Biotechnol J*, 17: 1-13.

Manders, E. M. M., F. J. Verbeek, and J. A. Aten. 1993. 'Measurement of co-localization of objects in dual-colour confocal images', *J Microsc*, 169: 375-82.

Mansfield, M. A., W. J. Peumans, and N. V. Raikhel. 1988. 'Wheat-germ agglutinin is synthesized as a glycosylated precursor', *Planta*, 173: 482-9.

Masopust, D., V. Vezys, A. L. Marzo, and L. Lefrançois. 2001. 'Preferential localization of effector memory cells in nonlymphoid tissue', *Science*, 291: 2413-7.

Matsubara, Y., G. Kiwan, J. Liu, L. Gonzalez, J. Langford, M. Gao, X. Gao, R. Taniguchi, B. Yatsula, T. Furuyama, T. Matsumoto, K. Komori, and A. Dardik. 2021. 'Inhibition of T-Cells by Cyclosporine A Reduces Macrophage Accumulation to Regulate Venous Adaptive Remodeling and Increase Arteriovenous Fistula Maturation', *Arterioscler Thromb Vasc Biol*, 41: e160-e74.

Matti, U., V. Pattu, M. Halimani, C. Schirra, E. Krause, Y. Liu, L. Weins, H. F. Chang, R. Guzman, J. Olausson, M. Freichel, F. Schmitz, M. Pasche, U. Becherer, D. Bruns, and J. Rettig. 2013. 'Synaptobrevin2 is the v-SNARE required for cytotoxic T-lymphocyte lytic granule fusion', *Nat Commun*, 4: 1439.

Maul-Pavicic, A., S. C. Chiang, A. Rensing-Ehl, B. Jessen, C. Fauriat, S. M. Wood, S. Sjöqvist, M. Hufnagel, I. Schulze, T. Bass, W. W. Schamel, S. Fuchs, H. Pircher, C. A. McCarl, K. Mikoshiba, K. Schwarz, S. Feske, Y. T. Bryceson, and S. Ehl. 2011. 'ORAI1-mediated calcium influx is required for human cytotoxic lymphocyte degranulation and target cell lysis', *Proc Natl Acad Sci U S A*, 108: 3324-9.

McGuire, M. J., P. E. Lipsky, and D. L. Thiele. 1993. 'Generation of active myeloid and lymphoid granule serine proteases requires processing by the granule thiol protease dipeptidyl peptidase I', *J Biol Chem*, 268: 2458-67.

McKenzie, M. D., N. L. Dudek, L. Mariana, M. M. Chong, J. A. Trapani, T. W. Kay, and H. E. Thomas. 2006. 'Perforin and Fas induced by IFNgamma and TNFalpha mediate beta cell death by OT-I CTL', *Int Immunol*, 18: 837-46.

Mihara, M., M. Hashizume, H. Yoshida, M. Suzuki, and M. Shiina. 2012. 'IL-6/IL-6 receptor system and its role in physiological and pathological conditions', *Clin Sci (Lond)*, 122: 143-59.

Mitchell, D. M., E. V. Ravkov, and M. A. Williams. 2010. 'Distinct roles for IL-2 and IL-15 in the differentiation and survival of CD8+ effector and memory T cells', *J Immunol*, 184: 6719-30.

Monks, C. R., B. A. Freiberg, H. Kupfer, N. Sciaky, and A. Kupfer. 1998. 'Three-dimensional segregation of supramolecular activation clusters in T cells', *Nature*, 395: 82-6.
Moore, K. W., A. O'Garra, R. de Waal Malefyt, P. Vieira, and T. R. Mosmann. 1993. 'Interleukin-10', *Annu Rev Immunol*, 11: 165-90.
Nagata, S. 1996. 'Fas-mediated apoptosis', *Adv Exp Med Biol*, 406: 119-24.
Niemann, H., J. Blasi, and R. Jahn. 1994. 'Clostridial neurotoxins: new tools for dissecting exocytosis', *Trends Cell Biol*, 4: 179-85.
Obar, J. J., and L. Lefrançois. 2010. 'Memory CD8+ T cell differentiation', *Ann N Y Acad Sci*, 1183: 251-66.
Oft, M. 2019. 'Immune regulation and cytotoxic T cell activation of IL-10 agonists - Preclinical and clinical experience', *Semin Immunol*, 44: 101325.
Oheim, M., A. Salomon, A. Weissman, M. Brunstein, and U. Becherer. 2019. 'Calibrating Evanescent-Wave Penetration Depths for Biological TIRF Microscopy', *Biophys J*, 117: 795-809.
Oldenborg, P. A., H. D. Gresham, and F. P. Lindberg. 2001. 'CD47-signal regulatory protein alpha (SIRPalpha) regulates Fcgamma and complement receptor-mediated phagocytosis', *J Exp Med*, 193: 855-62.
Otsuka, S., N. Melis, M. M. Gaida, D. Dutta, R. Weigert, and J. D. Ashwell. 2021. 'Calcineurin inhibitors suppress acute graft-versus-host disease via NFAT-independent inhibition of T cell receptor signaling', *J Clin Invest*, 131.
Packard, B. Z., W. G. Telford, A. Komoriya, and P. A. Henkart. 2007. 'Granzyme B activity in target cells detects attack by cytotoxic lymphocytes', *J Immunol*, 179: 3812-20.
Parekh, A. B., and R. Penner. 1997. 'Store depletion and calcium influx', *Physiol Rev*, 77: 901-30.
Parhamifar, L., and S. M. Moghimi. 2012. 'Total internal reflection fluorescence (TIRF) microscopy for real-time imaging of nanoparticle-cell plasma membrane interaction', *Methods Mol Biol*, 906: 473-82.
Peng, X., A. Kasran, and J. L. Ceuppens. 1997. 'Interleukin 12 and B7/CD28 interaction synergistically upregulate interleukin 10 production by human T cells', *Cytokine*, 9: 499-506.
Peters, P. J., J. Borst, V. Oorschot, M. Fukuda, O. Krähenbühl, J. Tschopp, J. W. Slot, and H. J. Geuze. 1991. 'Cytotoxic T lymphocyte granules are secretory lysosomes, containing both perforin and granzymes', *J Exp Med*, 173: 1099-109.
Poteryaev, D., S. Datta, K. Ackema, M. Zerial, and A. Spang. 2010. 'Identification of the switch in early-to-late endosome transition', *Cell*, 141: 497-508.
Purbhoo, M. A., D. J. Irvine, J. B. Huppa, and M. M. Davis. 2004. 'T cell killing does not require the formation of a stable mature immunological synapse', *Nat Immunol*, 5: 524-30.
Qu, B., V. Pattu, C. Junker, E. C. Schwarz, S. S. Bhat, C. Kummerow, M. Marshall, U. Matti, F. Neumann, M. Pfreundschuh, U. Becherer, H. Rieger, J. Rettig, and M. Hoth. 2011. 'Docking of lytic granules at the immunological synapse in human CTL requires Vti1b-dependent pairing with CD3 endosomes', *J Immunol*, 186: 6894-904.
Quang, C. T., B. Zaniboni, and J. Ghysdael. 2017. 'A TCR-switchable cell death pathway in T-ALL', *Oncoscience*, 4: 17-18.
Quann, E. J., E. Merino, T. Furuta, and M. Huse. 2009. 'Localized diacylglycerol drives the polarization of the microtubule-organizing center in T cells', *Nat Immunol*, 10: 627-35.
Quintana, A., M. Pasche, C. Junker, D. Al-Ansary, H. Rieger, C. Kummerow, L. Nuñez, C. Villalobos, P. Meraner, U. Becherer, J. Rettig, B. A. Niemeyer, and M. Hoth. 2011. 'Calcium microdomains at the immunological synapse: how ORAI channels, mitochondria and calcium pumps generate local calcium signals for efficient T-cell activation', *Embo j*, 30: 3895-912.
Rastogi, I., D. Jeon, J. E. Moseman, A. Muralidhar, H. K. Potluri, and D. G. McNeel. 2022. 'Role of B cells as antigen presenting cells', *Front Immunol*, 13: 954936.
Rettig, J., and C. T. Baldari. 2020. 'SMAPs: sweet carriers of lethal cargo for CTL-mediated killing', *Immunol Cell Biol*, 98: 524-27.
Rincon, M., and C. G. Irvin. 2012. 'Role of IL-6 in asthma and other inflammatory pulmonary diseases', *Int J Biol Sci*, 8: 1281-90.

Roberts, D. D., T. W. Miller, N. M. Rogers, M. Yao, and J. S. Isenberg. 2012. 'The matricellular protein thrombospondin-1 globally regulates cardiovascular function and responses to stress via CD47', *Matrix Biol*, 31: 162-9.

Salerno, F., N. A. Paolini, R. Stark, M. von Lindern, and M. C. Wolkers. 2017. 'Distinct PKC-mediated posttranscriptional events set cytokine production kinetics in CD8(+) T cells', *Proc Natl Acad Sci U S A*, 114: 9677-82.

Sallusto, F., J. Geginat, and A. Lanzavecchia. 2004. 'Central memory and effector memory T cell subsets: function, generation, and maintenance', *Annu Rev Immunol*, 22: 745-63.

Sauer, H., L. Pratsch, J. Tschopp, S. Bhakdi, and R. Peters. 1991. 'Functional size of complement and perforin pores compared by confocal laser scanning microscopy and fluorescence microphotolysis', *Biochim Biophys Acta*, 1063: 137-46.

Schandené, L., E. Cogan, A. Crusiaux, and M. Goldman. 1997. 'Interferon-alpha upregulates both interleukin-10 and interferon-gamma production by human CD4+ T cells', *Blood*, 89: 1110-1.

Schandené, L., G. F. Del Prete, E. Cogan, P. Stordeur, A. Crusiaux, B. Kennes, S. Romagnani, and M. Goldman. 1996. 'Recombinant interferon-alpha selectively inhibits the production of interleukin-5 by human CD4+ T cells', *J Clin Invest*, 97: 309-15.

Scheurich, P., B. Thoma, U. Ucer, and K. Pfizenmaier. 1987. 'Immunoregulatory activity of recombinant human tumor necrosis factor (TNF)-alpha: induction of TNF receptors on human T cells and TNF-alpha-mediated enhancement of T cell responses', *J Immunol*, 138: 1786-90.

Schiavo, G., F. Benfenati, B. Poulain, O. Rossetto, P. Polverino de Laureto, B. R. DasGupta, and C. Montecucco. 1992. 'Tetanus and botulinum-B neurotoxins block neurotransmitter release by proteolytic cleavage of synaptobrevin', *Nature*, 359: 832-5.

Schmittgen, T. D., B. A. Zakrajsek, A. G. Mills, V. Gorn, M. J. Singer, and M. W. Reed. 2000. 'Quantitative reverse transcription-polymerase chain reaction to study mRNA decay: comparison of endpoint and real-time methods', *Anal Biochem*, 285: 194-204.

Schoenborn, J. R., and C. B. Wilson. 2007. 'Regulation of interferon-gamma during innate and adaptive immune responses', *Adv Immunol*, 96: 41-101.

Schütze, S., K. Wiegmann, T. Machleidt, and M. Krönke. 1995. 'TNF-induced activation of NF-kappa B', *Immunobiology*, 193: 193-203.

Sharon, N., and H. Lis. 1972. 'Lectins: cell-agglutinating and sugar-specific proteins', *Science*, 177: 949-59.

Shen, Y., M. Rosendale, R. E. Campbell, and D. Perrais. 2014. 'pHuji, a pH-sensitive red fluorescent protein for imaging of exo- and endocytosis', *J Cell Biol*, 207: 419-32.

Siegmund, D., J. Kums, M. Ehrenschwender, and H. Wajant. 2016. 'Activation of TNFR2 sensitizes macrophages for TNFR1-mediated necroptosis', *Cell Death Dis*, 7: e2375.

Sleiman, M., D. R. Stevens, P. Chitirala, and J. Rettig. 2020. 'Cytotoxic Granule Trafficking and Fusion in Synaptotagmin7-Deficient Cytotoxic T Lymphocytes', *Front Immunol*, 11: 1080.

Smith-Garvin, J. E., G. A. Koretzky, and M. S. Jordan. 2009. 'T cell activation', *Annu Rev Immunol*, 27: 591-619.

Smith, K. A. 1988. 'Interleukin-2: inception, impact, and implications', *Science*, 240: 1169-76.

Smith, L. K., G. M. Boukhaled, S. A. Condotta, S. Mazouz, J. J. Guthmiller, R. Vijay, N. S. Butler, J. Bruneau, N. H. Shoukry, C. M. Krawczyk, and M. J. Richer. 2018. 'Interleukin-10 Directly Inhibits CD8(+) T Cell Function by Enhancing N-Glycan Branching to Decrease Antigen Sensitivity', *Immunity*, 48: 299-312.e5.

Stemberger, C., K. M. Huster, M. Koffler, F. Anderl, M. Schiemann, H. Wagner, and D. H. Busch. 2007. 'A single naive CD8+ T cell precursor can develop into diverse effector and memory subsets', *Immunity*, 27: 985-97.

Steyer, J. A., and W. Almers. 2001. 'A real-time view of life within 100 nm of the plasma membrane', *Nat Rev Mol Cell Biol*, 2: 268-75.

Steyer, J. A., H. Horstmann, and W. Almers. 1997. 'Transport, docking and exocytosis of single secretory granules in live chromaffin cells', *Nature*, 388: 474-8.

Stinchcombe, J., G. Bossi, and G. M. Griffiths. 2004. 'Linking albinism and immunity: the secrets of secretory lysosomes', *Science*, 305: 55-9.

Stinchcombe, J. C., and G. M. Griffiths. 2007. 'Secretory mechanisms in cell-mediated cytotoxicity', *Annu Rev Cell Dev Biol*, 23: 495-517.

Stinchcombe, J. C., M. Salio, V. Cerundolo, D. Pende, M. Arico, and G. M. Griffiths. 2011. 'Centriole polarisation to the immunological synapse directs secretion from cytolytic cells of both the innate and adaptive immune systems', *BMC Biol*, 9: 45.

Stout, A. L., and D. Axelrod. 1989. 'Evanescent field excitation of fluorescence by epi-illumination microscopy', *Appl Opt*, 28: 5237-42.

Sun, L., Y. Su, A. Jiao, X. Wang, and B. Zhang. 2023. 'T cells in health and disease', *Signal Transduct Target Ther*, 8: 235.

Survase, S. A., L. D. Kagliwal, U. S. Annapure, and R. S. Singhal. 2011. 'Cyclosporin A--a review on fermentative production, downstream processing and pharmacological applications', *Biotechnol Adv*, 29: 418-35.

Suto, A., D. Kashiwakuma, S. Kagami, K. Hirose, N. Watanabe, K. Yokote, Y. Saito, T. Nakayama, M. J. Grusby, I. Iwamoto, and H. Nakajima. 2008. 'Development and characterization of IL-21-producing CD4+ T cells', *J Exp Med*, 205: 1369-79.

Tan, K., and J. Lawler. 2009. 'The interaction of Thrombospondins with extracellular matrix proteins', *J Cell Commun Signal*, 3: 177-87.

Tau, G. Z., S. N. Cowan, J. Weisburg, N. S. Braunstein, and P. B. Rothman. 2001. 'Regulation of IFN-gamma signaling is essential for the cytotoxic activity of CD8(+) T cells', *J Immunol*, 167: 5574-82.

Tomono, M., K. Toyoshima, M. Ito, and H. Amano. 1996. 'Calcineurin is essential for DNA synthesis in Swiss 3T3 fibroblasts', *Biochem J*, 317 (Pt 3): 675-80.

Torang, A., P. Gupta, and D. J. Klinke, 2nd. 2019. 'An elastic-net logistic regression approach to generate classifiers and gene signatures for types of immune cells and T helper cell subsets', *BMC Bioinformatics*, 20: 433.

Traore, D. A., A. J. Brennan, R. H. Law, C. Dogovski, M. A. Perugini, N. Lukoyanova, E. W. Leung, R. S. Norton, J. A. Lopez, K. A. Browne, H. Yagita, G. J. Lloyd, A. Ciccone, S. Verschoor, J. A. Trapani, J. C. Whisstock, and I. Voskoboinik. 2013. 'Defining the interaction of perforin with calcium and the phospholipid membrane', *Biochem J*, 456: 323-35.

Tschopp, J., D. Masson, and K. K. Stanley. 1986. 'Structural/functional similarity between proteins involved in complement- and cytotoxic T-lymphocyte-mediated cytolysis', *Nature*, 322: 831-4.

Tuomela, K., A. R. Ambrose, and D. M. Davis. 2022. 'Escaping Death: How Cancer Cells and Infected Cells Resist Cell-Mediated Cytotoxicity', *Front Immunol*, 13: 867098.

Uhlén, M., E. Björling, C. Agaton, C. A. Szigyarto, B. Amini, E. Andersen, A. C. Andersson, P. Angelidou, A. Asplund, C. Asplund, L. Berglund, K. Bergström, H. Brumer, D. Cerjan, M. Ekström, A. Elobeid, C. Eriksson, L. Fagerberg, R. Falk, J. Fall, M. Forsberg, M. G. Björklund, K. Gumbel, A. Halimi, I. Hallin, C. Hamsten, M. Hansson, M. Hedhammar, G. Hercules, C. Kampf, K. Larsson, M. Lindskog, W. Lodewyckx, J. Lund, J. Lundeberg, K. Magnusson, E. Malm, P. Nilsson, J. Odling, P. Oksvold, I. Olsson, E. Oster, J. Ottosson, L. Paavilainen, A. Persson, R. Rimini, J. Rockberg, M. Runeson, A. Sivertsson, A. Sköllermo, J. Steen, M. Stenvall, F. Sterky, S. Strömberg, M. Sundberg, H. Tegel, S. Tourle, E. Wahlund, A. Waldén, J. Wan, H. Wernérus, J. Westberg, K. Wester, U. Wrethagen, L. L. Xu, S. Hober, and F. Pontén. 2005. 'A human protein atlas for normal and cancer tissues based on antibody proteomics', *Mol Cell Proteomics*, 4: 1920-32.

Vaeth, M., S. Kahlfuss, and S. Feske. 2020. 'CRAC Channels and Calcium Signaling in T Cell-Mediated Immunity', *Trends Immunol*, 41: 878-901.

Valitutti, S., S. Müller, M. Cella, E. Padovan, and A. Lanzavecchia. 1995. 'Serial triggering of many T-cell receptors by a few peptide-MHC complexes', *Nature*, 375: 148-51.

Valvo, S., V. Mayya, E. Seraia, J. Afrose, H. Novak-Kotzer, D. Ebner, and M. L. Dustin. 2017. 'Comprehensive Analysis of Immunological Synapse Phenotypes Using Supported Lipid Bilayers', *Methods Mol Biol*, 1584: 423-41.

Van Parijs, L., D. A. Peterson, and A. K. Abbas. 1998. 'The Fas/Fas ligand pathway and Bcl-2 regulate T cell responses to model self and foreign antigens', *Immunity*, 8: 265-74.

Villegas-Mendez, A., J. B. de Souza, L. Murungi, J. C. Hafalla, T. N. Shaw, R. Greig, E. M. Riley, and K. N. Couper. 2011. 'Heterogeneous and tissue-specific regulation of effector T cell

responses by IFN-gamma during Plasmodium berghei ANKA infection', *J Immunol*, 187: 2885-97.

Voskoboinik, I., M. J. Smyth, and J. A. Trapani. 2006. 'Perforin-mediated target-cell death and immune homeostasis', *Nat Rev Immunol*, 6: 940-52.

Wajant, H., K. Pfizenmaier, and P. Scheurich. 2003. 'Tumor necrosis factor signaling', *Cell Death Differ*, 10: 45-65.

Weber, T., B. V. Zemelman, J. A. McNew, B. Westermann, M. Gmachl, F. Parlati, T. H. Söllner, and J. E. Rothman. 1998. 'SNAREpins: minimal machinery for membrane fusion', *Cell*, 92: 759-72.

Weninger, W., M. A. Crowley, N. Manjunath, and U. H. von Andrian. 2001. 'Migratory properties of naive, effector, and memory CD8(+) T cells', *J Exp Med*, 194: 953-66.

Wißfeld, J., M. Hering, N. Ten Bosch, and G. Cui. 2024. 'The immunosuppressive drug cyclosporin A has an immunostimulatory function in CD8(+) T cells', *Eur J Immunol*, 54: e2350825.

Xiong, Y., K. A. Libby, and X. Su. 2024. 'The physical landscape of CAR-T synapse', *Biophys J*, 123: 2199-210.

Yamamoto, S., J. Gaillard, B. Vianay, C. Guerin, M. Orhant-Prioux, L. Blanchoin, and M. Théry. 2022. 'Actin network architecture can ensure robust centering or sensitive decentering of the centrosome', *Embo j*, 41: e111631.

Yokota, S., T. D. Geppert, and P. E. Lipsky. 1988. 'Enhancement of antigen- and mitogen-induced human T lymphocyte proliferation by tumor necrosis factor-alpha', *J Immunol*, 140: 531-6.

Zanier, E. R., S. Fumagalli, C. Perego, F. Pischiutta, and M. G. De Simoni. 2015. 'Shape descriptors of the "never resting" microglia in three different acute brain injury models in mice', *Intensive Care Med Exp*, 3: 39.

Zhang, M., S. M. Park, Y. Wang, R. Shah, N. Liu, A. E. Murmann, C. R. Wang, M. E. Peter, and P. G. Ashton-Rickardt. 2006. 'Serine protease inhibitor 6 protects cytotoxic T cells from self-inflicted injury by ensuring the integrity of cytotoxic granules', *Immunity*, 24: 451-61.

Zhang, S. L., Y. Yu, J. Roos, J. A. Kozak, T. J. Deerinck, M. H. Ellisman, K. A. Stauderman, and M. D. Cahalan. 2005. 'STIM1 is a Ca2+ sensor that activates CRAC channels and migrates from the Ca2+ store to the plasma membrane', *Nature*, 437: 902-5.

7. Annex

Standard curves produced using LEGENDplex™ software for a multiplex bead-based immunoassay. The blue points are the experimental data, the smooth curve (blue line) is the fitted standard curve. The data represents the mean fluorescence intensity (MFI) measured at known concentrations of IL-6, IFN-γ, TNF-α, IL-10, and IL-2. This measured levels under the restimulation condition (A) and the CsA-treated CTLs (B). The orange line represents the Limit of Detection (LOD) of the assay, which is the lowest concentration that the system can reliably detect. The red line indicates data that were excluded from the curve fitting, often because they were below the LOD or were considered outliers. The fitted curve indicates the concentration-MFI relationship, where the R^2 value represents the goodness of fit, and the red box shows the data points of the experiment. Note that: the absence of the red line means that the level of the measured cytokine is so less to be detected.

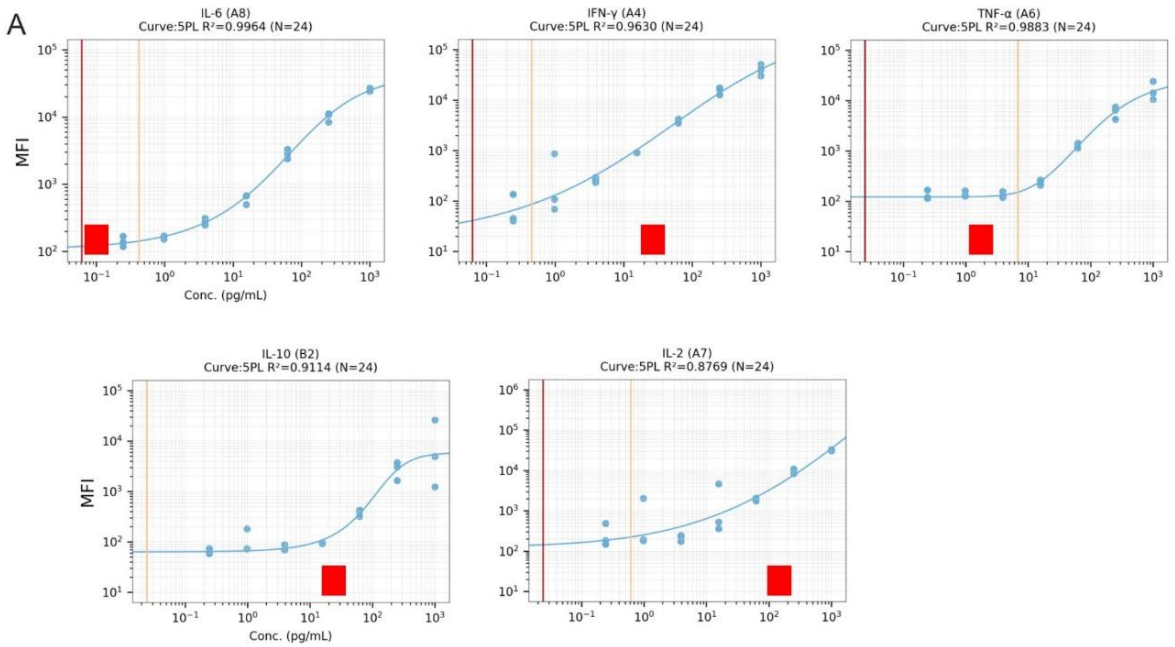

Figure (A): The levels of extracellular cytokines (IL-6, IFN-γ, TNF-α, IL-10, and IL-2) were analyzed from day 6 in both control and restimulated T-cells using the LEGENDplex data analysis software. IL-6 and TNF-α were below the limit of detection (LOD), while the measured concentration of IL-10 was too low to be detected. In contrast, IL-2 and IFN-γ were within reliable detection levels.

B

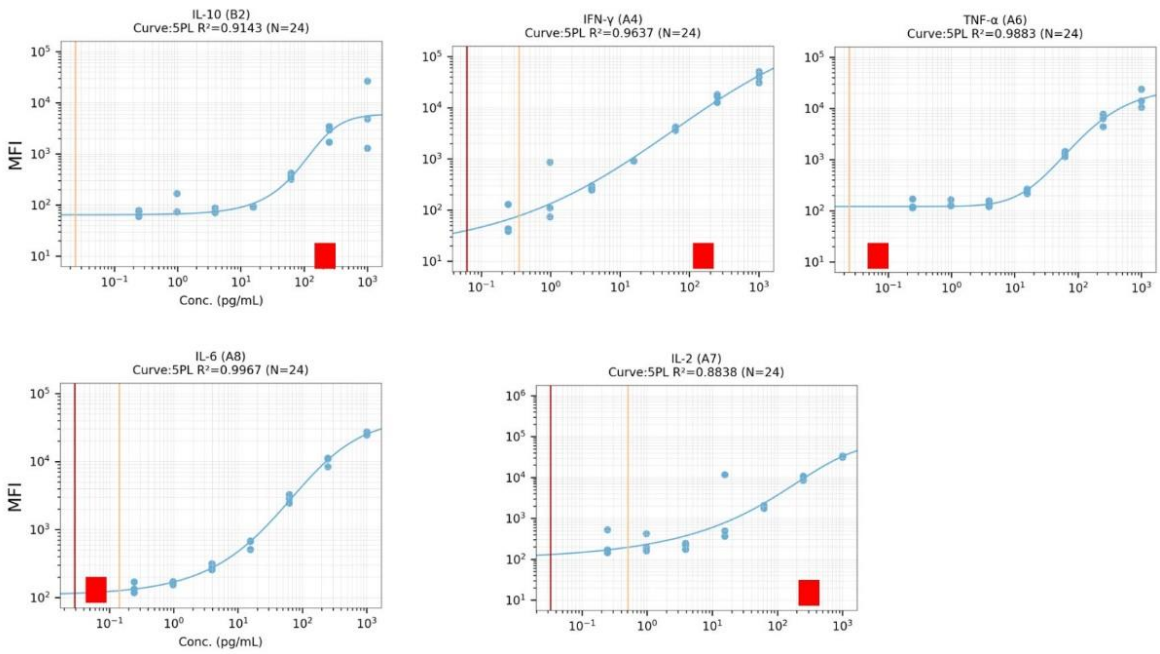

Figure (B): The levels of extracellular cytokines (IL-6, IFN-γ, TNF-α, IL-10, and IL-2) were analyzed on days 4 and 8 in both control and CsA-treated T cells using the LEGENDplex data analysis software. IL-10 and TNF-α levels were too low to be detected, while IL-6 was below the limit of detection (LOD). In contrast, IL-2 and IFN-γ levels were within the range of reliable detection.

8. Publications

Omnia M. Khamis, Claudia Schirra, Abed Alrahman Chouaib, Szumin Tu, Ute Becherer. SMAP biogenesis and secretion from mouse CTL is increased over time in an interferon-dependent manner (manuscript in preparation).

Chouaib Abed Alrahman, Hsin-Fang Chang, **Omnia M. Khamis**, Santiago Echeverry, Lucie Demeersseman, Sofia Elizarova, James A Daniel, Salvatore Valitutti, Sebastian Barg, Constantin Pape, Ali H. Shaib, and Ute Becherer. 2024. 'Highly adaptable deep-learning platform for automated detection and analysis of vesicle exocytosis', Nat Commun:16, 6450 (2025).

Amina E Essawy, Wessam M Abdel-Wahab, Ismail A Sadek, **Omnia M Khamis**. 2018. 'Dual protective effect of ginger and rosemary extracts against CCl_4-induced hepatotoxicity in rats', Environ Sci Pollut Res Int.:(20):19510-19517.

9. Curriculum Vitae

Aus datenschutzrechtlichen Gründen wird der Lebenslauf in der elektronischen Fassung der Dissertation nicht veröffentlicht.

For data protection reasons, the curriculum vitae is not published in the electronic version of the dissertation.